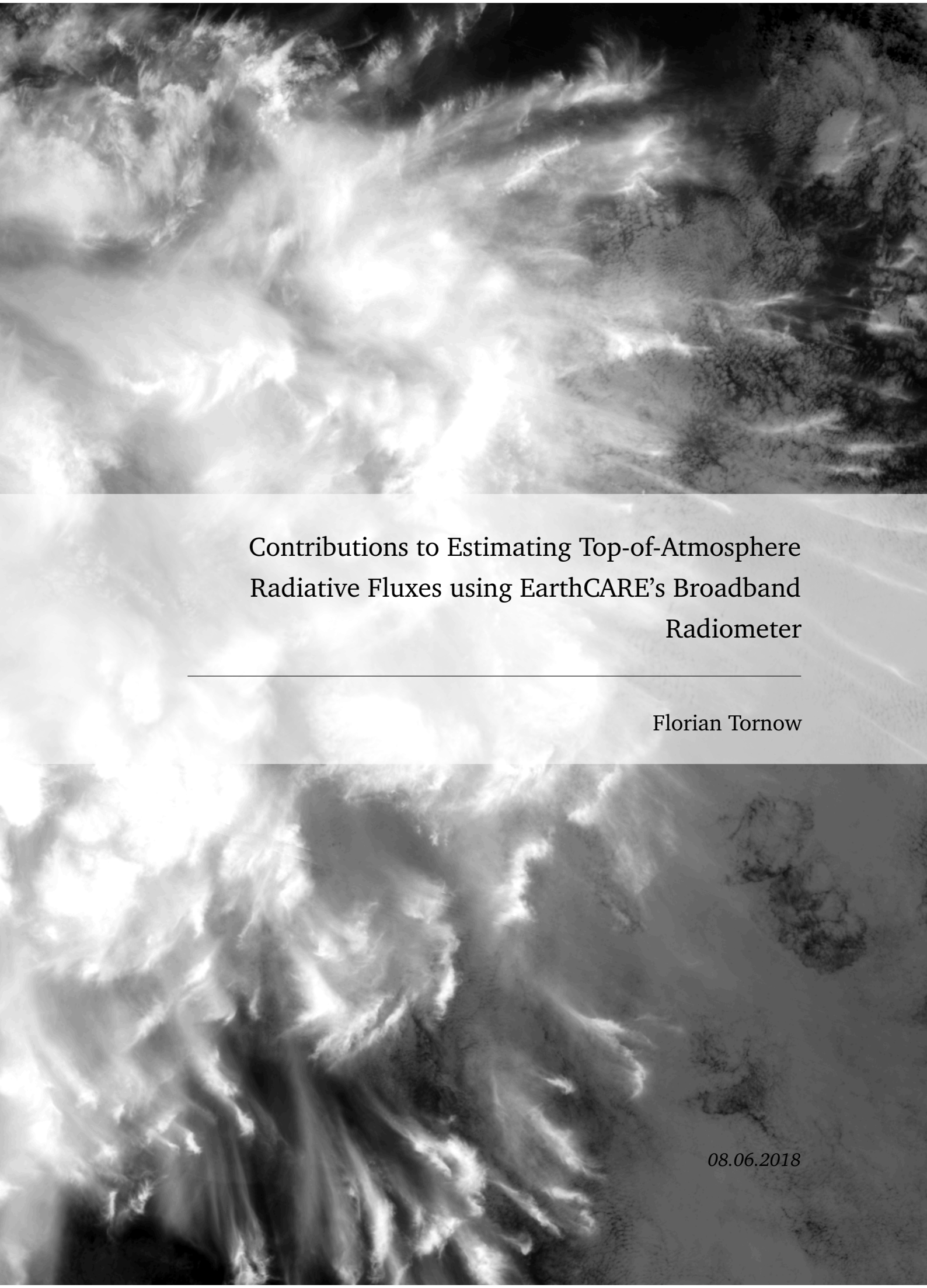

Contributions to Estimating Top-of-Atmosphere Radiative Fluxes using EarthCARE's Broadband Radiometer

Florian Tornow

08.06.2018

Cover: Landsat imagery on 13.06.2017, courtesy of NASA Goddard Space Flight Center and U.S. Geological Survey

Freie Universität Berlin

Department of Earth Sciences
Institute for Space Sciences

Dissertation

zur Erlangung des akademischen Grades eines Doktors der Naturwissenschaften am Fachbereich für Geowissenschaften der Freien Universität Berlin

Contributions to Estimating Top-of-Atmosphere Radiative Fluxes using EarthCARE's Broadband Radiometer

vorgelegt von

Florian Tornow

1. Gutachter	Prof. Dr. Jürgen Fischer Department of Earth Sciences Freie Universität Berlin
2. Gutachter	Prof. Dr. Ralf Bennartz Earth and Environmental Sciences Vanderbilt University
Disputationstermin	18.07.2018

08.06.2018

Florian Tornow

Contributions to Estimating Top-of-Atmosphere Radiative Fluxes using EarthCARE's Broadband Radiometer

Dissertation, 08.06.2018
Reviewers: Prof. Dr. Jürgen Fischer and Prof. Dr. Ralf Bennartz
Supervisor: Jürgen Fischer

Freie Universität Berlin
Institute for Space Sciences
Department of Earth Sciences
Carl-Heinrich-Becker-Weg 6-10
12165 Berlin

Selbstständigkeitserklärung

Hiermit erkläre ich an Eides Statt, dass ich die vorliegende Arbeit selbstständig und ohne fremde Hilfe angefertigt, keine anderen als die angegebenen Quellen und Hilfsmittel benutzt und die den benutzten Quellen wörtlich oder inhaltlich entnommenen Stellen als solche kenntlich gemacht habe. Diese Arbeit hat in gleicher oder ähnlicher Form noch keiner Prüfungsbehörde vorgelegen.

Berlin, 08.06.2018

Florian Tornow

Erklärung zu inhaltlichen Beiträgen der Co-Autoren an verschiedenen Publikationen innerhalb der kumulativen Dissertation

Alle folgend gelisteten Publikationen sind Teil der vorliegenden kumulativen Dissertation und enthalten Beiträge von Co-Autoren. Generell lässt sich festhalten, dass ich als Erstautor aller vier Publikationen qualitativ und quantitativ den Großteil beitrug.

Tornow F., Barker, H. W., Velázquez Blázquez, A., Domenech, C., Fischer, J., EarthCARE's Broadband Radiometer: Unforeseen Uncertainties Associated with Cloudy Atmospheres, submitted to *Journal of Atmospheric and Oceanic Technology*, May 2018

Mein Beitrag war die Datenbeschaffung, die Durchführung der Auswertung und die Präsentation in wissenschaftlicher Form. Die Idee zur Arbeit stammte von Carlos Domenech, Howard W. Barker und mir. Howard W. Barker unterstützte mich bei der Konzeption der Studie und bei der mathematischen Formulierung des Problems. Zusammen mit Almudena Velázquez Blázquez und Carlos Domenech, verifizierte Howard W. Barker meine Resultate an separaten Daten. Diese Verifikation wurde allerdings nicht in der Publikation aufgeführt. Jürgen Fischer stellte Ressourcen zur Durchführung der Arbeit bereit und formte die Studie in gemeinsamer Diskussion. Das Manuskript, das zum Großteil von mir geschrieben wurde, enthält umgesetzte Verbesserungsvorschläge aller Co-Autoren bezüglich Text und grafischer Darstellung.

Tornow, F., Domenech, C., Fischer, J., On the use of geophysical parameters for the top-of-atmosphere shortwave clear-sky radiance-to-flux conversion in EarthCARE, submitted to *Journal of Atmospheric and Oceanic Technology*, May 2018

Ich hatte die Idee zur Studie und führte die Datenbeschaffung, Datenaufbereitung, Auswertung sowie Präsentation in wissenschaftlicher Form durch. Carlos Domenech half mir dabei die Studie zu konzipieren. Jürgen Fischer stellte notwendige Ressourcen zur Durchführung der Studie bereit. Das Manuskript, das ausschließlich von mir geschrieben wurde, erfuhr Verbesserungen in Text und grafischer Darstellung, die auf Kritik von Jürgen Fischer und Carlos Domenech basierten.

Tornow, F., Preusker, R., Domenech, C., Carbajal Henken, C. K., Testorp, S., Fischer, J., Top-of-atmosphere shortwave anisotropy over liquid clouds: sensitivity to clouds' microphysical structure and cloud-topped moisture, 2018, *MDPI Atmosphere*, 9(7), 256

Die Idee zur Studie stammt von mir. Datenbeschaffung (inklusive numerischer Simulationen), Auswertung, und Präsentation in wissenschaftlicher Form führte ich durch. Renè Preusker und Carlos Domenech unterstützten mich bei der Konzeptionalisierung. Cintia K. Carbajal Henken und Sören Testorp halfen mir bezüglich Detailfragen in der Methodik. Jürgen Fischer stellte notwendige Ressourcen bereit und unterstützte mich bei den Vorbereitungen der Simulationen. Alle Co-Autoren trugen mittels kritischer Vorschläge dazu bei, das Manuskript, das ausschließlich von mir geschrieben wurde, in Text und grafischer Darstellung zu verbessern.

Tornow, F., Barker, H. W., Domenech, C., On the use of Simulated Photon Paths to Co-register TOA radiances in EarthCARE Radiative Closure Experiments, 2015, *Quarterly Journal of the Royal Meteorological Society*, 144 (693), 3239-3251

Zusammen mit Carlos Domenech, der die Idee zu dieser Arbeit hatte, konzipierte ich die Studie. Howard W. Barker führte numerische Simulationen durch. Ich leitete die Auswertung und Darstellung in wissenschaftlicher Form. Das Manuskript, das zum Großteil von mir geschrieben wurde, enthält Beiträge von Howard W. Barker. Alle Co-Autoren trugen durch kritische Anmerkungen zu Text und Grafik zur finalen Form der Publikation bei.

Berlin, 08.06.2018

Florian Tornow

Contents

1 Introduction

> *If you learned how to make a cloud, your time is not wasted.*
>
> **— Bob Ross**
> (painter, instructor, and television host)

Much like painters, climate scientists strive to represent clouds accurately in their work. Instead of paintings, climate scientists create global climate models (GCMs) that predict the future climate. Clouds are crucial elements, affecting water and energy cycles in the Earth-atmosphere system, and it is difficult to capture their complexity in a GCM.

Focusing on individual clouds - whether large enough to be resolved by a GCM's spatial grid or smaller than the grid size and therefore parametrized - a model needs to answer questions such as: How does cloud liquid and ice condensate distribute horizontally and vertically? How intense is cloud turbulent mixing with surrounding dry air? When and how much do clouds precipitate? And how would answers to these questions change if clouds interact with aerosols or are surrounded by a warmer and possibly moister atmosphere in a future climate?

Clouds affect the radiation budget at top-of-atmosphere (TOA), and their effects vary according to their micro- and macrophysical properties. Clouds represent the largest uncertainty for understanding and assessing Earth's changing energy budget (Boucher et al., 2013, and and references therein).

Clouds impact the TOA radiation budget as they reflect incoming shortwave (SW) radiation back to space and emit longwave (LW) radiation towards TOA. SW reflection generally cools Earth's surface as less radiation reaches the surface level for local absorption. Cloud albedo grows with amount of cloud liquid and ice water and with the degree of cloud-aerosol interaction (Twomey, 1977) distributing the same cloud water over more numerous but smaller cloud droplets or ice crystals. In terms of optical properties, cloud albedo is proportional to cloud optical depth (COD) and the inverse of cloud droplet size distribution. Whenever summarizing clouds over a horizontal domain with a specific domain-average COD, domain cloud albedo decreases as within-domain COD becomes more heterogeneous (e.g. Barker et al., 1996; Kato et al., 2005). LW emission generally increases with cloud temperature

and COD. A cloud located at higher (and naturally colder) altitudes therefore emits less LW radiation and even absorbs surface-originated LW radiation, which the cloud partly re-emits back down, thus warming Earth's surface. Low clouds, on the other hand, emit at a near-surface temperature. They can form large and optically thick sheets covering the oceans, and thus efficiently reflect solar radiation. In turn, low-clouds cool Earth's surface. Recent estimates on the global net effect of clouds imply that the SW cooling generally outweighs the LW heating by about 21.5$\pm$5 W m^{-2} (Stephens et al., 2012), thus leaving - on average - a colder atmosphere behind due to clouds.

Satellites and their remote-sensing instruments have provided valuable benchmarks for GCM development. Broadband radiometry from space started with the Earth Radiation Budget (ERB) experiment (Jacobowitz et al., 1979; Jacobowitz et al., 1984; Kyle et al., 1993) and continues today with CERES (Clouds and the Earth's Radiant Energy System, Wielicki et al., 1996) on polar-orbiting Aqua and Terra satellites, GERB (Geostationary Earth Radiation Budget, Mueller et al., 1999) on geostationary Meteosat Second Generation satellites, and ScaRaB (Scanner for Radiation Budget, Kandel et al., 1998) onboard Megha-tropiques in near-equatorial orbit. Global net effect estimates historically changed through improved instrumentation- and improved algorithms converting TOA SW or LW radiance measurements into TOA SW or LW fluxes: from -16.6 W m^{-2} (Ramanathan et al., 1989), -26.8 W m^{-2} (Ardanuy et al., 1991), -32.4 W m^{-2} (Rossow and Zhang, 1995), to -20.0 W m^{-2} (Kiehl and Trenberth, 1997). Recent efforts combined active instruments, CALIOP (Cloud-Aerosol Lidar with Orthogonal Polarization, Winker et al., 2009) onboard the CALIPSO (Cloud-Aerosol Lidar and Infrared Pathfinder Satellite Observations) satellite and the CloudSat CPR (Cloud Profiling Radar), together with the passive instrument MODIS (Moderate Resolution Imaging Spectro-radiometer) - all part of the A-Train satellite constellation (Stephens et al., 2002) - to show that radiation budget estimates crucially improved when combining information from all sensors (Kato et al., 2011). The upcoming ESA-JAXA (European Space Agency and Japan Aerospace Exploration Agency) satellite mission EarthCARE (Earth Clouds, Aerosols and Radiation Explorer, Illingworth et al., 2015) - to be launched in 2020 - will also use this combination of active (the Cloud Profiling Radar, CPR, as well as the ATmospheric LIdar, ATLID) and passive (Multi-Spectral Imager, MSI) instruments. The EarthCARE mission's goal is to evaluate the state-of-the-art knowledge on cloud-aerosol-radiation interaction. A radiative closure assessment compares 1) simulated TOA SW and LW fluxes from 1D and 3D broadband radiative transfer models acting on a 3D atmosphere of cloud and aerosol properties inferred from combined active-passive retrieval (Barker et al., 2011) with 2) estimated SW and LW fluxes from SW (0.25-$4.00\,\mu$m) and Total Wave (TW, 0.25 - $>50\,\mu$m) measurements performed by the on-board BBR (Broadband Radiometer, Wallace et al., 2009). The comparison will assess simulated and measurement-based TOA fluxes over horizontal domains

of $\sim$100 km^2, and requires a difference of no more than $\pm$10 W m^{-2} in SW and LW fluxes to claim understanding of cloud-aerosol-radiation interaction. In addition, vertical heating rate profiles - a valuable byproduct from radiative transfer simulations - can be trusted and used to assess current GCMs and their parametrizations.

This dissertation contributes in various ways to EarthCARE's BBR-based flux estimation and corresponding uncertainties. Chapter 2 quantifies a so-far unaccounted uncertainty in SW and TW measured radiances that arises from the assembly of individual BBR footprints of ($\sim$0.6 km)^2 size towards $\sim$100 km^2 domains and the fact that horizontal radiance fields are naturally heterogeneous. BBR instrument performance and thus sampling density is in-flight adjustable. LW radiances need to be inferred from staggered TW and SW radiances. We show the sensitivity of SW and LW radiances to radiance heterogeneity and instrument performance by using high-spatial resolution Landsat 8 imagery and mimicked BBR sampling. We finally recommended a minimum instrument performance in order to keep resulting flux uncertainties below 10 W m^{-2}.

Chapter 3 presents a novel way to convert TOA SW radiances, measured over clear-sky domains, into TOA SW fluxes. Instead of directly using state-of-the-art CERES Angular Distributions models (ADMs; providing empirical conversion factors), which are separately built per $1^\circ \times 1^\circ$ longitude-latitude bin and per calendar month to convert over land surfaces, we find a new representation of CERES ADMs that dissolves spatio-temporal binning. This was possible through the use of additional geophysical variables in Artificial Neural Networks (ANNs). Our results show how important variables were identified and how well we reproduced CERES ADMs.

In theory, the conversion of SW radiances towards fluxes above low-level clouds should be sensitive to the cloud droplet size distribution as well as cloud-topped water vapor. This was confirmed by the precise and flexible in-house radiative transfer code MOMO (Matrix-Operator Model, Hollstein and Fischer, 2012), which was used to simulate azimuthally resolved TOA SW radiances for various cloud optical properties as well as vertical temperature and moisture profiles. Chapter 4 shows that current CERES ADMs lack such sensitivity, demonstrates the construction of new and refined ADMs by using several years of CERES-MODIS observation as well as broadband radiative transfer simulations, and quantifies the impact onto flux estimation. We specifically looked into the potential introduction of biases into radiation budget climatologies.

Three BBR views and corresponding flux estimates should be colocated towards their supposed domain of origin. While such colocation is straight-forward for clear-sky conditions (colocation at surface level) or for opaque clouds (colocation at cloud-top altitude), there is no obvious vertical level of colocation for broken

or semitransparent clouds fields. Chapter 5 introduces a novel way to colocate. Applied to the best estimate of the 3D atmosphere and constituents therein, 3D Monte Carlo radiative transfer simulations produced photon paths. Such paths allowed us to identify those measurements across the three views, which received SW-scattered contributions from very similar vertical levels within the atmosphere. We demonstrate the application to a 5000 km domain of A-train data and discuss the performance and applicability of this novel method. Finally, Chapter 6 concludes findings of this thesis.

2

EarthCARE's Broadband Radiometer: Unforeseen Uncertainties Associated with Cloudy Atmospheres

Abstract

The EarthCARE satellite's Broadband Radiometer (BBR) consists of three telescopes and a rotating chopper drum (CD). Together they yield alternating measurements of totalwave (TW) (0.25 - $>50\,\mu$m) and shortwave (SW) (0.25 - $4\,\mu$m) radiances with point-spread functions that translate to $\sim$0.6 km diameter pixels. The mission requires that SW and TW radiances be averaged over $\sim$100 km^2 domains. Corresponding average longwave (LW) radiances are differences between TW and SW averages. It is shown that impacts on domain-average nadir radiances due to alternating samples of TW and SW signals for realistic cloudy atmospheres are sensitive to: variance of cloudy-sky radiances; CD rotation rate; and along-track length of averaging domains. The BBR's design allows for in-flight alteration of CD rate. An approximate method is provided for estimating SW and LW uncertainties due to CD rate. While the nominal rotation rate meets EarthCARE's mission requirements, reducing below $\sim$75% of that rate will lead to uncertainties for domain-average LW radiances that will often exceed mission requirements. This could be mitigated by increasing the size of averaging domains, but that would compromise the BBR's role in EarthCARE's radiative closure assessment programme. Uncertainties for off-nadir radiances are largely free of impacts arising from changes to CD rotation rate.

Tornow, F., Barker, H. W., Velázquez Blázquez, A., Domenech, C., Fischer, J.,
submitted to Journal of Atmospheric and Oceanic Technology, May 2018, in revision

2.1 Introduction

The EarthCARE (Earth, Clouds, Aerosols, and Radiation Explorer) satellite mission is a collaboration between the European Space Agency (ESA) and Japan Aerospace Exploration Agency (JAXA). It will be launched no sooner than the end of 2020, and will yield radar, lidar, and multi-spectral imager (MSI) measurements for synergistic retrieval of cloud and aerosol properties profiles for $\sim$(1 km)^2 nadir columns. EarthCARE's goal (ESA, 2001; ESA, 2006) is that when broadband radiative transfer models act on retrieved cloud and aerosol properties, estimated top-of-atmosphere (TOA) fluxes for domains with areas $\sim$100 km^2 will be, on average, within $\pm$10 W m^{-2} of fluxes inferred from radiances measured by its BroadBand Radiometer (BBR) (see Illingworth et al., 2015). This "radiative closure assessment" experiment has been a central driver to the overall design of the EarthCARE mission.

The BBR will measure TOA filtered radiances at nadir and two along-track oblique views, with viewing zenith angles of $\sim$53°, for a $\sim$30 km-wide swath (Wallace et al., 2009). It consists of three telescopes, microbolometer arrays of detectors, a rotating chopper drum mechanism (CDM), and a silica filter to produce SW radiances. Radiances measurements alternate between totalwave (TW) (0.25 - $>50\,\mu$m) and shortwave (SW) (0.25 - $4\,\mu$m) with point-spread functions that amount to $\sim$0.6 km diameter pixels separated by ground sampling distance d_s. Hence, SW and TW measurements are separated by $d_s/2$. The telescopes' characteristics require (mission-worthy) radiances to be averaged over (10 km)^2 areas. As such, areas used for the radiative closure experiment will be more rectangular but still cover $\sim$100 km^2. They are referred to hereinafter as "assessment domains". Correspondingly, longwave (LW) average radiances are differences between TW and SW averages.

By design, the CDM rotation rate can be adjusted whilst in orbit thereby facilitating possible extensions to the mission's lifetime (per. comm., A. Lefebvre 2018; Caldwell et al., 2017b). Although standard radiometric performance assessments of the BBR have occurred, uncertainties for assessment domain-average radiances due to intermittent sampling of TW and SW radiances have not been quantified. Such uncertainties can be expected when radiances exhibit significant fluctuations at spatial scales near pixel size and, and are to be averaged over relatively small assessment domains; such as cloud fields within EarthCARE-size assessment domains (e.g. Barker et al., 2017). Given the BBR's central role in Earth-CARE's radiative closure experiment, it is essential that BBR radiance uncertainties be quantified as well as possible. Moreover, it is useful to know the approximate lower-bound on CDM rotation rate so as not to compromise the closure experiment.

Hence, the primary purpose of this paper is to report on an investigation into the dependence of nadir BBR radiance uncertainties on d_s via CDM rotation rate. While

analyses focus entirely on cloudy atmospheres, results apply to all scenes that exhibit radiometric variability. Off-nadir radiances, being sufficiently over-sampled in the along-track direction, are almost free of CDM-related sampling uncertainties and are, therefore, not addressed here (see Wallace et al., 2009).

The second section explains the experimental design and simulation of BBR measurements. The third section describes how uncertainties for mean radiances arise due to the rotating CDM. Results are presented in the fourth section, and conclusions in the final section.

2.2 Simulation of BBR measurements

In order to achieve spatially accurate BBR point-spread function (PSF) integrations coupled with sampling separation distances d_s, BBR measurements were simulated by averaging high-resolution Landsat-8 imagery. Figure 4.1a shows the PSF resolved at Landsat-8's resolution of 0.03 km. At 50% of the PSF's integrated energy, BBR "pixels" are ~0.58 km across, and their centers are separated across-track by 0.58 km also. At the CDM's full (i.e., nominal) rotation rate, one revolution of the CDM takes ~0.23 s (Caldwell et al., 2017a). As shown in Figure 4.1b, each telescope has four exposures per revolution: two each for the TW and SW bands. Hence, with EarthCARE travelling at ~7.21 km s^{-1}, successive nadir-view pixels with the same wavelength will have $d_s \approx 0.8$ km. Obviously, adjusting CDM rotation rate will impact d_s. Figure 4.1c shows conditions at half the CDM's nominal rate. A detailed description of EarthCARE's BBR can be found in Wallace et al. (2009).

Landsat-8 Bands 5 (0.845 - $0.885\,\mu$m; 0.03 km pixels) and 10 (10.6 - $11.2\,\mu$m; 0.1 km pixels) were used to construct approximate, unfiltered BBR SW and LW radiances; thus assuming a perfect spectral response. Broadband SW radiances R_{SW}, at 0.03 km resolution, were approximated by scaling Landsat-8's Band 5 radiances by the ratio between broadband to Landsat-8's filtered spectral incidence at TOA. Also, radiances were then scaled to correspond to a solar zenith angle θ_0 of 23° which is the smallest for EarthCARE's orbit. Broadband LW radiances R_{LW}, at 0.1 km resolution, were approximated by estimating Planck effective temperatures from Landsat-8's Band 10, using them in the Stefan-Boltzmann equation to get broadband fluxes, multiplying them by a broadband effective transmittance of 0.65, and dividing by π to get back to radiance. R_{SW} and R_{LW} are clearly approximations, but what is important here is that, once integrated over PSFs, they are *close* to expected BBR values and exhibit *realistic* spatial fluctuations. Totalwave radiances are $R_{TW} = R_{SW} + R_{LW}$.

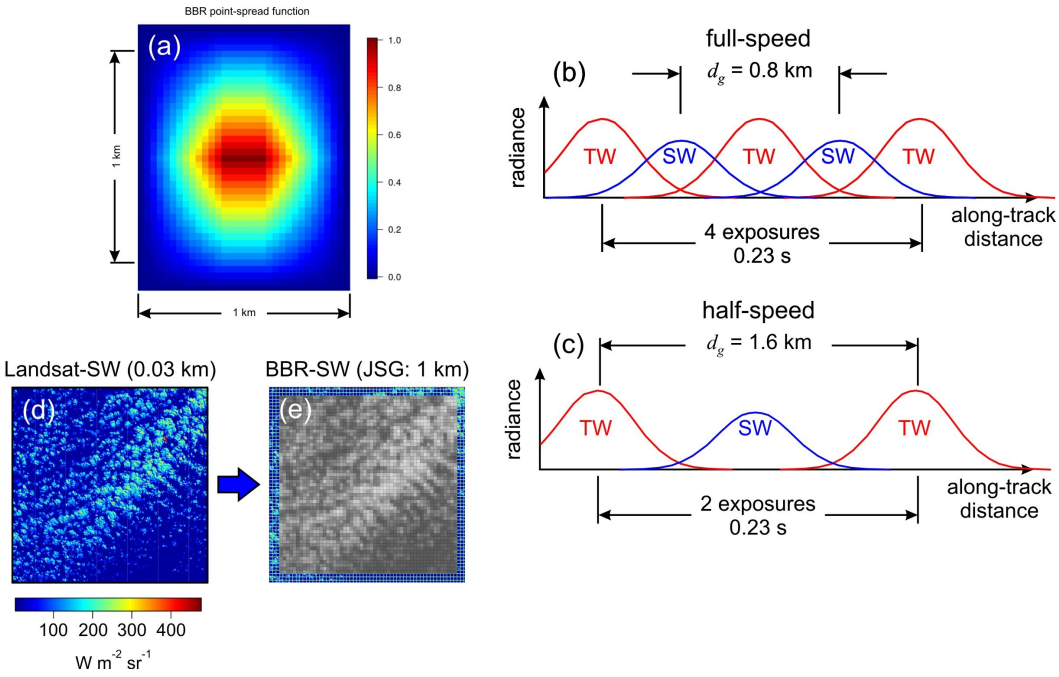

Fig. 2.1: (a) Approximate representation of a BBR Point Spread Function for 0.03 km Landsat imagery. (b) Schematic of alternating TW and SW PSFs at the BBR CDM nominal rotation rate. (c) As in (b) except this is for half the nominal rate. (d) A $(58.4\ \text{km})^2$ Landsat Band 5 sample image, and (e) its integration and interpolation to $(1\ \text{km})^2$ (EarthCARE's JSG).

After integrating R_{SW} and R_{TW} for each PSF they get interpolated onto a 1 km grid which approximates EarthCARE's Joint Standard Grid (JSG). The JSG is what most of EarthCARE's products will be reported on (see Figure 4.1d and Figure 4.1e). Finally, JSG-level BBR radiances are averaged over assessment domains which were originally planned to be $(10\ \text{km})^2$ but will likely be closer to $\sim$5 km across-track by $\sim$21 km along-track (Illingworth et al., 2015; Barker et al., 2014a).

2.3 Definitions and general considerations

Let $\langle S \rangle$ and $\langle T \rangle$ be assessment domain-average SW and TW radiances as would be measured by the BBR. Their errors are

$$\delta\langle S \rangle = \langle S \rangle - \langle \mathrm{S} \rangle \tag{2.1}$$

and

$$\delta\langle T \rangle = \langle T \rangle - \langle \mathrm{T} \rangle \tag{2.2}$$

where ⟨S⟩ and ⟨T⟩ are true domain-averaged SW and TW radiances - arithmetic averages of all R_{SW} and R_{TW} across an assessment domain. Since LW radiances are not measured, domain-average LW BBR radiance $\langle L \rangle$ is defined as

$$\begin{aligned} \langle L \rangle &\equiv \langle T \rangle - \langle S \rangle \\ &= [\langle L_T \rangle + \langle S_T \rangle] - \langle S \rangle \\ &= \langle L_T \rangle - [\langle S \rangle - \langle S_T \rangle] \\ &= \langle L_T \rangle - \Delta_{TS} \langle S \rangle \end{aligned} \tag{2.3}$$

where the subscript T indicates LW and SW radiances that comprise the TW PSFs. $\Delta_{TS}\langle S \rangle$ is difference in mean SW radiances due to sampling with the TW and SW bands. Note that in actual operations the SW channel is slightly contaminated by thermal radiation. This is secondary to the issue at hand and has been neglected here (see Velázquez-Blázquez et al., 2017). Figure 4.2 provides a graphic example of how and why, in general, $\Delta_{TS}\langle S \rangle \neq 0$. Presented this way it is easy to see that at the nominal rotation rate $\Delta_{TS}\langle S \rangle$ are likely to be fairly small since sampling along-track is quite dense. If, however, d_s becomes too large and sampling too sparse, $\Delta_{TS}\langle S \rangle$ can be sizable. Hence, error for $\langle L \rangle$ is

$$\delta\langle L \rangle = \langle L_T \rangle - \langle \mathrm{L} \rangle - \Delta_{TS}\langle S \rangle \tag{2.4}$$

where ⟨L⟩ represents true domain-averaged LW radiance - the average of all R_{LW} across an assessment domain. When the sun is down, then by definition $\langle L \rangle \equiv \langle T \rangle$ and $\delta\langle L \rangle = \delta\langle T \rangle$. In fact, since LW radiances usually vary much less than SW radiances, even for moderately large values of θ_0, it can often be expected that

$$\delta\langle L \rangle \approx -\Delta_{TS}\langle S \rangle \tag{2.5}$$

implying that

$$\sigma^2(\delta\langle L \rangle) \approx \sigma^2(\delta\langle S \rangle) + \sigma^2(\delta\langle S_T \rangle) - 2\mathrm{cov}(\delta\langle S \rangle, \delta\langle S_T \rangle) \tag{2.6}$$

When CDM rotation rates are large and d_s are small, it is likely that $\delta\langle S \rangle \approx -\delta\langle S_T \rangle$, meaning that equation 2.6 can be simplified to

$$\sigma(\delta\langle L \rangle) \approx 2\sigma(\delta\langle S \rangle) \tag{2.7}$$

This means that uncertainties in estimated mean LW radiances are approximately, though slightly less than, *double the magnitude* of their SW counterparts, even when LW radiances exhibit no fluctuations at all! This might seem counterintuitive but it is demonstrated in the next section.

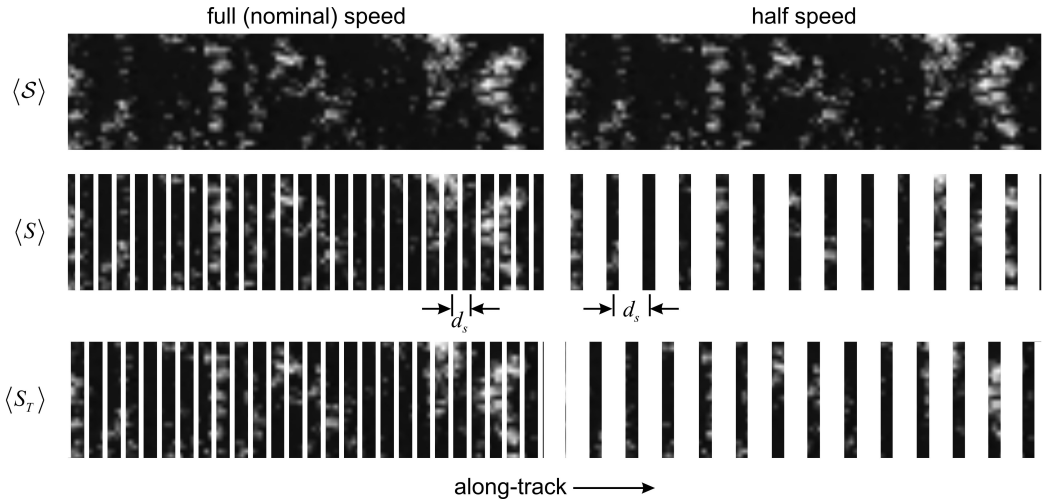

Fig. 2.2: Top frames show a 5 × 21 km assessment domain of full SW radiances R_{SW}, the domain-average being ⟨S⟩ (see equation 2.1). Middle frames show PSF samplings at the BBR's nominal CDM rotation rate and at half the nominal rate. d_s is ground sampling distance. Their domain-averages are $\langle S \rangle$. Lower frames show SW signals seen by the totalwave telescope which samples between successive samples on the middle frames. Cross-track sampling is very good and independent of CDM rotation rate. Hence, it was neglected in order to focus attention on along-track sampling.

2.4 Results

Figure 4.3 shows ten Landsat 8 high-resolution images used in this study. These images adequately represent a wide range of cloud types and radiance variability. The BBR sampling process, described above, was applied to these radiances assuming various CDM rotation speeds. Resulting BBR radiance estimates where compared against “true" mean radiances for designated assessment domain sizes.

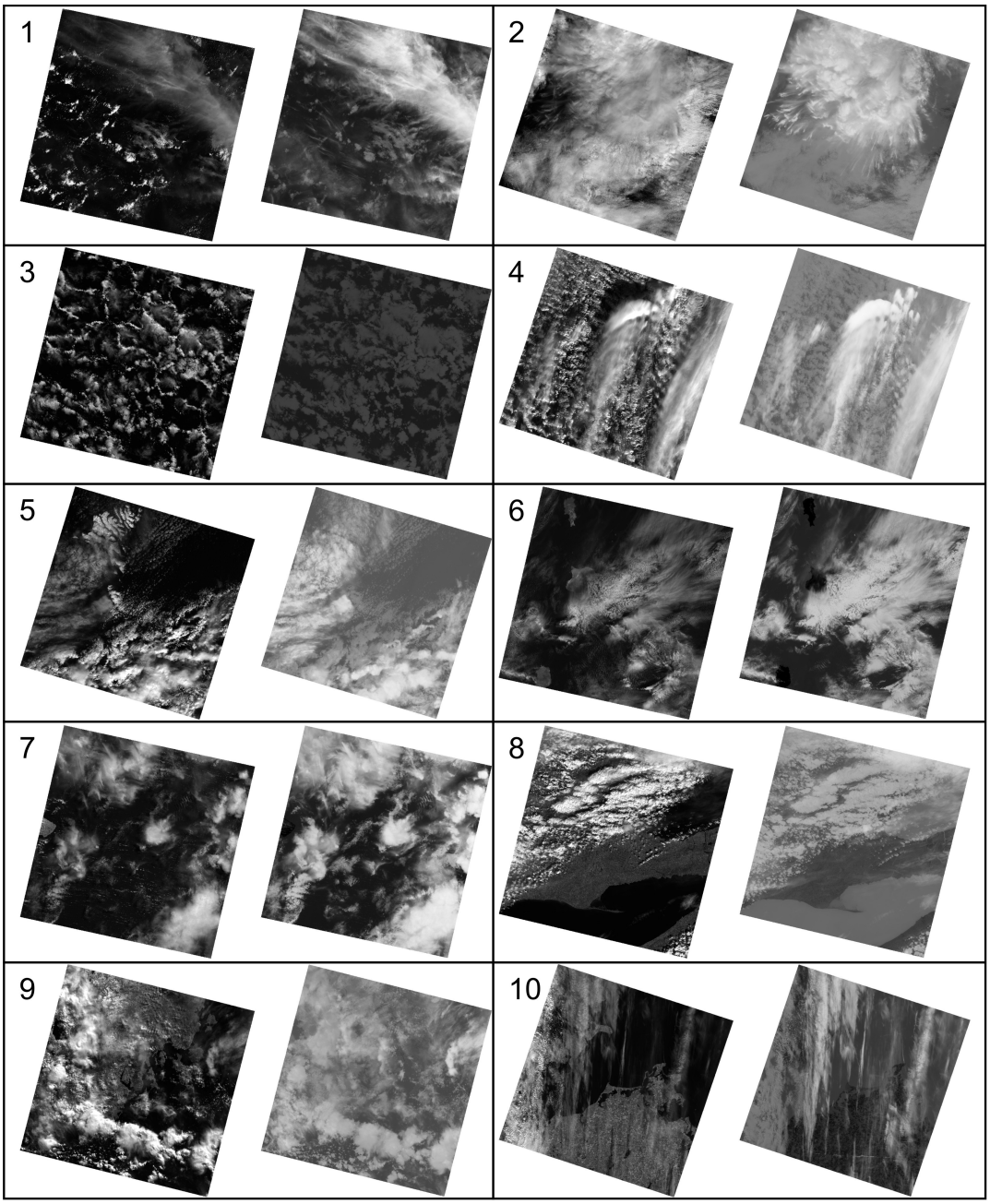

Fig. 2.3: Ten pairs of (left) Landsat Band 5 (0.85 - $0.88\,\mu$m) and (right) Band 10 (10.6 - $11.2\,\mu$m) images used in this study to derive estimates of SW and LW BBR radiances. Each image is 190 km $\times$ 180 km. SW and LW radiances range from 0 (black) to 290 (white) W m^{-2} sr^{-1} and from 25 (white) to 95 (black) W m^{-2} sr^{-1}, respectively. See Table 4.1 for details.

Tab. 2.1: Characteristics of Landsat tiles shown in Figure 3. For domain sizes of 5 × 21 km, perceived heterogeneities (i.e., radiance variability as defined in the text) and mean domain radiances were computed, sorted by SW radiance variability, and grouped into 1-percentile bins. Group averages (shown for percentiles 16, 50, and 84) of radiance variability and mean radiance (in parentheses) for SW, LW, and TW radiances are listed. Values are in W m^{-2} sr^{-1}.

No.	Landsat Scene ID & Location	Description	SW Radiance Variability (SW Radiance Mean)			LW Radiance Variability (LW Radiance Mean)			TW Radiance Variability (TW Radiance Mean)		
			16%	50%	84%	16%	50%	84%	16%	50%	84%
1	LC81330552016355LGN02 6.1-8.3°N, 92.0-94.1°E	sparse cumuli, 30% cirrus, few high convective clouds	7.68 (17.62)	17.99 (28.93)	45.86 (41.85)	4.12 (78.83)	6.15 (74.69)	4.49 (78.76)	5.25 (96.45)	13.91 (103.62)	42.84 (120.62)
2	LC81900192017164LGN00 57.6-59.8°N, 19.0-23.2°E	80% cirrus, above overcasting stratocumulus few high convective clouds	16.82 (92.63)	25.16 (126.38)	42.48 (116.31)	3.52 (62.40)	3.21 (63.56)	4.24 (64.96)	14.30 (155.02)	23.04 (189.93)	40.47 (181.26)
3	LC81940712017160LGN00 14.8-17.0°S, 5.1-7.3°W	no cirrus, 50% cumulus of various structures	21.82 (24.47)	39.84 (44.71)	54.70 (65.06)	2.69 (83.65)	3.21 (82.25)	3.34 (81.20)	19.50 (108.12)	37.15 (126.96)	51.89 (146.25)
4	LC82100172016062LGN01 60.3-62.6°N, 5.5-10.3°W	50% cirrus, 50% cumuli, some high cloud shadows	29.04 (79.87)	41.20 (94.45)	54.64 (103.40)	3.50 (57.09)	3.49 (38.64)	4.73 (58.21)	26.18 (136.96)	50.83 (153.07)	50.83 (161.61)
5	LC82090172016119LGN01 60.3-62.6°N, 4.0-8.7°W	30% cirrus, 30% cumuli, some high convection, some islands	10.63 (16.94)	32.00 (64.37)	64.97 (113.90)	1.96 (67.27)	5.42 (55.35)	6.20 (55.20)	9.08 (84.21)	27.97 (119.72)	60.86 (169.10)
6	LC82090492017073LGN00 14.8-17.0°N, 21.4-23.6°W	50% cirrus, few cumuli, some islands	5.64 (23.82)	19.35 (66.79)	35.33 (98.70)	2.98 (80.49)	6.71 (64.41)	8.42 (55.23)	3.41 (104.31)	14.60 (131.20)	28.22 (153.93)
7	LC82320512017154LGN00 11.9-14.1°N, 57.6-59.8°W	50% cirrus, sparse cumuli, some altostrati	8.28 (23.88)	18.74 (45.58)	37.52 (81.74)	5.12 (81.03)	9.50 (67.37)	9.49 (60.13)	5.50 (104.96)	11.51 (112.95)	29.81 (141.87)
8	LC80180302016077LGN01 42.1-44.2°N, 78.6-81.6°W	50% cumulus and altostratus, mostly land surface	7.19 (38.24)	38.30 (79.31)	70.75 (150.70)	1.60 (71.60)	5.60 (64.58)	6.45 (55.70)	7.15 (109.84)	34.59 (143.89)	65.32 (206.40)
9	LC80900902017247LGN00 42.1-44.2°S, 145.7-148.7°E	50% cumuli, 50% cirrus, 30% land surface	20.09 (49.74)	37.51 (89.30)	66.20 (137.88)	3.83 (65.37)	5.38 (60.09)	5.60 (55.62)	17.83 (115.11)	33.33 (149.39)	61.73 (193.51)
10	LC81940222016270LGN02 53.3-55.6°N, 10.6-14.5°E	50% cirrus mostly land surface of heterogeneous reflectivity	6.70 (17.54)	16.74 (76.37)	28.40 (65.85)	2.82 (74.55)	4.24 (74.84)	4.43 (73.14)	4.06 (92.09)	14.86 (151.21)	27.47 (138.99)

Intuitively, radiance uncertainties due to incomplete sampling should increase as radiances become increasingly heterogeneous across assessment domains. Near-homogeneous fields, such as stratiform decks, where there is little to miss even when sampling is sparse, should present well, while fields of scattered cumulus could be sampled poorly (see Figure 4.2). To explore this, N assessment domains measuring 5×21 km^2 (i.e., one option in EarthCARE's configurable assessment domain size) were sampled randomly from each tile. To isolate heterogeneity effects, assessment domains were grouped by 1-percentile intervals of SW radiance variability σ_{SW}, as defined by the standard deviation of SW radiances within an assessment domain. Finally, within each interval, TOA SW, TW, and LW sampling uncertainties, defined as the standard deviation of differences between sampled mean and true mean radiances, were determined and compared to mission requirements. In order to address sampling uncertainty during the EarthCARE mission, SW variability was based on radiances resolved at 1 km^2 (approximately the size of the EarthCARE's JSG). Sampling uncertainties for SW and TW radiances are discussed first. This is followed by an assessment for the indirectly measured LW radiances.

2.4.1 Uncertainties for SW and TW mean radiances

Figure 4.4 shows how SW sampling uncertainty $\sigma(\delta\langle S\rangle)$ increases with reductions to CDM performance for four tiles of very different composition and magnitudes of sampling uncertainty. Tile 3, characterized by weak TOA SW radiance variability (21.8 - 54.7 W m^{-2} sr^{-1}, see Table 4.1), and tile 7, characterized by smooth filaments of high-level clouds (8.3 - 37.5 W m^{-2} sr^{-1}), lead to small SW uncertainties $\sigma(\delta\langle S\rangle)$ (1.9 and 0.7 W m^{-2} sr^{-1} at lowest performance, respectively) while tiles 4 and 8 have much larger SW uncertainties (2.8 and 3.2 W m^{-2} sr^{-1} at lowest performance, respectively). Tiles with broken low-level cumuli exhibit bright and sharp features which result in large TOA SW radiance variability σ_{SW} of up to 70.8 W m^{-2} sr^{-1} (see Table 1). Hence, SW sampling at largest d_s would produce $\sigma(\delta\langle S\rangle)$ of ~3.2 W m^{-2} sr^{-1}, which when multiplied by π slightly exceeds the mission requirement of 10 W m^{-2} (tile 8 in Figure 4.4).

We believe that varying amounts of TOA SW radiance variability σ_{SW} caused observed variety in TOA SW nadir radiance sampling uncertainty $\sigma(\delta\langle S\rangle)$. Figure 4.5 shows $\sigma(\delta\langle S\rangle)$ as a function of σ_{SW} and ground sampling distance d_s for domains measuring 5 km across-track and 21 km along-track. SW uncertainty increases almost linearly with σ_{SW} .

This linear relationship between σ_{SW} and $\sigma(\delta\langle S\rangle)$, shown in Figure 4.5, grows not only progressively steeper, but also noisier due to progressively larger gaps between BBR along-track SW footprints as d_s increases. To understand the effects of sparser along-track SW footprints, BBR sampling was done repeatedly on the

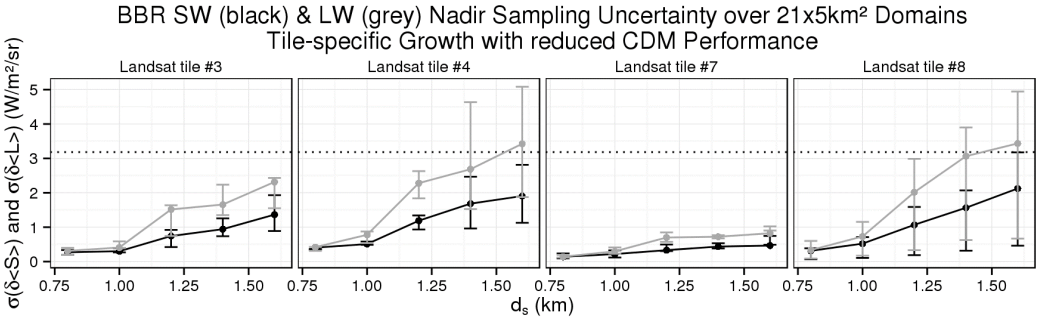

Fig. 2.4: BBR LW (gray) and SW (black) uncertainties as functions of CDM rotation rate expressed as d_s for 5 $\times$ 21 km domains. Lines indicate median levels of tile-specific SW radiance variability while bar ends denote 16$^{\text{th}}$ and 84$^{\text{th}}$ percentiles. Dotted horizontal line indicates 10 W m^{-2} (mission required flux accuracy) divided by π.

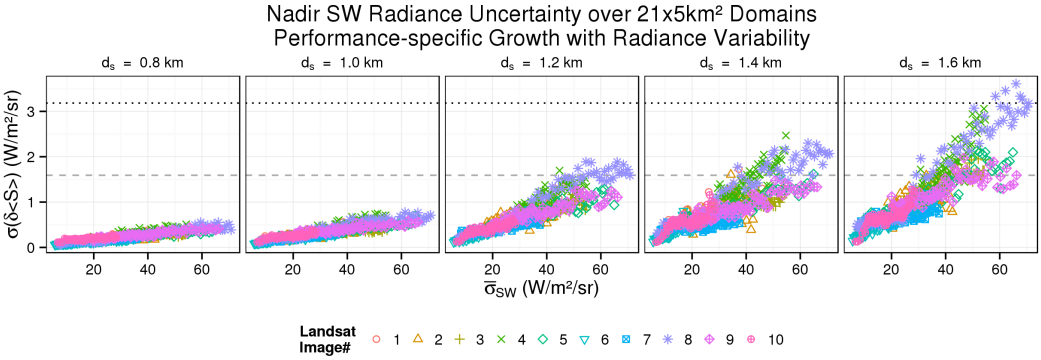

Fig. 2.5: BBR SW uncertainty as functions of SW radiance field heterogeneity for 5 $\times$ 21 km domains for various values of d_s as indicated above each plot. Radiance variability percentiles, 16 through 84, are shown for each tile. As in Figure 4.4, black dotted lines indicate mission requirements. Assuming LW uncertainties to be roughly twice the SW uncertainties (see equation 2.7), gray dashed lines mark $5/\pi$ W m^{-2} sr^{-1} which indicates the mission required limit for LW radiances uncertainties.

central 50 km $\times$ 50 km portion of tile 5 to obtain several values of interpolated SW radiances and SW errors for each 1 km^2 cell. The standard interpolation method was used: all overlapping SW footprints and their two-dimensional PSFs resolved at 30m were considered; each PSF was weighted by the PSF energy overlapping with the cell; and all weighted PSFs were merged onto a horizontal field and normalized to integrate to 1. In addition to interpolating SW radiances, the amount of energy of the normalized PSF falling into each cell was determined. Cell coverage was defined as the integral of normalized PSF values within a cell's perimeter. Hence, a coverage of "1" translates into to BBR sampling only within the cell, while a value of "0" corresponds to no BBR footprint within the grid cell at all. Neither extreme was observed as dense across-track samples always extended beyond cell perimeters (leading to a coverage < 1), and – even at a ground sampling distance of 1.6 km – each cell was partly sampled by at least one SW exposure (a coverage > 0). Similar to σ_{SW}, sub-grid variability was extracted per grid cell based on 30m resolved radiances. Figure 4.6 shows how 1 km^2 sampling errors (y-axis) grew with sub-grid variability (x-axis) and with lower coverage (darker colors). At lowest d_s, coverage varied between 0.6 and 0.7 and errors remained within $\pm$15 W m^{-2} sr^{-1} (i.e. the 16$^{\text{th}}$ and 84$^{\text{th}}$ error percentiles at highest sub-grid variability), while greatest d_s led to a larger spread in coverage (between 0.1 and 0.7) and produced overall larger errors ($\pm$30 W m^{-2} sr^{-1}). Assembled to 21 $\times$ 5 km domains, such sampling errors can partly compensate as one cell's overestimation can outweigh a neighboring cell's underestimation. However, especially at larger d_s, neighboring cells presented a contrast in PSF coverage (not shown) preventing such error compensation: the high coverage ($\sim$0.7) of one cell (producing a low sampling error) was accompanied by a poor coverage ($\sim$0.1) of along-track neighbors thereby generating large sampling errors. To conclude, SW errors have shown to grow with more heterogeneous coverage through SW footprints - resulting from increased d_s - and that can attribute to steeper slopes of radiance uncertainties over 21 $\times$ 5 km domains against radiance variability, as well as increased noise around slopes.

Summarizing above observations, as BBR SW sampling becomes sparse, radiance uncertainties increase (up to 3.2 W m^{-2} sr^{-1}), especially for very heterogeneous radiance fields. Thus, only extreme conditions (50% CDM performance and largest radiance variabilities) led to critical levels of uncertainty which exceed mission requirements of 10 W m^{-2} when transformed into fluxes. The same goes for TW sampled radiances (not shown) with TW uncertainties reaching 4.1 W m^{-2} sr^{-1}. As an alternative to domain size of 5 $\times$ 21 km, 10 $\times$ 10 km domains were considered, too. Their SW and TW uncertainties (not shown) were up to 10% larger. For larger solar zenith angles, SW and TW uncertainties would be smaller and their flux equivalents would likely comply with mission requirements at CDM rotation rates between 50% and 100% of the nominal rate.

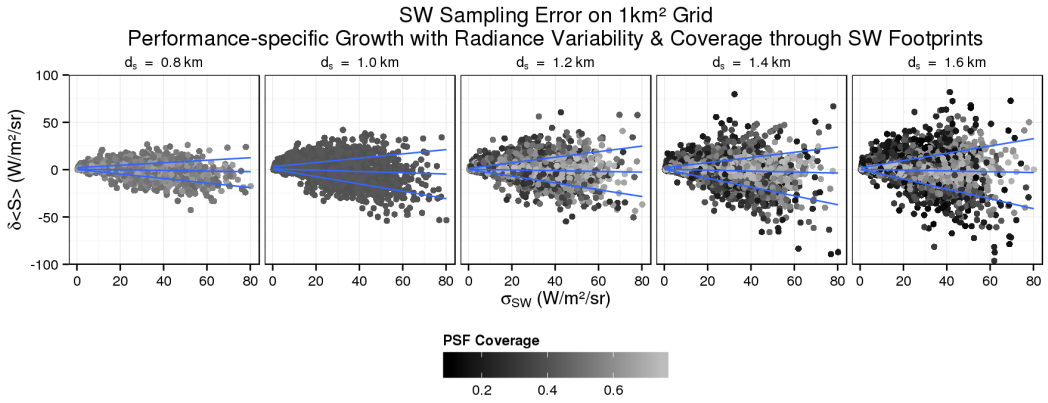

Fig. 2.6: For various d_s (as indicated), BBR radiance errors over 1 km^2 grid cells as functions of sub-grid variability. Values were extracted from the central portion of tile 5 as described in the text. Blue lines mark quantile regression of 16$^{\text{th}}$, 50$^{\text{th}}$ and 84$^{\text{th}}$ error percentiles.

2.4.2 Uncertainties for LW mean radiances

In contrast to the previous subsection, LW radiances are not directly observed, but rather inferred from staggered measurements of TW and SW radiances. In effect, the methodology relies on a dense sampling through both modes. According to equation 2.7, LW uncertainties $\sigma(\delta\langle L\rangle)$ are expected to be twice as large as $\sigma(\delta\langle S\rangle)$, especially, and counterintuitively, when LW radiance heterogeneity is much smaller than its SW counterpart. Figure 4.4 shows how TOA LW radiance uncertainties generally exceed and follow the rise of SW radiance uncertainties. As a result, sampling at $d_s \geq 1.4$ km over tiles 4 and 8 produce LW uncertainties that exceed mission requirements when transformed into LW fluxes.

At $d_s = 1.2$ km, LW uncertainty jumps, occasionally accompanied by an abrupt rise in SW uncertainty (e.g., tiles 3 and 4). Figure 4.7 confirms that the ratio of LW to SW uncertainty increases with d_s, peaking at $\sim$1.2 km with ratios near 2. A doubling of SW uncertainties at $d_s = 1.2$ km - or a 33% performance reduction - would result in non-compliant LW uncertainties (see the central panel of Figure 4.5). Neither levels of σ_{SW} nor σ_{LW} can explain error ratio fluctuations (see point size and colors in Figure 4.7). Additionally, it was verified that 10 $\times$ 10 km assessment domains have almost identical relationships (not shown).

Following this, we investigated why the LW inference process (i.e. subtracting sampled SW from TW radiances to gain LW radiances) was sensitive to CDM performance and effectively the along-track distance between subsequent TW and SW footprints. We extracted additional information from the central portion of tile 5 (complementing extracted variables in section 2.4.1) on a 1 km^2 grid: we measured the size of SW-TW footprint overlaps; the coherence of SW and TW PSF weights;

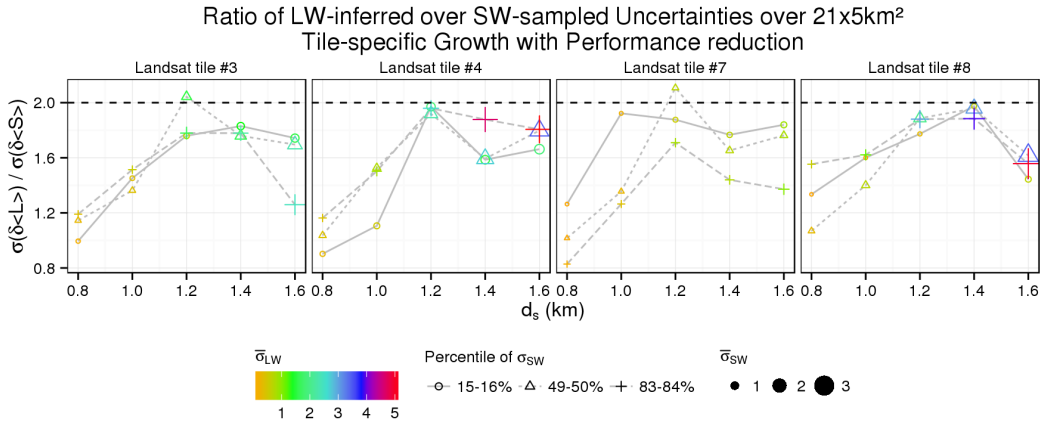

Fig. 2.7: Ratio of LW radiance uncertainties to SW radiance uncertainties as functions of d_s and a domains size of 5 $\times$ 21 km. SW heterogeneity is represented by dot size and LW heterogeneity by dot color. Dashed horizontal lines mark the theoretical ratio of 2 as predicted by equation 2.7.

and the resulting error of BBR-inferred LW radiance. Overlap size is determined through the integral of SW plus TW PSF weights (resolved at 30m, again each footprint weighted for interpolation, and across both SW and TW PSFs normalized to integrate to 1) of all relevant footprints (i.e. all SW and TW footprints which intersect the grid cell) integrated only within the overlap area (i.e. the area where both SW and TW weights are non-zero). A theoretical maximum of “2" would be reached if SW and TW were sampled simultaneously, while “0" indicated no overlap at all (impossible at $d_s \in [0.8\text{ km}, 1.6\text{ km}]$). Observed maximum values of about 1 (at a d_s of 0.8 km) shows that SW and TW PSF effectively overlapped by about 50%. Coherence of SW-TW PSF weights was measured as the covariance of SW and TW PSF weights within the overlap area, denoted “PSF Covariance". Lowest (negative) covariances were observed for d_s of 1.2 km and indicated that locally high SW PSF weights coincided with low TW PSF weights, and vice versa. Figure 4.8 shows how 1 km^2 SW errors (x-axis with same values as y-axis of Figure 4.6) corresponded to LW errors (y-axis) for different d_s and effectively different levels of PSF overlap size (dot size) and PSF covariance (dot color). For a d_s of 0.8 km, we found largest overlap sizes (approximately 1) and covariances (about 3E-8). The corresponding slope between LW and SW errors (shown as a blue line and annotated in the plot) was -0.3. Steepest slopes (approximately -1.2) were found for d_s of 1.2 km and higher. Overlap size was generally smaller (mean $<$0.77) and co-variances lower (mean $<$0). LW errors with smallest overlap sizes (about 0.2, shown as smallest points) correspond to even steeper slopes. In conclusion, we showed that SW errors translated into larger LW errors (i.e. a larger LW/SW error ratio) when SW and TW footprints overlapped less and their PSF weights were less coherent.

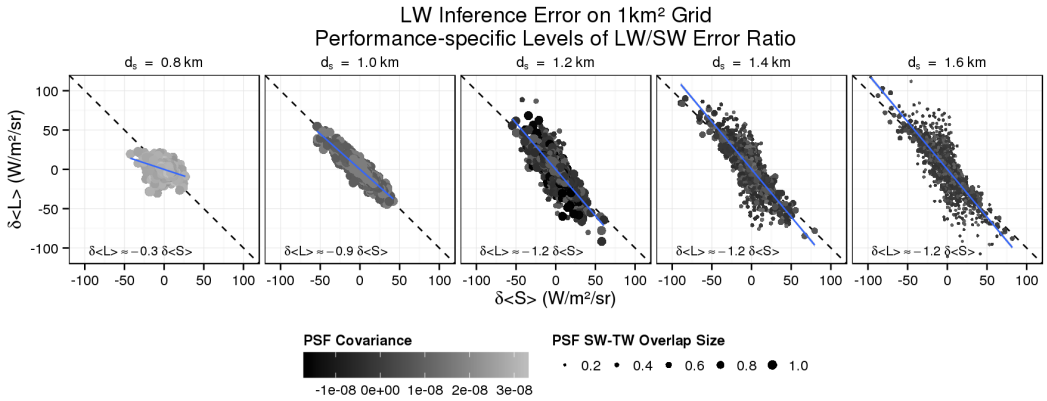

Fig. 2.8: 1km^2 LW errors as functions of SW errors for different CDM performances. Colors mark the covariance of SW and TW PSF weights, while dot size indicates the size of their footprint overlap (extracted as described in the text). Blue line and annotations highlight the LW-SW error ratio.

In summary, it has been confirmed that, according to equation 2.7, LW uncertainties are about twice as large as SW uncertainties (at $d_s \geq 1.2$ km or performance reduction $\geq 33\%$) due to the sensitive nature of LW inferences from staggered SW and TW sampling. To remain within mission requirements and to ensure that LW uncertainties when converted to LW fluxes fall below 10 W m^{-2}, CDM performance should not be reduced beyond 25% (i.e., $d_s \leq 1.0$ km). Again, smaller LW uncertainties can be expected for smaller SW uncertainties - arising from, for example, large solar zenith angles.

2.5 Conclusion and discussion

The overall goal of the EarthCARE satellite mission is to retrieve cloud and aerosol properties well enough that when acted upon by radiative transfer models, estimated TOA fluxes for each ∼100 km^2 domain will be within 10 W m^{-2} of fluxes inferred from BBR measurements (ESA, 2001; ESA, 2006). Similarly, BBR radiances can be used directly in EarthCARE's radiative closure assessment. For a closure either through fluxes or radiances, it is essential that BBR radiance uncertainties be accounted for. Considering in-orbit adjustable CDM rotation rates, which when reduced will extend instrument lifetime but also decrease along-track sampling rate, it is important to find a compromise between lifetime and required radiometric accuracy. This study analysed sampling uncertainties arising from both reduced CDM performance and horizontal heterogeneity of radiance fields.

Using high-resolution Landsat 8 scenes, SW, TW, and LW sampling errors were quantified for assessment domains of 5 × 21 km and various CDM rotation rates. It was found that SW and TW sampling uncertainties are related approximately

linearly to sample heterogeneity and increase with reduced instrument performance (at lowest performance SW and TW uncertainties reached 3.2 W m^{-2} sr^{-1} and 4.1 W m^{-2} sr^{-1} for scenes with the greatest radiance variabilities of 70.8 W m^{-2} sr^{-1} and 65.3 W m^{-2} sr^{-1}, respectively). LW are inferred from staggered SW and TW radiances, and their uncertainties scaled with SW uncertainties by a factor $\sim$2 for $\geq$ 33% performance reductions, even though LW fields exhibited much less variability. It was shown that critical LW uncertainties (exceeding 10 W m^{-2}) were achieved when performance was reduced by more than 25% from the nominal rate.

Previous radiance error assessments focused on radiance unfiltering (Velázquez-Blázquez and Clerbaux, 2010). It has been shown here that uncertainties arising from the BBR's sampling strategy represent a previously unrecognized source of uncertainty. Both unfiltering and sampling errors can reach similar magnitudes. Future research should examine whether these are independent sources of error.

As a final comment, it is interesting to note that had a lens filter been available that allowed LW, rather than SW, radiances to be measured directly, uncertainties for LW radiances would be much reduced with only minor increasees in SW uncertainties relative to the BBR's configuration. Recent payloads (e.g., RBI on JPSS-2[1], Mariani et al., 2016) offer such filter. Alternatively, LW errors can be mitigated through simultaneous TW and SW measurements (e.g. CERES, Wielicki et al., 1996) thereby avoiding effects due to staggered measurements of radiances.

Acknowledgements

This study was supported by a contract issued by the European Space Agency, under the EarthCARE component of its Living Planet Programme, to the Freie Universitä Berlin that was subsequently subcontracted to Environment and Climate Change Canada, the Royal Meteorological Institute of Belgium, and GMV. The authors wish to thank Tobias Wehr of ESA for helpful discussions.

[1]Earth Science Sensor set cancelled through NASA:
www.nasa.gov/feature/nasa-cancels-earth-science-sensor-set-for-2021-launch

3

On the use of geophysical parameters for the top-of-atmosphere shortwave clear-sky radiance-to-flux conversion in EarthCARE

Abstract

We have investigated whether differences across CERES (Clouds and the Earth's Radiant Energy System) Top-Of-Atmosphere (TOA) clear-sky angular distribution models, estimated separately over regional ($1° \times 1°$ longitude/latitude) and temporal (monthly) bins above land, can be explained by geophysical parameters from MAC-v1, ERA20C, and a MOD43B climatology. Our research aimed to dissolve binning and to isolate inherent properties or indicators of such properties which govern the TOA radiance-to-flux conversion in the absence of clouds. We colocated several months of CERES SSF Edition 4 data with auxiliary data from MAC-v1, ERA20C, and a MOD43B climatology. Looking at data per surface type and per scattering direction - as perceived by the broadband radiometer (BBR) on board EarthCARE (Earth Clouds, Aerosol and Radiation Explorer) - we identified optimal subsets of geophysical parameters and trained Artificial Neural Networks (ANNs). Flux error standard deviations on test data were on average 2.7 – 4.0 W m^{-2}, well below the 10 W m^{-2} flux accuracy threshold defined for the Mission, with the exception of footprints containing fresh snow. Dynamic surface types (i.e. fresh snow and sea ice) required simpler ANN input sets to guarantee mission-worthy flux estimates, especially over footprints consisting of several surface types.

Tornow, F., Domenech, C., Fischer, J.,
submitted to Journal of Atmospheric and Oceanic Technology, May 2018, in revision

3.1 Introduction

In the absence of clouds, Earth's surface and atmospheric constituents (i.e. absorbing gases and scattering and absorbing aerosols) govern the angular distribution of back-scattered solar radiation perceived at Top-Of-Atmosphere (TOA). Any unforeseen spatial or temporal variations of the surface's appearance (such as the surface roughness of a water body or the vegetation state over land) as well as atmospheric composition (such as aerosol plumes or ozone variations) may translate into an uncertainty for a radiance-to-flux conversion.

The gold standard of angular distribution models has been provided by the CERES team (Su et al., 2015a) and is widely applied to other satellite missions performing broadband radiometry (Viollier et al., 2009; Dewitte et al., 2008). The upcoming ESA-JAXA mission EarthCARE (Illingworth et al., 2015), to be launched in 2020, will be equipped with a broadband radiometer (BBR; e.g. Wallace et al., 2009; Caldwell et al., 2017b) observing nadir as well as along-track forward and backward (both at 55° viewing zenith angle). Apart from monitoring TOA fluxes, the mission will conduct a radiative closure assessment, comparing BBR-derived longwave (LW) and shortwave (SW) flux estimates with simulated fluxes. Broadband simulations will act on active-passive retrievals of cloud and aerosol vertical profiles along the swath (Barker et al., 2011). Agreement between measurement and simulation-based fluxes (within 10 W m^{-2} over 100 km^2 horizontal assessment domains) translates into confirmed understanding of cloud-aerosol-radiation interaction and, ultimately, into trusting simulated vertical heating rate profiles. In the closure assessment, clear-sky scenes will pose less of a challenge. However, simulation biases - arising e.g. from poorly characterized surface or aerosol spectral properties - could easily be identified in a comparison to BBR-derived clear-sky fluxes.

To account for the complex nature of bi-directional reflectance distribution over clear-sky scenes, the CERES team built regional (resolved at $1°\times1°$ latitude/longitude cells) and temporal (resolved by calendar month) angular distribution models over land surfaces (CERES SSF Edition 4; Su et al., 2015a). In this study, we investigate whether additional geophysical variables could help to dissolve regional and temporal binning. We co-locate several data sets characterizing land and atmosphere with CERES instantaneous observations. We identify essential subsets for each surface type and scattering direction to serve as input for radiance-to-flux converting ANNs. Finally, we propose operational modifications for EarthCARE.

Tab. 3.1: A list of extracted CERES footprints, obtained after filtering for clear-sky and BBR-like conditions.

Year	No. of CERES footprints Terra (FM1 & FM2)	Aqua (FM3 & FM4)	Mode
2000	108828	/	FAPS
2001	208492	/	FAPS
2002	207365	67024	FAPS
2003	222016	208360	FAPS
2004	215843	274869	FAPS
2005	25655	25224	FAPS
2006	/	/	/
2007	2892051	2819907	cross-track

3.2 Data and Methodology

3.2.1 CERES SSF Edition 4

We obtained instantaneous TOA SW anisotropies - denoted as $\Re$ throughout this paper - from CERES SSF (Single Scanner Footprint TOA/Surface Fluxes and Clouds) Edition 4, along with parameters on viewing and illumination geometry (i.e. solar zenith angle θ_S, relative azimuth angle φ, and viewing zenith angle θ_V) as well as IGBP (International Geosphere-Biosphere Programme) types and their fraction within each footprint. MODIS (Moderate-resolution Imaging Spectroradiometer) cloud fraction served to filter out clear-sky footprints (i.e. $\leq$0.1% cloud fraction), and VZA (viewing zenith angle) was used to select BBR-like viewing geometries (i.e. $\theta_V \leq 2.5°$ and $52.5° \leq \theta_V \leq 57.5°$).

Anisotropy estimation over clear-sky scenes is thoroughly described in Su et al. (2015a). In short, angular distribution models (ADMs) over water surfaces were generated per interval of prevailing MODIS-based Aerosol Optical Depth (AOD) and aerosol fine mode fraction, as well as 10 m wind speed. Sun-glint affected geometries were handled separately. ADMs over land surfaces were established individually for each grid box (1° latitude by 1° longitude) and calendar month. Intervals of MODIS-based NDVI (Normalized Density Vegetation Index) and surface elevation variability received further individual treatment. ADMs over snow and ice surfaces were produced based on intervals of respective surface type fraction as well as bright and dark categories. Talbe 4.1 lists details on extracted footprints from both Aqua and Terra missions.

3.2.2 Co-located Data

All footprints listed in Table 4.1 were spatially and temporally co-located via the nearest neighbor approach with median total AOD from the MAC-v1 climatology (resolved at 1° latitude/longitude and monthly steps; Kinne et al., 2013) and a selection of atmospheric and surface parameters from ERA-20C (using the years 2000-2007; resolved at T159 spectral or about 125 km spatial resolution, and 3 h temporal resolution; Poli et al., 2016). We selected ERA-20C parameters that characterize the appearance of surface or atmosphere and therefore potentially explain TOA SW anisotropy variations. Based on 12 years (2002-2013) of MCD43GF data (Moody et al., 2008), we use a climatology (at 1 km^2 spatial and 16-day temporal resolution; pers. comm. Zhipeng Qu) of RossThick-LiSparse kernel weights (e.g. Lucht et al., 2000) to serve EarthCARE level-2 processors. We co-located kernel weights according to each CERES footprint's field-of-view and resulting point spread function (detailed description in Wielicki et al., 1996). From kernel weights in visible (VIS, 0.3-0.7 μm and near-infrared (NIR, 0.7-5.0 μm) spectra, we calculated surface reflectance (equation 4.1, shown for VIS reflectance r^{VIS}) and albedos for both black- and white-sky conditions (equation 4.2, shown for VIS white-sky albedo a_w^{VIS}). Finally, we produced Bottom-Of-Atmosphere (BOA) anisotropy corresponding to each footprint's viewing and illumination geometry (equation 4.3, shown for VIS white-sky anisotropy R_w^{VIS}). K_{geo} and K_{vol} correspond to geometric and volumetric kernels, respectively.

$$r^{VIS}\pi = f_{iso}^{VIS} + f_{vol}^{VIS}K_{vol}(\theta_S, \theta_V, \varphi) + f_{geo}^{VIS}K_{geo}(\theta_S, \theta_V, \varphi) \tag{3.1}$$

$$a_w^{VIS} = f_{iso}^{VIS} + 0.189184 f_{vol}^{VIS} - 1.377622 f_{geo}^{VIS} \tag{3.2}$$

$$R_w^{VIS} = \frac{r^{VIS}\pi}{a_w^{VIS}} \tag{3.3}$$

All co-located parameters are listed in Table 4.2. We also computed two bi-directional reflectance effects. The hotspot effect $1 + F(G)$ was computed as shown in Rahman et al. (1993) (using MCD43GF-based VIS surface reflection under zenith illumination and zenith viewing conditions r_0, as well as instantaneous viewing and illuminations angles):

$$1 + F(G) = 1 + \frac{1 - r_0}{1 + G} \tag{3.4}$$

where

$$G = (\tan^2\theta_S + \tan^2\theta_V - 2\tan\theta_S \tan\theta_V \cos\varphi)^{\frac{1}{2}} \tag{3.5}$$

$$r_0 = (f_{iso}^{VIS} + f_{vol}^{VIS}K_{vol}(0,0,\varphi) + f_{geo}^{VIS}K_{geo}(0,0,\varphi))/\pi \tag{3.6}$$

Tab. 3.2: A list of co-located geophysical parameters to each CERES footprint, listed in Table 4.1.

Source	Parameter	Spatial & Temporal Resolution	Co-registration Type
ERA-20C (Poli et al., 2016)	Total Column Ozone Total Column Water Vapour Leaf Area Index High Veg. Leaf Area Index Low Veg. 10m U Wind Component 10m V Wind Component Forecast Surface Roughness Charnock Snow Depth Sea-Ice Cover	∼125km (T159); 3 hourly	nearest neighbour
MAC-v1 (Kinne et al., 2013)	Median Total AOD	1° Lat./Lon.; monthly	nearest neighbour
MCD43GF (Moody et al., 2008) (a climatology based on the years 2002-2013; pers. comm. Zhipeng Qu)	VIS isotropic model parameter f_{iso}^{VIS} VIS volume-scattering model param. f_{vol}^{VIS} VIS geometric-scattering model param. f_{geo}^{VIS} NIR isotropic model parameter f_{iso}^{NIR} NIR volume-scattering model param. f_{vol}^{NIR} NIR geometric-scattering model param. f_{geo}^{NIR}	1km; 16-day	nearest in time; weighted areal average according to CERES instantaneous PSF

The sun-glint reflectance r_g (Cox and Munk, 1954) was computed as shown in Wald and Monget (1983) (essentially using ERA-20C 10 m wind speed $W_{10m} = (U_{10m}^2 + V_{10m}^2)^{1/2}$, the Fresnel reflection factor $\rho(\omega)$ for a perfectly smooth surface, and above instantaneous illumination and viewing angles):

$$r_g = \frac{\pi\rho(\omega)P(\theta_n, W_{10m})}{4\cos\theta_S \cos\theta_V \cos^4\theta_n} \tag{3.7}$$

where

$$P(\theta_n, W_{10m}) = \frac{1}{\pi\sigma^2}\exp\left(-\frac{\tan^2\theta_n}{\sigma^2}\right) \tag{3.8}$$

$$\sigma^2 = 0.003 + 0.00512W_{10m} \tag{3.9}$$

$$\theta_n = \arccos\left(\frac{\cos\theta_V + \cos\theta_S}{2\cos\omega}\right) \tag{3.10}$$

$$\cos 2\omega = \cos\theta_V \cos\theta_S + \sin\theta_V \sin\theta_S \cos\varphi \tag{3.11}$$

3.2.3 The Importance of Variables

To measure the importance of variables, one generally attempts to identify an optimum subset $\Gamma \in X = \{x_1, \ldots, x_N\}$ of regressors x_i (also referred to as independent parameters where X denotes the full set of parameters) to predict the regressand y (also known as the dependent parameter, in this study TOA SW anisotropy $\Re$). We examined the importance of variables in two different ways. First, we applied Random Forest Regression (thoroughly described in Breiman, 2001). In short, a Random Forest consists of T decision trees (here $T = 25$) and, once trained, provides a constant predicted value $\tilde{y}$ at each end of each tree (essentially, an estimate $\tilde{y} = f(\Gamma_{RF}) = \tilde{y}|\Gamma_{RF}$, where Γ_{RF} is the Random Forest essential subset). To train the Random Forest, regressors were searched in several rounds for optimum split nodes to further refine each tree's structure and ultimately reduce errors of predictions (i.e. $\tilde{y}$ is the mean of predicted values $\tilde{y}_1(m), \ldots, \tilde{y}_T(m)$ from all trees for a sample m). To identify the essential subset, we then used a permutation test (Strobl and Zeileis, 2009) to measure the increase in Root Mean Square Deviation $\Delta RMSD$ of predictions with one permutated regressor (where an individual tree's prediction was $\tilde{y}_{t;x_i}$ for x_i permutated) against a prediction with non-permutated regressors over M random samples (here $M = 1000$). Generally, an irrelevant regressor x_i should

produce $\Delta RMSD = 0$, while an important x_i (providing at least one important split-node in at least one tree) should give $\Delta RMSD > 0$.

$$\Delta RMSD(x_i) = \sqrt{\frac{\sum_{m=1}^{M}\left(\left[\frac{1}{T}\sum_{t=1}^{T}\tilde{y}_{t;x_i}(m)\right] - y(m)\right)^2}{M-1}} - \sqrt{\frac{\sum_{m=1}^{M}\left(\left[\frac{1}{T}\sum_{t=1}^{T}\tilde{y}_{t}(m)\right] - y(m)\right)^2}{M-1}} \quad (3.12)$$

Repeated 100 times, we identified parameters with a distribution of $\Delta RMSD$ significantly larger (one-sided t-test with $p < 0.1$) than the $\Delta RMSD$ of an irrelevant variable. We assume these parameters have meaningfully contributed to the construction of the Random Forest and the regression.

Second, we used Genetic Algorithms wrapping multi-linear regression (described in e.g. Mehmood et al., 2012) to build a multi-linear model $\tilde{y} = f(\Gamma_{LM}) = \Gamma_{LM}^T w$, where Γ_{LM} is the optimal subset of geophysical parameters for a linear model (superscript T indicates its transpose) and w are the least square weights to approximate $\tilde{y}$, here TOA SW anisotropy $\Re$. The optimal subset Γ_{LM} is identified using a survival-of-the-fittest method, inspired by biological evolution theory. Starting with an initial population of linear models - each with a random binary string of length N indicating participation of a regressor x_i ("0" or "1" to exclude or include from the linear model, respectively) - fitter models (evaluated by a fitness function, here through the Bayesian Information Criterion) are more likely to survive into the next round. From all survivors, new linear models can be added to the population through mutation (i.e. the random switch of a bit from 0 to 1, or vice versa, in the binary string of a surviving model) or crossover (i.e. the random unification of two surviving binary strings from two models). The newly generated population is re-evaluated for fitness to determine new survivors, and so on. In the final round the fittest linear model is presumed to consist of set Γ_{LM}. In this study, we identified subsets Γ_{LM}^1 through Γ_{LM}^{100} from 100 repetitions (each using a population size of 500, the Bayesian Information Criterion fitness function, linear ranking-based roulette wheel selection, a mutation probability of 0.01, a crossover probability of 0.95, and an elitism of 3 over maximum 50 iterations as defined in Scrucca et al., 2013). We selected the subset which performed best (i.e. had the lowest $RMSD$) in a cross validation on a separate set (using 25% of the training data) of size M.

$$\Gamma_{LM} = \arg\min[RMSD(\Gamma_{LM}^1), ..., RMSD(\Gamma_{LM}^{100})] \quad (3.13)$$

where

$$RMSD(\Gamma_{LM}) = \sqrt{\frac{1}{M-1}\sum_{m=1}^{M}\left[\Gamma_{LM}^T(m)w - y(m)\right]^2} \quad (3.14)$$

3.2.4 Artificial Neural Networks

Inspired by the biological neural pathways in brains, regression with ANNs aims to connect an input signal (here a subset of geophysical regressors X) to a learned output (here TOA SW anisotropy $\Re$). Such connections (resembling biological synapses) are usually not directly connecting in- and output, but involve at least one intermediate layer (referred to as hidden layer) of nodes (i.e. artificial neurons) - each receiving potential contribution from any neuron of the previous layer (the input layer in cases with only one hidden layer). Through a transfer function (e.g. $\tanh$) the weighted sum of these contributions at each node provides modulated input to the follow-up layer (the output layer in cases with only one hidden layer). Weights (corresponding to synapse strength) are learned through training, most commonly through the back-propagation algorithm. The resulting non-linear regression allows us to approximate progressively complex relations with a growing number of hidden layers. All ANNs in this study consisted of a single hidden layer. Both input and output were standardized before training. To find the optimal number of hidden neurons for each ANN, we repeated training for odd numbers of hidden neurons from 3 to $2J - 1$ (where J is the number of input parameters) and selected the best performer using applied cross-validation (using 33% of the training data).

3.3 Results

To examine whether geophysical auxiliary parameters could explain variation in CERES TOA anisotropy across regional and temporal models, we co-located several million instantaneous clear-sky CERES footprints with an MCD43GF climatology (providing bottom-of-atmosphere anisotropy information), the MAC-v1 aerosol climatology, and ERA-20C re-analysis data (providing information on atmospheric gases and numerous parameters relevant to the state of the surface). In preparation for the EarthCARE mission, we focused on nadir viewing and 55° off-nadir viewing radiance measurements only.

Section 3.3.1 demonstrates the capability of various parameters, such as leaf area index, to serve as predictors for TOA anisotropy and introduces the separate treatment of surface types and scattering directions. In Section 3.3.2 we present optimal parameter subsets for TOA anisotropy estimation and assess performance when they are used in Artificial Neural Networks. Finally, Section 3.3.3 presents limitations and adaptations of this methodology for EarthCARE.

3.3.1 Exploring the capability of geophysical parameters

Earth's surface offers a rich set of characteristic appearances, each with a unique bi-directional reflectance distribution. Similar to previous studies (e.g. Domenech and Wehr, 2011), we used the IGBP surface classification (IGBP, 1992) to separately perform radiance-to-flux conversions over forest (IGBP types 1, 2, 3, 4, and 5), fresh snow (19), sea ice (20), savannah (8 and 9), grassland (10, 11, 12, and 14), shrubland (6 and 7), desert (13 and 16), permanent snow and ice (15), and open water (17) surfaces.

To introduce and demonstrate how powerful co-located and generated geophysical parameters are for the prediction of TOA SW anisotropy, Figure 4.1 shows their application in simple linear models. Note the initial spread in TOA SW anisotropy (y-axis of the left column) - in part resulting from various illumination and viewing geometries. The hotspot parameter (shown in Fig. 4.1a over the Saharan desert) accounted for geometries and partly explained TOA anisotropy variations. BOA VIS white-sky anisotropy (Fig. 4.1b) further explained resulting residuals. The VIS black-sky anisotropy is complementary to the VIS white-sky anisotropy (Fig. 4.1g and 4.1h).

The climatological surface anisotropy might fail to account for inter-annual or non-seasonal changes of land surface characteristics. ERA-20C data could account for this, e.g. through the leaf area index (LAI, shown in Figure 4.1i), potentially serving as a proxy for enhanced volumetric scattering.

Atmospheric gases absorb parts of the solar spectrum, affecting off-nadir views more than nadir views through respective atmospheric path lengths. Total column ozone explained some anisotropy residuals (shown in Figure 4.1f). Aerosols may also scatter and redistribute solar radiation within the upward hemisphere. The MAC-v1 climatology did not include single-scattering albedo (or aerosol type). However, through a surface-specific application of AOD, we potentially uncover a relationship between anisotropy changes and surface-specific aerosol mixtures. Figure 4.1c and 4.1e show examples of explained anisotropy residuals.

3.3.2 Finding optimal subsets

Extracted geophysical parameters are applicable to the prediction of TOA SW anisotropy. Regression towards TOA SW anisotropy with Artificial Neural Networks (as in Domenech and Wehr, 2011; Loukachine and Loeb, 2004; Capderou and Viollier, 2006) requires - like most other regression methods - a careful selection of input parameters. Including useless parameters could add unwanted noise while ex-

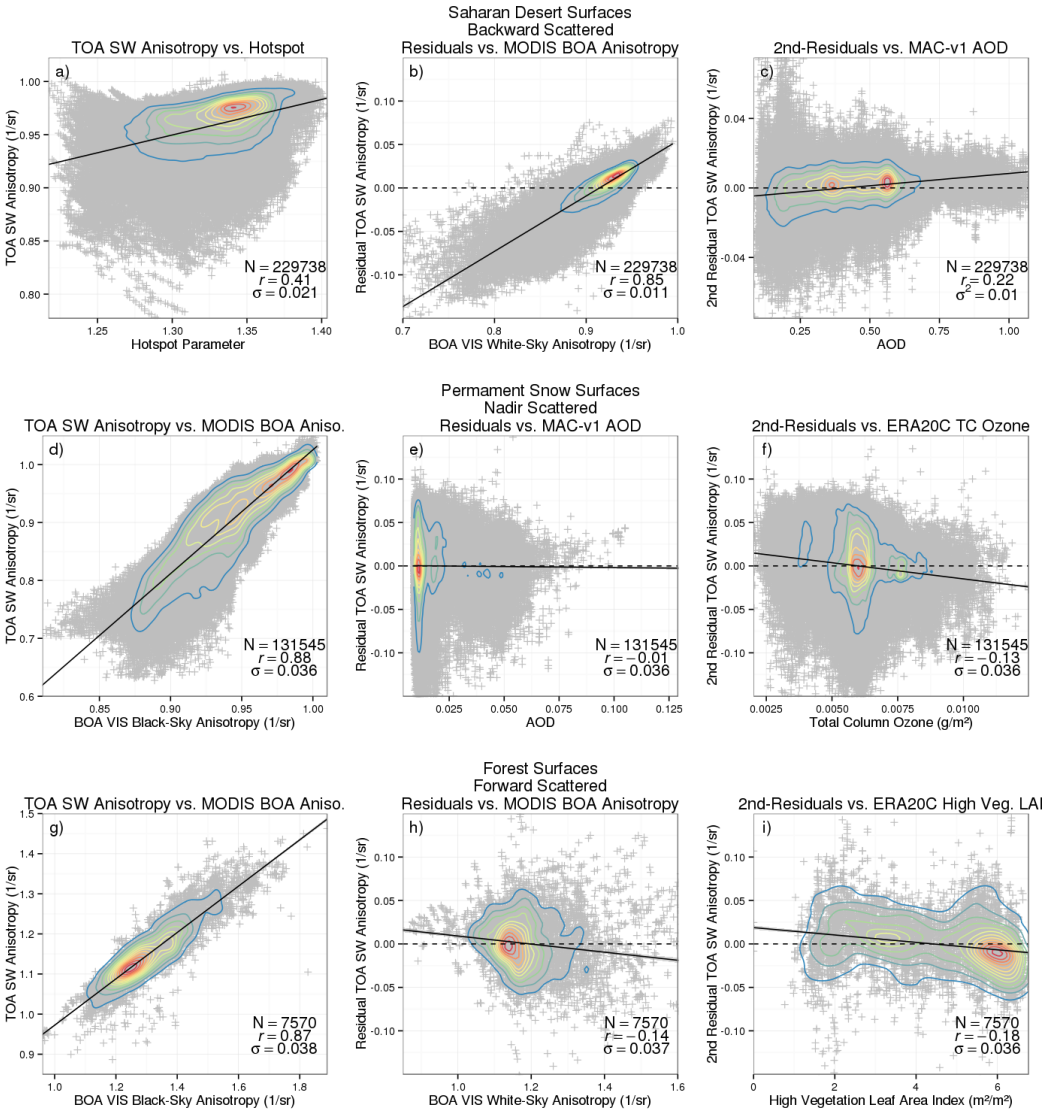

Fig. 3.1: We present the use of co-located geophysical parameters to explain varying TOA SW anisotropy for three surfaces at particular scattering directions (by row): Saharan Desert Surfaces at backward scattering; Permanent Snow and Ice Surfaces at nadir scattering; and Forest Surfaces at forward scattering. From left to right a simple linear models evolves. A linear fit with an initial parameter (a), d), and g)) leaves residuals which we aim to explain through an extended linear model using an additional parameter (b), e), and h)) which still leaves residuals. A third parameter (c), f), and i)) extends this linear model further. Colored lines mark the observed probability density (blue to red from low to high). Black lines show simple linear fits.

cluding useful parameters may reduce performance (i.e. the bias-variance dilemma; Theodoridis and Koutroumbas, 2009).

In order to identify which geophysical parameters are useful to each surface type and scattering direction (nadir: $\theta_V \sim 0°$; off-nadir forward: $\theta_V \sim 55°$, and $\varphi < 90°$ or $\varphi > 270°$; off-nadir backward: $\theta_V \sim 55°$, $90° \leq \varphi \leq 270°$), we applied two variable importance techniques: Random Forest regression and subsequent permutation test and Genetic Algorithms applied to Linear Regression (see section 4.2.3). Table 4.3 summarizes the selection of both methods.

Parameters relating to a scene's brightness (normalized radiance) as well as general illumination and viewing geometry (θ_S, φ, and θ_V) were consistently selected with the exception of fresh snow cases. As for general bidirectional reflectance distribution effects, the hotspot parameter was consistently selected over land surfaces free of fresh snow, while sun-glint reflectance was consistently selected only over open water surfaces as well as sea ice. Selection through Genetic Algorithms tended to include both hotspot parameter and sun-glint reflectance over almost all surface types and scattering directions, while selection through Random Forests usually included either hotspot parameter or sun-glint reflectance.

Tab. 3.3: Results of parameter selections applied to each surface type and BBR-perceivable scattering direction (B - backward, F - forward, N - nadir). Dots and their color connote selection method: selected by both Random Forest and Genetic Algorithms (black); excluded by both (blank); selected only by Random Forest (green); and selected only by Genetic Algorithms (orange). "/" indicates general exclusion from parameter selection.

	Surface Types									
	Forest	Fresh Snow	Sea Ice	Savannah	Grassland	Shrubland	Perm. Snow	Desert	Open Water	
Parameter//Scattering Dir.	B F N	B F N	B F N	B F N	B F N	B F N	B F N	B F N	B F N	
Normalized Radiance	● ● ●	● ●	● ● ●	● ● ●	● ● ●	● ● ●	● ● ●	● ● ●	● ● ●	
SZA	● ● ●	● ●	● ● ●	● ● ●	● ● ●	● ● ●	● ● ●	● ● ●	● ● ●	
VZA	● ●	● ●	● ●	● ●	● ●	● ● ●	● ●	● ●	● ●	
RAA	● ● /	● /	● ● /	● ● /	● ● /	● ● /	● ● /	● ● /	● ● /	
P(SGA)	● ●		● ● ●	● ●	● ●	● ●	● ● ●	● ●	● ● ●	
Hotspot	● ● ●	● ● ●	● ● ●	● ● ●	● ● ●	● ● ●	● ● ●	● ● ●	● ● ●	
AeroCom Median AOD	● ●	●	● ● ●	● ● ●	● ● ●	● ● ●	● ● ●	● ● ●	● ● ●	
ERA Ozone	● ● ●	●	● ● ●	● ● ●	● ●	● ●	● ● ●	●	● ● ●	
ERA TCWV	● ● ●		● ● ●	● ● ●	● ● ●	●	● ● ●	● ● ●	● ●	
α_{surf} Black-sky VIS	● ● ●	● ● ●	/ / /	● ● ●	● ● ●	● ● ●	● ● ●	● ● ●	/ / /	
α_{surf} White-sky VIS	● ● ●	● ●	/ / /	● ● ●	● ● ●	● ● ●	● ● ●	● ● ●	/ / /	
α_{surf} Black-sky NIR	● ● ●	● ●	/ / /	● ● ●	● ● ●	● ● ●	● ● ●	● ● ●	/ / /	
α_{surf} White-sky NIR	● ● ●	● ● ●	/ / /	● ●	● ● ●	● ● ●	● ● ●	● ● ●	/ / /	
ERA LAI low veg.	●		/ / /	● ● ●	● ● ●	● ● ●	/ / /	● ●	/ / /	
ERA LAI high veg.	● ●	● ● ●	/ / /	● ●		● ●	/ / /	●	/ / /	
ERA 10m wind	●		● ● ●	● ●	● ●	● ●	● ● ●		● ● ●	
ERA surface roughn.	● ●	● ●		● ● ●	● ●	● ●	●			
ERA charnock										
ERA snow depth	/ / /	●	/ / /	/ / /	/ / /	/ / /	●	/ / /	/ / /	
ERA ice cover	/ / /	/ / /		/ / /	/ / /	/ / /	/ / /	/ / /	/ / /	

Climatological AOD - potentially explaining atmospheric scattering - appears consistently relevant over most surface types with the exception of fresh snow, sea ice, and nadir directed scattering over forest, savannah, grassland, and open water. Gaseous absorption through atmospheric water vapor or ozone was sparsely selected by both methods with no relevance over fresh snow surfaces. For permanent snow and sea ice cases, on the other hand, both methods reported importance for at least two out of three scattering directions.

MCD43GB-based land surface anisotropy - which captures local and climatological bi-directional reflection effects perceived from a satellite perspective and is available in VIS and NIR as well as under white-sky and black-sky conditions - was frequently selected by both methods. For fresh snow cases we found less agreement or even mutual exclusion (at forward-scattering). Parameters from ERA-20C - which characterize the land surface state beyond climatological surface anisotropy - were collectively excluded for many surface types. For at least two out of three scattering directions, we found consistent relevance for high vegetation LAI over forest, surface roughness and low vegetation LAI over savannah, and 10m wind over permanent snow cases.

We believe that potential changes in land surface appearance mostly followed a regular annual cycle and were therefore generally covered by above land surface anisotropy. Reasons for the apparent importance of ERA-20C parameters could be rooted in non-climatological surface conditions: e.g. irregular vegetation on/offsets over forest and savannah regions as well as wind-driven formation of unusual "Sastrugi" over permanent snow (e.g. Corbett and Su, 2015). Alternatively, LAI (of low or high vegetation) was potentially selected due to its correlation to NDVI, which served to estimate CERES ADMs (see Section 4.2.1).

Apart from fresh snow cases, we found a general agreement of both methods on inclusion or exclusion of parameters. We interpret that a layer of fresh snow alienates the surface anisotropy sufficiently to render the MOD43GF product useless. Interestingly, Genetic Algorithms selected High Vegetation LAI as important. We suspect that snow-covered forests might appear different enough in anisotropy compared to plain snow fields, leading to the selection of this parameter.

The application of different input sets, as described in Table 4.4, to artificial neural networks (Section 3.2.4) affected the ability to predict TOA SW fluxes on unseen test data (shown in Table 4.4). Compared to CERES flux estimates, we generally found poorest performance for the minimum input set (set d)), on average 0.52 - 1.08 W m^{-2} worse than the best performer. Using the complete parameter set (set c)) slightly surpassed optimal parameter sets (sets a) and b)) for particular surfaces like sea ice cases (by up to 0.47 W m^{-2}) and forward and nadir-scattered light over

savannah cases (by up to 1.39 W m^{-2}). However, we found optimal sets to exceed the performance of the complete parameter set in other cases (like nadir-scattering over permanent snow and desert by a difference of 0.8 W m^{-2} and 1.97 W m^{-2}, respectively). Summarized over all surfaces, we found little performance difference between optimal sets (on average 0.00 - 0.07 W m^{-2}). From then on we used set a) as final ANN input.

Tab. 3.4: The test error of four different sets of ANN input: a) obtained from Random Forest Regression, b) obtained from Genetic Algorithms applied to a Linear Model, c) all available parameters and d) only viewing and illumination geometric parameters (θ_S, φ, θ_V, and normalized radiance). For each BBR viewing direction and surface type we bolded the best performing set (test error in W m^{-2}, and in % in parentheses below)) and show additional performance downgrade of all other sets.

		Surface Types									
BBR view	ANN Input Set	Forest	Fresh Snow	Sea Ice	Savannah	Grassland	Shrubland	Perm. Snow	Desert	Open Water	All surfaces
Backward	a) Random Forest Regr.	**6.51**	+0.94	+0.09	**2.26**	**2.83**	+0.02	+0.04	**2.98**	**1.28**	+0.07
		(3.14%)	(+0.35%)	(+0.03%)	**(1.40%)**	**(1.56%)**	(-0.06%)	(-0.06%)	**(1.07%)**	**(1.66%)**	(+0.00%)
	b) Genetic Algorithms	+0.09	**9.12**	+0.47	+0.12	+0.22	+0.03	**2.05**	**2.98**	+0.02	**2.69**
		(+0.07%)	**(3.67%)**	(+0.15%)	(0.24%)	(+0.06%)	(+0.02%)	**(0.86%)**	**(1.07%)**	(+0.00%)	**(1.40%)**
	c) All Parameters	+0.03	+0.69	**2.69**	+0.06	+0.43	**2.51**	+0.14	+0.14	+0.03	+0.11
		(-0.01%)	(+0.12%)	**(1.15%)**	(+0.09%)	(+0.13%)	**(1.37%)**	(+0.04%)	(+0.08%)	(+0.05%)	(+0.04%)
	d) Minimum	+0.33	+1.04	+0.45	+0.69	+1.08	+1.68	+1.20	+1.98	+0.13	+1.08
		(0.33%)	(+0.31%)	(+0.24%)	(+0.33%)	(+0.60%)	(+0.67%)	(+0.36%)	(+0.68%)	(+0.15%)	(+0.34%)
Forward	a) Random Forest Regr.	+2.18	+2.37	+0.08	+0.11	+0.00	**2.51**	**2.81**	+0.05	+0.56	+0.25
		(+1.67%)	(+0.16%)	(+0.07%)	(-0.05%)	(+0.02%)	**(1.46%)**	**(1.06%)**	(+0.01%)	(+0.57%)	(+0.25%)
	b) Genetic Algorithms	**2.96**	+0.06	+0.25	+0.04	**3.10**	+0.02	+0.78	**2.64**	+0.36	+0.25
		(2.67%)	(+0.00%)	(+0.31%)	(-0.11%)	**(1.63%)**	(-0.04%)	(+0.31%)	**(0.94%)**	(+0.48%)	(+0.25%)
	c) All Parameters	+0.17	+0.50	**3.60**	**2.36**	+0.20	+0.12	+0.29	+0.01	**3.23**	**3.20**
		(+0.41%)	(-0.50%)	**(1.16%)**	**(1.46%)**	(+0.22%)	(+0.40%)	(+0.18%)	(+0.00%)	**(3.62%)**	**(2.24%)**
	d) Minimum	+0.40	**5.97**	+0.76	+0.41	+0.76	+0.73	+2.22	+1.04	+1.80	+1.44
		(+0.31%)	**(3.74%)**	(+0.46%)	(+0.11%)	(+0.36%)	(+0.23%)	(+0.78%)	(+0.35%)	(+1.77%)	(+0.96%)
Nadir	a) Random Forest Regr.	+0.75	+0.22	+0.24	+1.39	+0.18	**5.48**	**1.53**	**3.92**	**3.34**	**3.98**
		(+0.67%)	(-0.06%)	(+0.06%)	(+0.64%)	(-0.03%)	**(2.75%)**	**(0.54%)**	**(1.38%)**	**(3.98%)**	**(2.89%)**
	b) Genetic Algorithms	**5.55**	+0.62	+0.19	+0.06	+0.02	+0.17	+0.26	+0.03	+0.11	+0.06
		(3.93%)	(+0.08%)	(+0.05%)	(+0.11%)	(-0.12%)	(+0.05%)	(+0.12%)	(+0.01%)	(-0.04%)	(-0.03%)
	c) All Parameters	+0.01	+0.28	**4.16**	**3.10**	**6.86**	+0.16	+0.80	+1.97	+0.33	+0.48
		(-0.02%)	(-0.09%)	**(1.55%)**	**(2.08%)**	**(3.84%)**	(+0.11%)	(+0.45%)	(+0.72%)	(-0.09%)	(+0.01%)
	d) Minimum	+0.30	**9.98**	+0.51	+0.64	+0.64	+0.44	+1.01	+0.74	+0.73	+0.52
		(+0.29%)	**(4.52%)**	(+0.18%)	(+0.36%)	(+0.25%)	(+0.11%)	(+0.45%)	(+0.21%)	(+0.78%)	(+0.45%)

The large flux errors over fresh snow surfaces (up to 9.98 W m^{-2}) were due to large absolute values (a product of snow's high albedo in lower latitudes with correspondingly low θ_S) and the apparent lack of suitable candidates relating to TOA anisotropy (cf. Table 4.3). In effect, the minimum input (set d)) performed best in 2 out of 3 scattering directions.

Figure 4.2 shows a global map of deviations in ANN predictions from original CERES flux estimates. Regions in northern latitudes exceeding the mission requirement of 10 W m^{-2} could largely be attributed to fresh snow cases, while larger uncertainties near Antarctica were caused by sea ice. Empty areas (e.g. the southern ocean) were either persistently cloudy or footprints composed of multiple surfaces (see Section 3.3.3).

Figure 4.3 presents which angular combinations (θ_S and φ) caused ANN predictions to deviate from CERES estimates. We found that uncertainties increased near the boundaries of sampled angles (e.g. shrubland), at lower θ_S (e.g. fresh snow), and around pronounced anisotropy (such as the sun-glint region over open water). The angular space that will be observed by EarthCARE's BBR instrument (shown in gray shade, pers. comm. ESA) was only partly covered by CERES samples, the result of a difference in equator crossing time between EarthCARE (2:00pm) and Aqua (1:30pm) or Terra (10:30am). To test how well ANNs predicted anisotropies over unseen angular combinations, we manually excluded two regions ($15° \leq \varphi \leq 25°$ and $155° \leq \varphi \leq 165°$ at $0° \leq \theta_S \leq 80°$). Retrained ANNs using remaining samples were applied over excluded regions. Compared against a training using complete data, the increase in flux error was well below 1.5 W m^{-2} over most surface types. Only open water (an average increase in excluded regions of 3.6 W m^{-2} or 4.48%), grasslands (2.7 W m^{-2} or 1.56%), sea ice (2.5 W m^{-2} or 1.01%), fresh snow (2.1 W m^{-2} or 0.92%), and permanent snow (1.9 W/ m^{-2} or 0.71%) cases demonstrated a larger increase in excluded angular portions (shown in Figure 4.4). We attribute the large increase over open water to the partial exclusion of dominant sun-glint area. Interestingly, the performance of some (non-excluded) angular combinations (like open water $50° \leq \varphi \leq 70°$ and fresh snow $70° \leq \varphi \leq 120°$) profited from ANN training using a reduced training set. This suggests that further sub-division in angular space (beyond forward and backward scattering) allows for better performance.

3.3.3 Modifications for EarthCARE

In order to apply the above approach operationally, dynamic surface types (fresh snow and sea ice) need to be consistently assigned to CERES surface classes. We delineated sea ice from ice-free ocean using ERA-20C sea ice fraction (greater than zero). The best candidate to separate snow-free from fresh snow or permanent snow cases was ERA-20C snow depth (greater than zero or greater than 4.9 m,

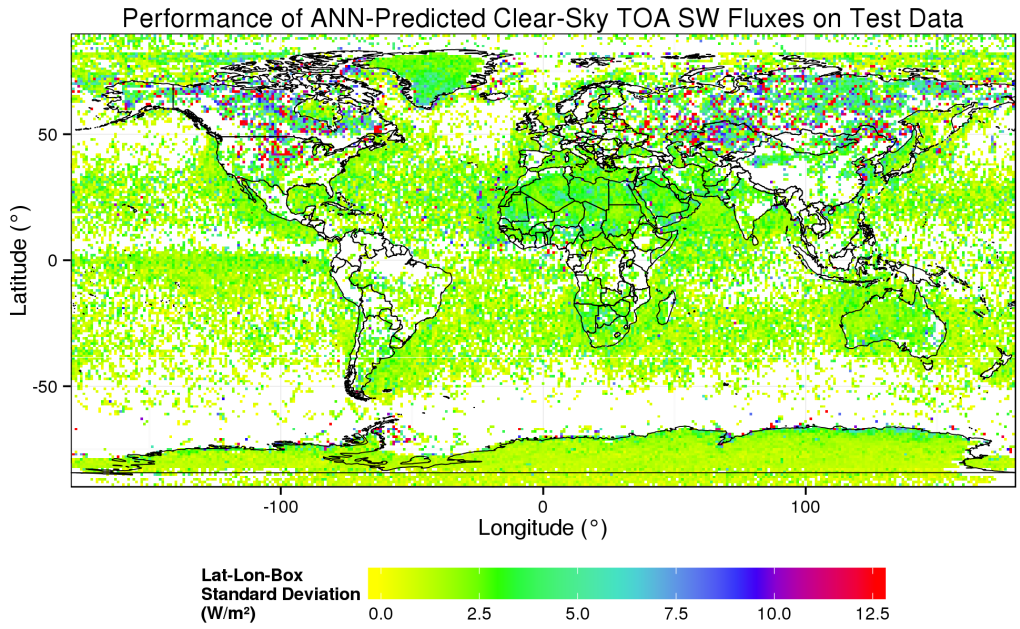

Fig. 3.2: We present Error Standard Deviations of ANN-predicted (using set a)) clear-sky TOA SW Fluxes of single-surface CERES footprints within $1^\circ \times 1^\circ$ Latitude-Longitude boxes. Individual footprints are either at nadir or 55° θ_V, aiming for a BBR-like viewing geometry.

respectively). Naturally, snow depth fails to report the area covered by snow and only indicates snow contamination in a footprint. Compared to CERES classes, we identified the partial presence of sea ice, fresh snow, and permanent snow with hit rates (and false alarm rates) of 97.1% (8.5%), 92.9% (42.1%), and 99.6% (0.5%), respectively. We suspect that large false alarm rates over fresh snow resulted from ERA-20C's coarse resolution (approximately 125 km grid spacing). During the EarthCARE mission ECMWF (European Centre for Medium-Range Weather Forecasts) forecasts (using IFS 41r2) will provide information instead of ERA-20C. Reported fields will have a finer spatial resolution (approximately 8 km grid spacing) and potentially produce higher hit (and lower false alarm) rates.

To further assure operational fitness, we verified that anisotropy predictions over mixed surfaces (roughly a third of all obtained CERES footprints) satisfied mission requirements. To predict a TOA SW anisotropy $\Re_{mix}$ over a footprint containing several surface types, we used the approach by Bertrand et al. (2005). $\Re_1$ and $\Re_2$ denote predicted anisotropies over each surface type, and f_1 and f_2 respective surface fraction.

$$\Re_{mix} = \frac{f_1 \Re_1 \bar{a}_1 + f_2 \Re_2 \bar{a}_2}{f_1 \bar{a}_1 + f_2 \bar{a}_2} \tag{3.15}$$

Required surface type albedos, $\bar{a}_1$ and $\bar{a}_2$, were approximated from single-surface footprints of similar latitude (categorized into tropical zone: 23.5° S- 23.5° N,

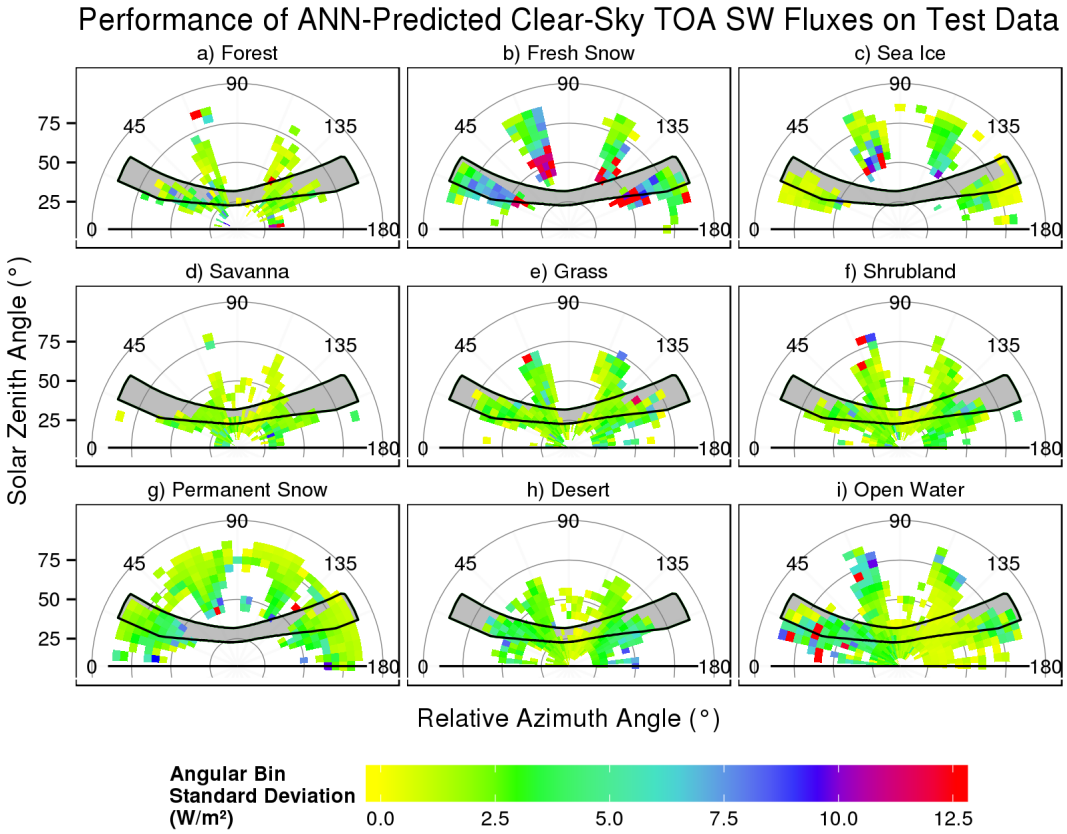

Fig. 3.3: Standard Deviations of ANN-predicted (using set a)) clear-sky TOA SW Fluxes of single-surface CERES footprints from original CERES SSF 4 estimates within 5° × 5° angular boxes of θ_S and φ. Individual footprints are at 55° θ_V, aiming for a BBR-like off-nadir viewing geometry. The gray-shaded area highlight expected angular combination seen by EarthCARE's BBR when sampling globally.

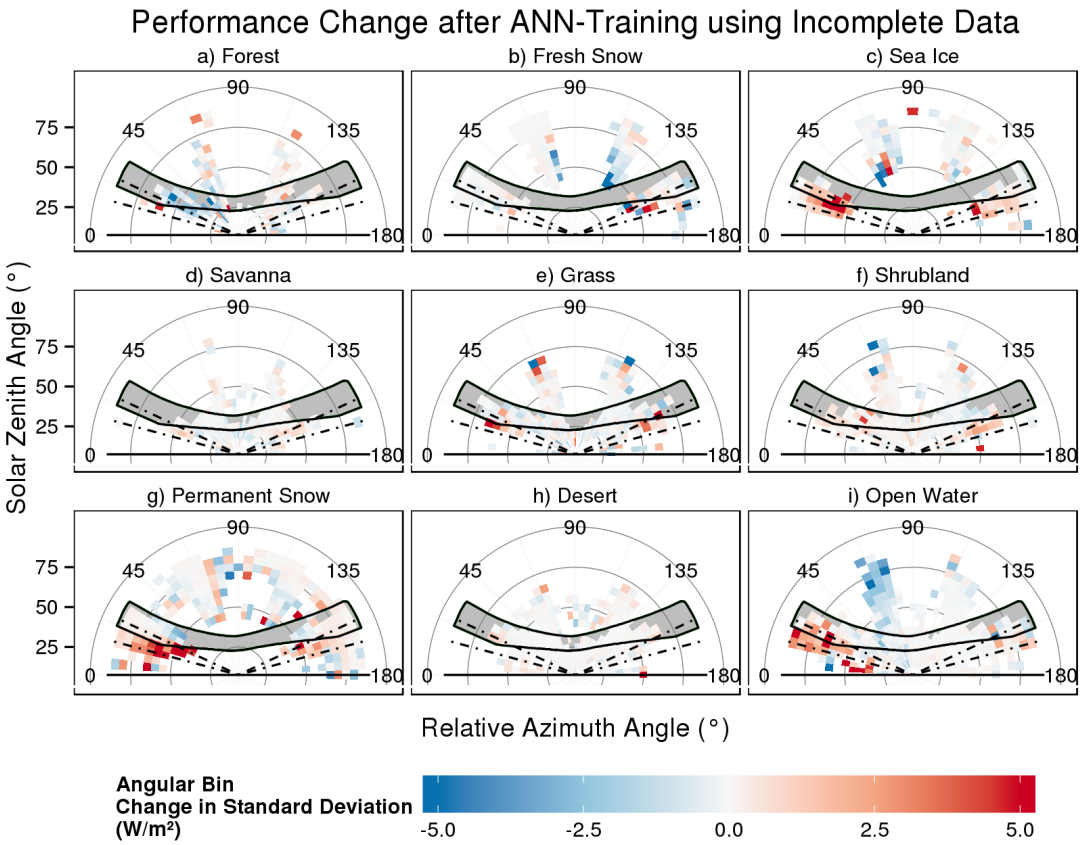

Fig. 3.4: Repeating the ANN training using an incomplete data set (excluding angular portions of $\varphi \in 15-25°$, $\varphi \in 155-165°$, and $\theta_S \in 0-80°$, highlighted by dashed lines), we present changes in Standard Deviations of ANN-predicted clear-sky TOA SW Fluxes compared against an ANN training using all available data (shown in Figure 4.3).

Tab. 3.5: Uncertainties (in W m^{-2}) resulting from the inclusion of mixed scenes in training and testing of fresh snow, sea ice, and permanent snow footprints. Sets a.) and d.) correspond to input sets shown in Table 4.4. Expected performances for all other surface types are listed in Table 4.4 (set a.))

	Surface Types		
	Fresh Snow	Sea Ice	Perm. Snow
ANN Input Set	set d.)	set d.)	set a.)
Fraction of mixed footprints	17.5%	74.2%	1.3%
Backward	11.64 (5.91%)	5.41 (2.51%)	2.75 (1.06%)
Forward	8.27 (6.33%)	9.63 (7.01%)	4.04 (1.55%)
Nadir	14.62 (8.83%)	8.06 (4.88%)	2.64 (1.14%)

mid-latitudes: 23.6° - 66.5° N/S, and polar regions 66.6° - 90° N/S) and solar zenith angle (by increments of 5° from 10° to 85° θ_S). We found that the above methodology worked reliably for snow- and ice-free mixtures: flux uncertainties were of similar magnitude (not shown) as single-surface footprints (Table 4.4). Only two combinations caused flux uncertainties larger than 10 W m^{-2}: grassland mixed with desert at nadir view with 17.84 W m^{-2} (2708 footprints or 0.07% of all nadir cases) and shrubland mixed with open water at nadir view with 26.04 W m^{-2} (14823 footprints or 0.37%). Assuming we had accurate information on snow fraction, mixtures including snow or ice produced large uncertainties across observed surface pairings (fresh snow: 16.1-194.1 W m^{-2}, permanent snow: 15.6-150.2 W m^{-2}, and sea ice: 15.2-59.1 W m^{-2}), particularly for combinations including stark albedo contrasts, like with open water.

Due to our inability to determine surface fractions of fresh or permanent snow and the large uncertainty above mixtures with snow or ice, we treated footprints with any snow or ice contamination as single-surface footprints of respective snow or ice type. We extended training as well as the test set, and repeated ANN training. For fresh snow and sea ice which contained a large fraction of mixed footprints (17.5% and 74.2% of snow and ice footprints were mixed, respectively) we discovered that a simpler input set (set d)) resulted in lower flux uncertainties compared to set a). Prediction over permanent snow (only 1.3% of permanent snow footprints were mixed) remained optimal using set a). Application of re-trained ANNs on extended test data resulted in higher flux uncertainties (Table 3.5) than a pure surface training

and testing (cf. Table 4.4), clearly the result of introduced heterogeneity of mixed surface footprints into ANN training and testing.

3.4 Discussion

The SW radiance-to-flux conversion over clear-sky scenes is challenging due the spatial heterogeneity and temporal variation of factors driving bidirectional reflectance distribution at TOA. The CERES solution for land surfaces involved separate ADMs per regional and temporal bin, and further separation through levels of surface specific parameters (such as NDVI, surface elevation variability, or fractional coverage through snow or ice). We have successfully shown that the use of additional parameters, relating to the geophysical state of surface and atmosphere as well as viewing and illumination geometry, could explain variations across bins, and thus help to dissolve binning. We presented the identification of optimal subsets and their use as input to ANNs, applied per surface type and scattering directions as perceived by EarthCARE's BBR. To ensure mission-worthy flux estimates we presented modifications concerning footprints partly covered in snow or ice.

We showed that ANNs performed better when optimal subsets of parameters were used instead of their full set. Even though we applied two very different selection methods for variable importance, we mostly found agreement on in- or exclusion of parameters. Both the selection of the hotspot parameter over land surfaces free of fresh snow and the selection of sun-glint reflectance over open water confirm our understanding of general bidirectional reflectance effects established at Earth's surface. The additional and consistent selection of MCD43GF-based surface anisotropy confirms that local climatological surface conditions further impact such effects over all land types free of fresh snow. Apart from fresh snow scenes, AOD - even though extracted from a climatology - was frequently selected, we presume due to reoccurring spatial patterns like dust storms or biomass burning events which impact TOA SW anisotropy through scattering or absorption. Atmospheric gases (here total column water vapor and ozone) from ERA-20C, which could likewise impact TOA SW anisotropy through absorption, were only occasionally chosen. We found their selection foremost over sea ice and permanent snow surfaces, presumably because only these regions have a large enough variability in respective gas concentration. The identification of ERA-20C LAI of low and high vegetation over savannah and forest surfaces, respectively, could further support the importance of land surface anisotropy. On the other hand, their selection could simply be a response to CERES-based stratification by NDVI.

As with any alternative statistical tool, our methods for determining variable importance could potentially select meaningless variables. Noisy data, unrepresentative

validation sets (used to select one optimal set over the other), or a method's tendency to include more or fewer variables are all factors that make some variable selections controversial. We suspect that Genetic Algorithms had a tendency to include more parameters: the method persistently identified an importance of sun glint reflectance over land and the hotspot effect over water, both of which we find questionable. However, ANN training, while unable to eliminate useless parameters altogether, can reduce their weight to near zero. We can see in Table 4.4 that using the full parameter set was close to, and in some cases actually was, the best performing ANN input set.

The performance of ANNs indicates that we could successfully reproduce CERES models. ANN's overall relative errors - though covering only a portion of the viewing zenith angular space - were near the CERES-defined goal of 2.3% over ocean, 1.6% over land, and 2.0% over snow and ice (Su et al., 2015b).

TOA SW anisotropy over fresh snow remained largely unexplained. Future efforts should continue to explore sources characterizing anisotropy fluctuations reaching TOA. Radiative transfer simulations should also clarify the role of different aerosol types in altering TOA SW anisotropy aloft different types of surfaces.

Acknowledgements

We thank Nicolas Clerbaux, Howard W. Barker, Tobias Wehr, and all other members of the CLARA team for helpful discussion, Maximilian Voigt and Rene Preusker for technical support, and to the Atmospheric Sciences Data Center at the National Aeronautics and Space Administration, Langley Research Center, for providing them with the Clouds and the Earth's Radiant Energy System Single Scanning Footprint TOA/Surface Fluxes and Clouds data product. This work was possible through funding within the ESA contract 4000112019/14/NL/CT.

4

Top-of-atmosphere shortwave anisotropy over liquid clouds: sensitivity to clouds' microphysical structure and cloud-topped moisture

Abstract

We have investigated whether Top-of-Atmosphere Shortwave (TOA SW) anisotropy - essential to convert satellite-based instantaneous TOA SW radiance measurements into TOA SW fluxes - is sensitive to cloud-top effective radii and cloud-topped water vapor. Using several years of CERES SSF Edition 4 data - filtered for overcast, horizontally homogeneous, low-level and single-layer clouds of cloud optical thickness 10 - as well as broadband radiative transfer simulations, we built refined empirical Angular Distribution Models (ADMs). The ADMs showed that anisotropy fluctuated particularly around the cloud bow and cloud glory (up to 2.9-8.0%) for various effective radii and at highest and lowest viewing zenith angles under varying amounts of cloud-topped moisture (up to 1.3-6.4%). As a result, flux estimates from refined ADMs differed from CERES estimates by up to 20 W m^{-2} at particular combinations of viewing and illumination geometry. Applied to CERES cross-track observation of January and July 2007 - utilized to generate global radiation budget climatologies for benchmark comparisons with global climate models - we found that such differences between refined and CERES ADMs introduced large-scale biases of 1-2 W m^{-2} and on regional levels of up to 10 W m^{-2}. Such biases could be attributed in part to low cloud-top effective radii (about $8\,\mu$m) and low cloud-topped water vapor (1.7 kg m^{-2}) and in part to an inopportune correlation of viewing and illumination conditions with temporally varying effective radii and cloud-topped moisture, which failed to compensate towards vanishing flux bias. This work may help avoid sampling biases due to discrepancies between individual samples and the median cloud-top effective radii and cloud-top moisture conditions represented in current ADMs.

Tornow, F., Preusker, R., Domenech, C., Carbajal Henken, C. K., Testorp, S., Fischer, J., submitted to MDPI Atmosphere, June 2018

4.1 Introduction

Radiative fluxes – leaving the Earth-Atmosphere system through Top-of-Atmosphere (TOA) and inferred from satellite measurements – are a key variable in diagnosing the system's current energy balance and – when observed repeatedly – to assess the radiative effects of clouds and aerosols (e.g. Ramanathan et al., 1989). For stratocumulus clouds - predominantly found over cooler regions of mid-latitude oceans – the main effect is to reflect solar radiation (where a much darker ocean surface would otherwise absorb) while emission of terrestrial radiation to space is similar to cloud-free conditions (since low clouds emit at a near-surface temperature) (e.g. Wood, 2012). In the presence of aerosols, cloud liquid water may distribute over more numerous and smaller droplets which crucially alters cloud optical properties and ultimately affects solar reflection (Twomey, 1977).

To convert instantaneous TOA broadband radiance measurements into corresponding TOA fluxes, satellite missions (Viollier et al., 2009; Dewitte et al., 2008) have been relying on CERES ADMs (latest version "CERES SSF Edition 4" as described in Su et al., 2015a). The conversion for solar radiances to fluxes above clouds is – apart from viewing and illumination conditions – a function of cloud phase and cloud optical depth. The conversion factor, anisotropy, is resolved by viewing geometry (Relative Azimuth Angles ϕ and Viewing Zenith Angle θ_v) given a certain illumination geometry (Solar Zenith Angle θ_s). Anisotropy is mainly characterized by the cloud glory (the direct reflection back to the sun), the cloud bow (the direction of reflection at a scattering angle of about 140-145°), and higher intensity at larger θ_v in the forward-scattering direction. In theory, features of the scattering phase function, such as cloud bow and glory, should correspond to the size distribution of cloud droplets. This correlation is illustrated in Figure 4.1. Stratocumulus clouds and their cloud-aerosol interaction should distribute reflected solar radiation differently depending on their droplet size distribution (given a constant cloud optical depth). Additionally, low clouds can have vast amounts of water vapor aloft. Such absorbing gas (acting mainly beyond $0.8\,\mu$m) should have a stronger effect on upwelling radiances at larger θ_v than at smaller ones due to respective atmospheric path lengths. Accordingly, anisotropy should be dependent on levels of water vapor.

In this study, we hypothesize that TOA SW anisotropy changes significantly with cloud microphysical properties, represented through the cloud-top effective radius, and amount of moisture above clouds, represented through cloud-topped water vapor. Using several years of CERES SSF Edition 4 data, we extracted footprints of low-level and single-layer clouds above ocean which are overcast, horizontally homogeneous, and had mean cloud optical depth of about 10 (Section 4.2.1). As shown in Section 4.2.3, we built new empirical ADMs using CERES-measured SW

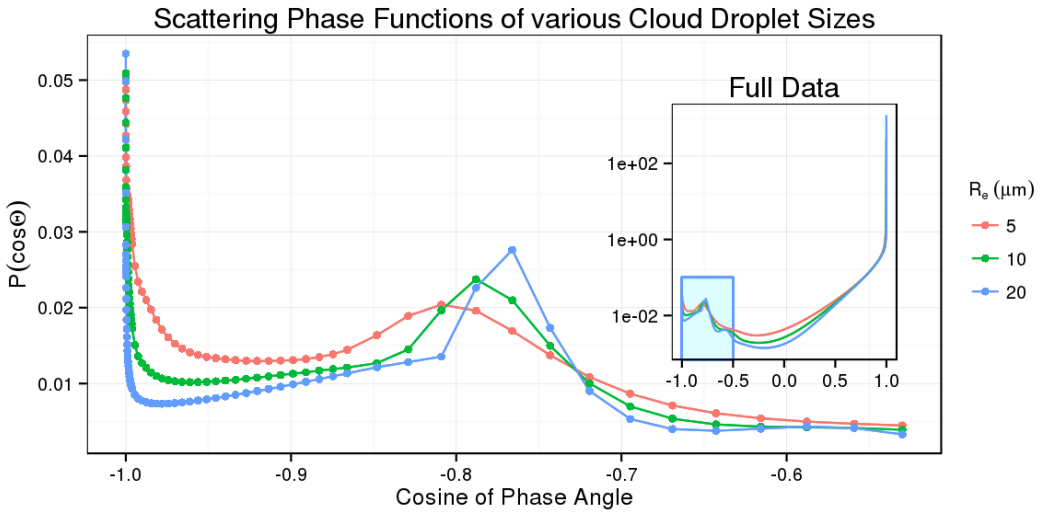

Fig. 4.1: Broadband phase functions for three different cloud droplet effective radii R_e. Phase functions were spectrally integrated over the solar regime (0.25-4.00 μm) and are based on Mie calculation in spectral subintervals, assuming a Gamma-Hansen distribution with an effective variance of 0.11. Contributions from each subinterval were weighted by corresponding spectral cloud extinction and solar constant. Note that the y-axis of the inset is logarithmic, while the main plot is shown in linear scale.

reflectances, MODIS-retrieved cloud-top effective radii, and estimates of cloud-topped water vapor (Section 4.2.2). In section 4.3 we demonstrate that refined ADMs had a sensitivity to above effective radii and water vapor, and that missing such sensitivity resulted in regional and systematic underestimation of TOA SW fluxes. Section 4.4 finally discusses results.

4.2 Material and Methods

4.2.1 TOA SW Reflectances

CERES Edition 4 SSF

We obtained TOA SW reflectances (0.3-5.0 μm) from CERES SSF Edition 4 (Su et al., 2015a). Measurements were realized by CERES instruments (Wielicki et al., 1996) on board Aqua and Terra satellites and operating in two modes: the Rotating Azimuth Plane Scan (RAPS) mode (performed periodically during 2000-2005) and cross-track scan mode (of the year 2007). CERES footprints covered areas of about 20 km diameter at nadir. For θ_v of up to 69.5°, all footprints were collocated with MODIS imagery as well as products derived from the CERES/MODIS cloud algorithms (based on Minnis et al., 2011). Cloud information on MODIS pixel-basis

Tab. 4.1: A list of CERES footprints, obtained after screening for low-level and single-layer clouds, overcast conditions, a cloud optical depth of 10, and cases free of horizontal inhomogeneity: in total 2470099 footprints.

	No. of CERES footprints		
Year	Terra (FM1 & FM2)	Aqua (FM3 & FM4)	Mode
2000	192604	/	RAPS
2001	259810	/	RAPS
2002	278305	85745	RAPS
2003	266966	223979	RAPS
2004	274189	276981	RAPS
2005	4730	62213	RAPS
2006	/	/	/
2007	273343	271234	cross-track

was used for statistics across CERES footprints, taking into account the instrument's point spread function (Wielicki et al., 1996).

We screened footprints for conditions typical of marine stratocumulus by selecting mean cloud-top pressures between 700 and 1000 hPa of single-layer clouds, a mean logarithmic cloud optical thickness $\tilde{\tau} = \exp\left(\overline{\log \tau}\right)$ of 10 (permitting values between 9.75 and 10.25) as well as ocean surface fractions greater 95%. We also screened overcast conditions (selecting cloud fraction $f \geq 99\%$), and cases free of horizontal inhomogeneity (Barker et al., 1996; Kato et al., 2005) by using footprints of $\nu > 10$, where $\nu = \overline{\tau}^2/\sigma(\tau)^2$; where $\overline{\tau}$ is the mean optical thickness and $\sigma(\tau)$ is the standard deviation of mean cloud optical thickness. Table 4.1 summarizes extracted footprints after screening.

Broadband Radiative Transfer Simulations

To supplement observations, we simulated TOA SW reflectances using the radiative transfer code MOMO (Matrix-Operator Model; Hollstein and Fischer, 2012). Simulations covered the solar spectrum between 0.25 and $4.00\,\mu$m through 53 spectral subintervals, chosen such that water spectral refractive indices changed near-linearly with wavelength. For each subinterval, non-correlated k-binning (Doppler et al., 2014) produced – based on HITRAN-2008 database (Rothman et al., 2009) - between $\mathcal{O}(10^1 - 10^3)$ k-terms to represent gaseous absorption. We chose about 80 vertical layers between 0 and 120 km, vertically resolving the lowest 2 km of atmosphere at 25-100 m (except for cloud-top and cloud-topped inversion, resolved at 5 m), 2-5 km altitude at 500 m, and 5-20 km at 2.5 km intervals. The choice of 70 Fourier terms allowed for an azimuthal resolution of 6°. θ_s (and likewise θ_v) were resolved at 35 angles, most of them listed in the first column of Table 4.2. We

used an isotropic ocean surface and Mie-calculated phase functions to represent scattering and absorption by clouds droplets in each vertical layer, and assumed a Gamma-Hansen droplet size distribution.

To cover realistic ranges of cloud-topped water vapor in simulations, we extracted four representative temperature and moisture profiles from radiosonde observations (Figure 4.2), covering between 3.2-20.1 kg m^{-2} of cloud-topped water vapor. To explore potential scenarios of cloud vertical profiles which resemble stratocumulus clouds of optical thickness 10 and were subject to weaker or stronger cloud-aerosol interaction, we used the adiabatic theory (e.g. Brenguier et al., 2000). Adiabatic clouds increase linearly in liquid water content (LWC) from cloud base to top and have a vertically constant cloud droplet number concentration. Sub-adiabatic conditions (i.e. an adiabaticity of < 1) capture the intrusion of dry air from aloft and this reduces the linear slope of LWC accordingly. Figure 4.3 shows the resulting 13 scenarios of adiabatic clouds, assuming an adiabaticity of 0.6. All cloud scenarios had a cloud top-pressure of 875 hPa.

4.2.2 Cloud-topped Water Vapor

To approximate the vertical column of water vapor located aloft marine low-level clouds, we used the following variables: precipitable water PW, surface skin temperature T_S and surface pressure P_S – all provided by the Goddard Earth Observing System (GEOS Bloom et al., 2005) version 5.4.1 and collocated to CERES footprints - as well as MODIS mean cloud top and cloud base pressure (P_{CT} and P_{CB}, respectively). All fields were included in CERES Edition 4 SSF (introduced in Section 4.2.1).

First, we approximated the amount of water in the cloud-topped boundary layer. Taking the T_S and the dry-adiabatic lapse rate, we derived the temperature at cloud base level T_{CB}. Applying the relation by Bolton (1980) (shown in Equation 4.1), we determined the saturation vapor pressure e_s at cloud base temperature (here T_{CB} in °C) and then (in Equation 4.2) the mixing ratio r. W_w and W_{air} are molecular weights of water and dry air, respectively.

$$e_s = 6.112 \exp\left(\frac{17.67\, T_{CB}}{T_{CB} + 243.5}\right) \tag{4.1}$$

$$r = \frac{e_s}{P_{CB}} \frac{W_w}{W_{\text{air}}} 10^{-3} \tag{4.2}$$

Assuming well-mixed conditions and thus a constant r within the cloud-topped boundary layer, we integrated the vertical column of water vapor between surface

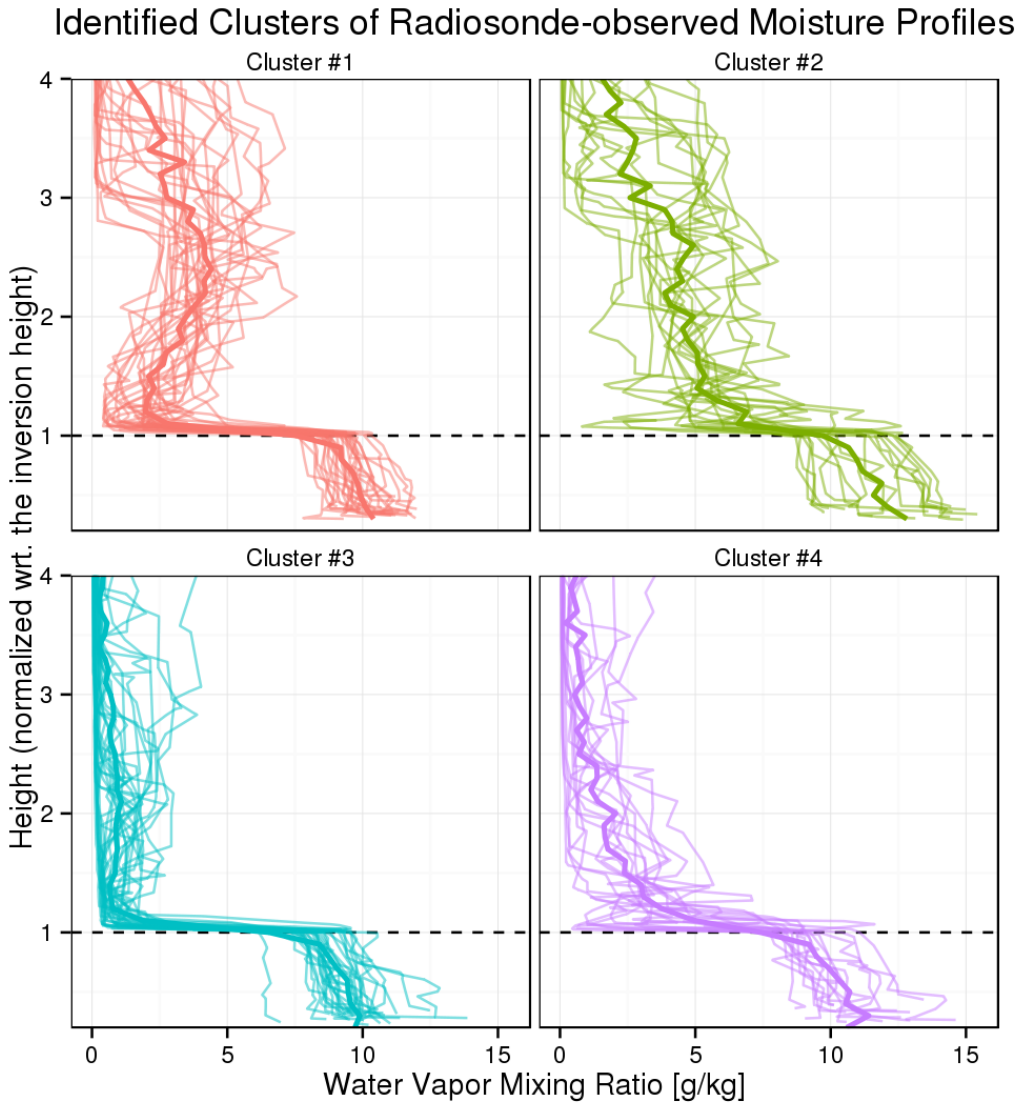

Fig. 4.2: Four main clusters of vertical moisture profiles as observed during cloudy days (ascertained through MODIS imagery) over 12 months (August 2016 to July 2017) of radiosonde observations on St. Helena (`http://catalogue.ceda.ac.uk/uuid/c6fccd62a8ad4d9ea35fb825c3968910`). Clusters were obtained through k-means clustering using mixing ratios at three different heights (normalized with respect to the cloud-top): 1.2, 1.4-1.6, and 2.3-2.7. Cloud-top levels were inferred from highest observed vertical level (within the lowest 2.5 km) with a relative humidity larger than 85%. For simulations we used temperature and moisture profiles of the nearest neighbor to each cluster center.

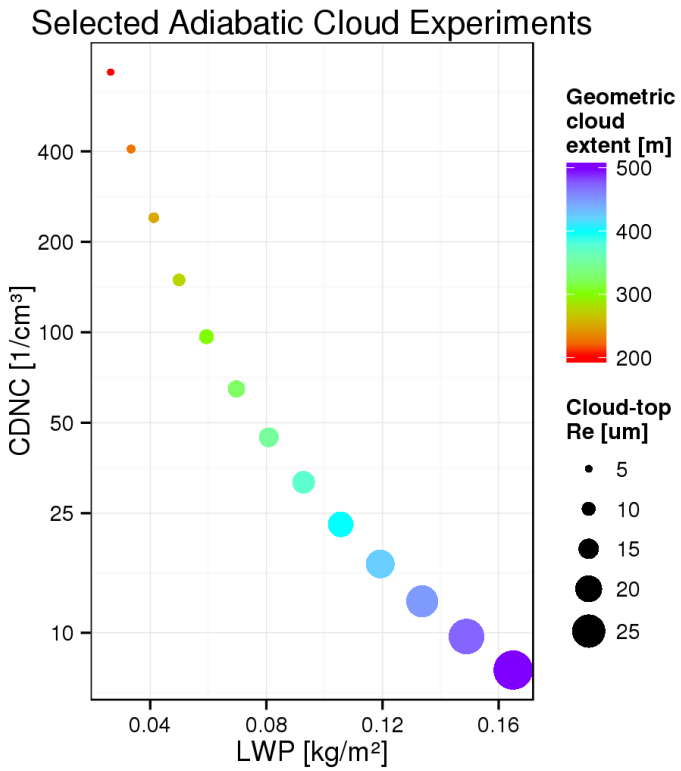

Fig. 4.3: The setup of thirteen adiabatic cloud experiments. Each experiment arrived at a cloud optical depth of 10 and a cloud top pressure of 875 hPa. Across experiments, both liquid water path (x-axis) and cloud-droplet number concentration (CDNC; y-axis) varied. Accordingly, geometric extent (shown in color) and profiles of cloud droplet effective radii (represented by cloud-top effective radius shown in dot size) changed.

and cloud-top. Finally, we subtracted the boundary layer integral from PW to gain the vertical column of cloud-topped water vapor $CTWV$ (as shown in Equation 4.3 where g is the gravitational constant and ρ_w is the water density).

$$CTWV = PW - \frac{1}{g\rho_w} \int_{P_S}^{P_{CT}} r \; dp \tag{4.3}$$

With regard to Figure 4.2, boundary layers rarely had a vertically constant mixing ratio. By using the ratio at cloud base, we potentially compensated an underestimation in the cloud-free boundary layer with an overestimation between cloud base and cloud top. Our methodology, additionally, depended on a correct vertical position of the cloud. In case of under- or overestimation of cloud base and top, the effect on errors in cloud-topped water vapor should, however, be regularizing.: e.g. an overestimation in cloud base and top height would result in lower boundary layer mixing ratios (as the cloud base temperature was erroneously lower) which would be integrated over a higher boundary layer. We mimicked a cloud base and top underestimation of 50 hPa and found a median offset of -0.5 kg m^{-2} (-7.6%) in cloud-topped moisture. Negative values in cloud-topped water vapor (found in 13% of all footprints) were set to zero.

4.2.3 Angular Distribution Models

The general strategy to estimate instantaneous fluxes F from observed radiances I_0 is to empirically learn – per scene type and per illumination geometry θ_s - the directional intensity of upwelling radiances with respect to the prevalent upwelling flux. Therefore, the upward hemisphere (resolved by θ_v and ϕ) is discretized. Observations are sorted into angular bins. Once all bins of the upward hemisphere are filled, fluxes ($\hat{F}$) are estimated through the hemispheric integral of mean radiances $\hat{I}$ from each bin. The last step is to infer on anisotropy R (Equation 4.4).

$$R(\theta_s, \theta_v, \phi) = \frac{\pi \hat{I}(\theta_s, \theta_v, \phi)}{F(\hat{\theta_s})} = \frac{\pi \hat{I}(\theta_s, \theta_v, \phi)}{\int_0^{2\pi} \int_0^{\pi/2} \hat{I}(\theta_s, \theta_v, \phi) d\theta_v d\phi} \tag{4.4}$$

A new radiance observation I_o can be converted into an instantaneous flux F, as shown in equation 4.5.

$$F(\theta_s) = \frac{\pi I_o(\theta_s, \theta_v, \phi)}{R(\theta_s, \theta_v, \phi)} \tag{4.5}$$

In CERES SSF Edition 4, liquid clouds over ocean were treated as a single scene type. To consider stark intensity changes of upwelling radiances with cloud fraction and cloud optical depth, collected radiances of each angular bin (resolved by 2° in θ_v

and ϕ) served to produce a sigmoidal fit linking $\hat{I}$ and $\ln(f\tilde{\tau})$. ADMs were therefore based on hemispheric integrals of sigmoidal fits. In effect, resulting anisotropies are a function of $\ln(f\tilde{\tau})$. In this study $f \approx 100\%$ and $\tilde{\tau} \approx 10$. Essentially, CERES TOA SW anisotropy – per angular bin and per discrete illumination geometry (resolved at 2°) – remained constant.

We produced new ADMs (hereafter referred to as "refined ADMs") by incorporating intensity changes of upwelling instantaneous reflectance ρ_o with cloud-top effective radius R_e and cloud-topped moisture $CTWV$. We produced a linear model per angular bin and discrete illumination geometry of the following form (with least-square estimates a, b, and c):

$$\ln \rho_o(\theta_s, \theta_v, \phi) = a + b \cdot \ln R_e + c \cdot CTWV \tag{4.6}$$

An example is shown in Figure 4.4. Similar to the CERES approach, we integrated TOA albedos as a function of linear models and inferred on TOA SW anisotropies. We produced a look-up table by applying linear models to R_e between 5 and $25\,\mu$m (by steps of $1\,\mu$m) as well as $CTWV$ between 0 and 40 kg m^{-2} (by increments of 2 kg m^{-2}).

In case of insufficient CERES observations within a bin (less than 10 or samples with a spread in R_e of smaller than $10\,\mu$m), we added reflectances from broadband radiative transfer simulations (introduced in Section 4.2.1) to complement CERES observations. This was generally necessary for θ_v beyond 70° and occasionally for some bins at particularly low or high θ_s (as listed in Table 4.2).

4.3 Results

Empirical ADMs allow us to estimate instantaneous TOA fluxes from satellite broadband radiometry. State-of-the-art shortwave ADMs (Su et al., 2015a, referred to as "CERES SSF 4" ADMs) over cloudy scenes are sensitive to cloud fraction f, cloud optical depth $\tilde{\tau}$, and cloud phase. In this study, we examined whether ADMs should also be sensitive to the cloud micro-physical structure and amount of absorbing atmospheric gas above the cloud layer.

We generated alternative ADMs (referred to as "refined ADMs", Section 4.2.3), using CERES SSF 4 data (Section 4.2.1, years 2000-2005), including CERES-observed TOA SW reflectances as well as collocated MODIS-retrieved cloud-top effective radius and estimated cloud-topped water vapor (Section 4.2.2). As shown in Section 4.2.1, we restricted ourselves to fully overcast, horizontally homogeneous, low-level, and

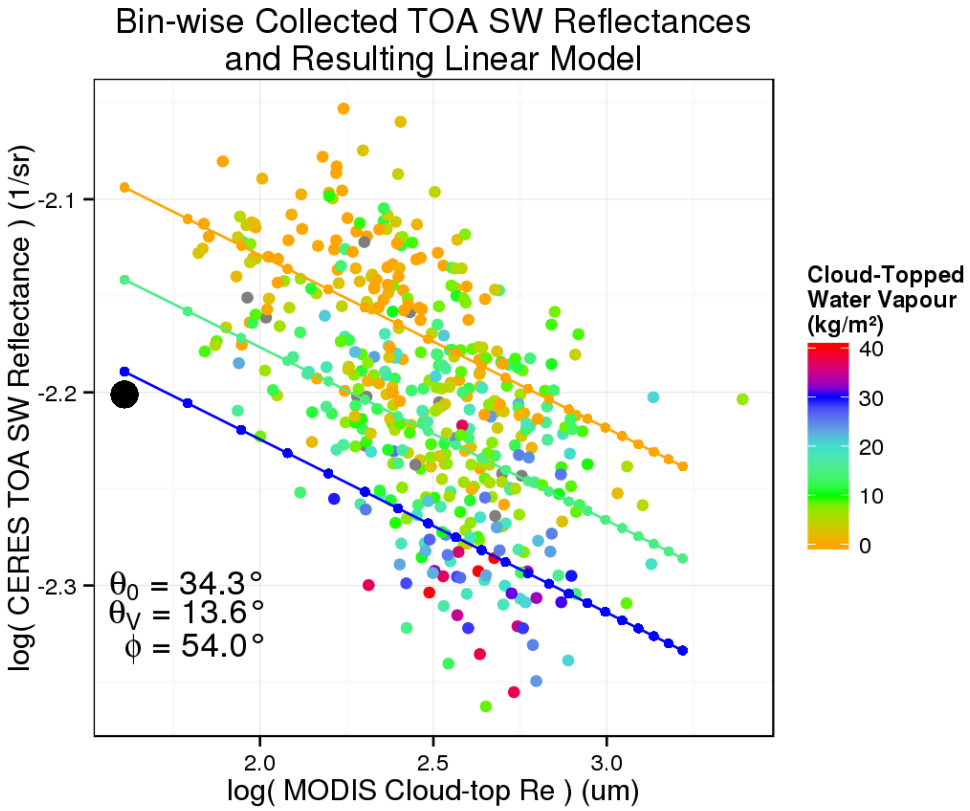

Fig. 4.4: For an exemplary angular bin (as specified in bottom left), we show collected CERES-measured TOA SW reflectances (y-axis) against cloud-top effective radii (x-axis; MODIS-retrieved mean value across each CERES footprint); both transformed through the natural logarithm. Colors explain the inferred amount of cloud-topped water vapor. Produced linear model (colored lines; Equation 4.6) - forming the basis for ADMs - captured the general darkening with larger droplet sizes (predicted for 5 to 25 μm) and with higher levels of cloud-topped moisture (predicted for 0, 15, and 30 kg m^{-2}). Following the CERES methodology, the average reflectance in this angular bin was represented by the black dot.

Tab. 4.2: A list summarizing the availability and nature of CERES footprints per increment of θ_s. To fill angular bins (resolved by ϕ and θ_v; here shown for θ_v between 0 and 70°) within the upward hemisphere, CERES footprints (numbers shown in second column) were in part supplemented by broadband simulations (fraction of bins receiving support shown in third column). Colleted CERES samples varied considerably in cloud-top effective radius (column four; showing minimum to maximum of medians for each angular bin) and cloud-topped water vapour (column five; correspondingly).

			Min.–Max. in angular bin medians of	
θ_s (°)	CERES footprints	Bins supplemented with simulations (%)	Cloud-top R_e (um)	Cloud-topped WV (kg m^{-2})
16.2	16144	33.3	5.9–26.2	0.0–30.8
18.8	29636	14.4	6.8–17.6	0.0–27.2
21.4	42413	7.1	6.8–14.8	0.0–20.7
23.9	53459	2.6	7.7–14.0	0.0–16.7
26.5	70327	1.5	9.1–16.5	0.0–15.6
29.1	84465	1.0	9.1–15.3	0.0–16.3
31.7	92215	0.8	8.8–15.5	0.0–14.3
34.3	103819	0.6	8.6–13.3	0.0–13.3
36.9	110576	0.3	9.5–13.9	0.9–12.0
39.5	111249	0.3	9.3–14.1	0.4–12.7
42.1	113933	0.2	10.1–14.1	0.0–12.3
44.7	110230	0.2	10.4–14.1	0.2–8.6
47.3	108844	0.8	10.7–15.4	1.0–8.7
49.9	103208	0.2	10.9–15.1	0.0–9.2
52.4	97595	0.6	11.1–17.3	0.3–7.9
55.0	85986	0.8	9.5–16.1	0.0–8.9
57.6	75292	1.3	11.0–15.4	0.0–9.2
60.2	67078	1.0	10.7–16.5	0.0–7.8
62.8	58011	1.8	11.5–18.0	0.0–10.5
65.4	45071	2.4	7.9–17.5	0.0–10.3
68.0	55063	2.1	12.2–20.1	0.0–7.4
70.6	43824	2.6	10.0–19.6	0.0–7.7
73.2	37792	4.0	11.7–21.9	0.0–12.0
75.8	30961	6.7	8.9–19.7	0.0–18.0
78.3	22864	14.1	10.8–22.5	0.0–16.6
80.9	16282	25.5	9.2–22.5	0.0–16.6

single-level clouds of optical thickness 10 and added simulated reflectances to angular bins in case of insufficient observations.

Refined ADMs show a marked difference in anisotropy across several cloud-top effective radii (Fig. 4.5, top), predominantly around the cloud bow and cloud glory. A higher cloud glory intensity for smaller droplets and an outward shift (in scattering angle) of cloud bow intensity with larger droplet size is in line with Mie-calculated phase functions (Fig. 4.1). For an R_e of $10\,\mu$m, anisotropies from refined ADMs agreed well with those from CERES SSF 4. Samples collected for this study showed median R_e around $10\,\mu$m in most angular bins (9.1- $15.3\,\mu$m at $\theta_s \approx 29°$, Tab. 4.2). We believe that CERES ADM construction used samples of similar characteristics and therefore produced anisotropies reflecting median conditions. For higher levels of cloud-topped water vapor (Fig. 4.5, bottom), we observed an increase in anisotropy at lower viewing zenith angles and a decrease in anisotropy at higher θ_v. Table 4.3 summarizes the spread in anisotropy for various illumination geometries. Anisotropy variations due to effective radii (2.9-8.0%) were generally larger than variations due to cloud-topped moisture (1.3-6.4%). The uncertainty in anisotropy (based on reflectance residuals of linear models) was of similar order of magnitude (3.2-5.3%) for variations due to effective radii and variations due to cloud-topped moisture. By reproducing the CERES approach (exemplarily shown in Figure 4.4 as black dot) and extracting reflectance residuals, we approximated a corresponding CERES uncertainty. Compared to CERES ADMs, uncertainties of refined ADMs were smaller by a factor 1.2 – 1.7.

Refined and CERES ADMs should produce different flux estimates, especially for departures from median conditions (e.g. small and large droplet size distributions). In order to quantify flux deviations, we took mean reflectances of refined models for three R_e, three θ_s , and a fixed cloud-topped water vapor, and applied both refined and CERES SSF 4 ADMs. A radiance $\hat{I}$ was produced from a reflectance through $\hat{I} = \hat{\rho} S \cos\theta_s$, where S is the solar constant.

$$\Delta F(\theta_s) = \pi \cdot \hat{I}_{\text{refined}}(\theta_s, \theta_v, \phi, R_e, CTWV) \cdot \left(\frac{1}{R_{\text{refined}}(\theta_s, \theta_v, \phi, R_e, CTWV)} - \frac{1}{R_{\text{CERES}}(\theta_s, \theta_v, \phi)} \right) \tag{4.7}$$

Figure 4.6 shows flux deviations between ADMs (computed according to Equ. 4.7) of up to 20 W m^{-2}. For an R_e of 5 and $20\,\mu$m these deviations were located in the forward scattering direction (ϕ between 0-45°) and again in the direct backscatter (cloud bow and glory). For an R_e of $10\,\mu$m differences were mostly within 10 W m^{-2} and showed a general positive bias. We suspect that employed simulations (predominantly at θ_v of 70° and higher), which were free of horizontal heterogeneity

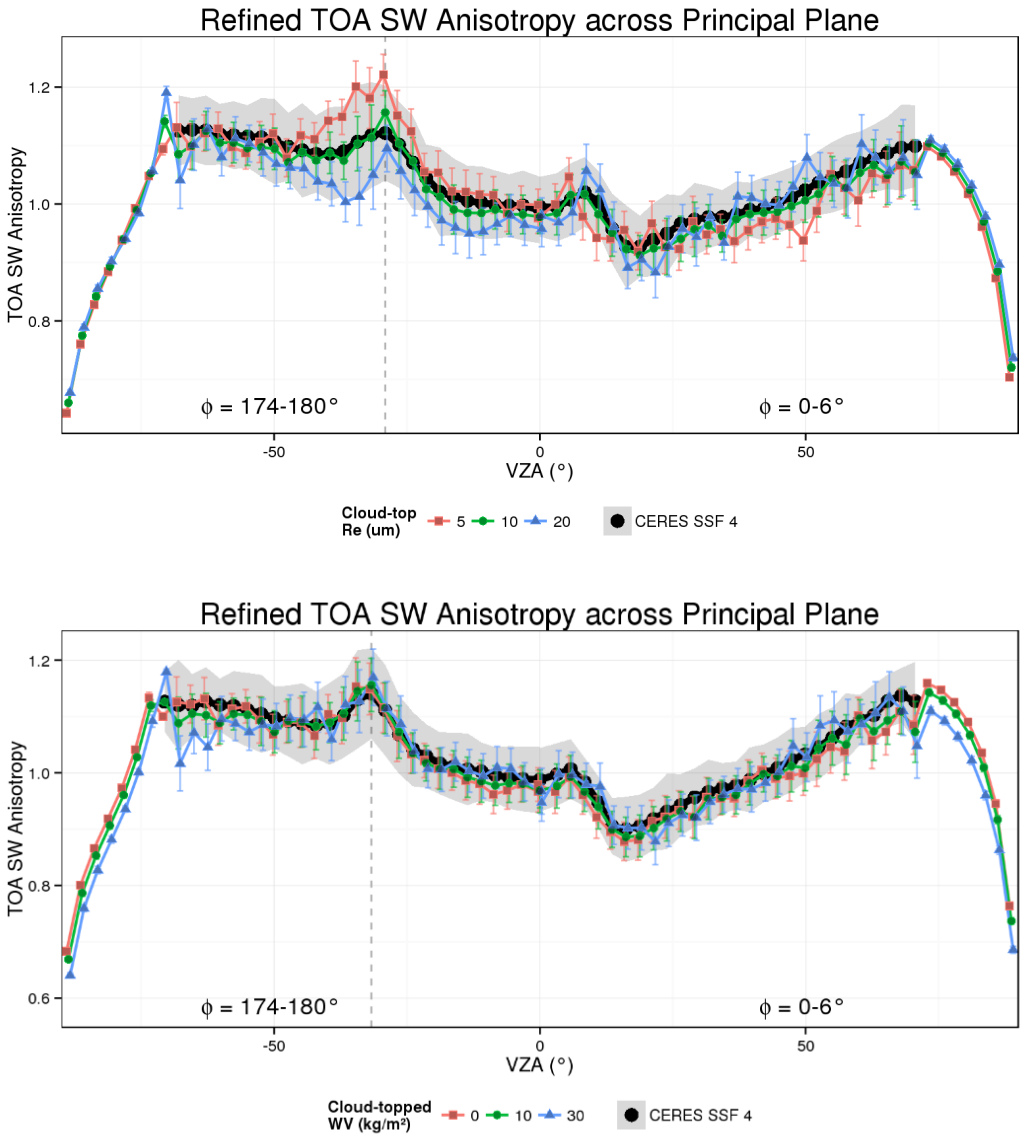

Fig. 4.5: TOA SW anisotropy of refined ADMs at varius cloud-top effective radii (top, at a θ_s of 29° and a steady cloud-topped water vapor of 4 kg m^{-2}) and levels of cloud-topped water vapor (bottom, at a θ_s of 32° and a steady cloud-top effective radius of $10\,\mu$m). Colors indicate respective scenarios. Black dots mark TOA SW anisotropy of CERES SSF 4. Error bars were based on reflectance residuals of linear models propagated into TOA albedo and TOA anisotropy. To obtain corresponding uncertainties for CERES (grey shade), we mimicked the CERES approach and obtained reflectance residuals. Grey dashed lines indicate the cloud glory position.

Tab. 4.3: A θ_s-resolved overview of the anisotropy spread due to extremes in cloud-top effective radius (second column displays the median absolute difference of anisotropy at $25\,\mu$m and anisotropy at $5\,\mu$m normalized by the anisotropy at $10\,\mu$m at a steady cloud-topped water vapor of 4kg m^{-2}) and cloud-top water vapor (third column displays the median absolute difference of anisotropy at 32 kg m^{-2} minus anisotropy at 0 kg m^{-2} normalized by the anisotropy at 16 kg m^{-2} at a steady cloud-top effective radius of $10\,\mu$m). We also show estimated anisotropy uncertainties of refined ADMs (fourth column), CERES SSF 4 ADMs (fifth column), and their ratio (column six). Uncertainties were produced as laid out in Figure 4.5 and in the text.

	Median Anisotropy Spread (%)		Median Anisotropy Uncertainties (%)		Median Ratio CERES/
θ_s (°)	Cloud-top R_e	Cloud-topped WV	Refined	CERES-like	Refined
16.2	3.9	2.0	3.2	6.0	1.7
18.8	3.9	1.9	3.7	5.9	1.5
21.4	3.5	1.6	4.0	6.1	1.5
23.9	3.2	1.5	4.0	6.0	1.5
26.5	2.9	1.3	4.0	5.7	1.4
29.1	2.9	1.3	4.1	5.7	1.4
31.7	3.1	1.3	4.2	5.7	1.4
34.3	3.2	1.3	4.3	5.6	1.3
36.9	3.3	1.5	4.4	5.5	1.2
39.5	3.3	1.3	4.5	5.3	1.2
42.1	3.3	1.5	4.5	5.3	1.2
44.7	2.9	1.5	4.4	5.4	1.2
47.3	3.6	1.6	4.2	5.3	1.2
49.9	3.7	1.5	4.0	5.2	1.3
52.4	3.2	1.7	4.0	5.2	1.3
55.0	3.8	1.8	3.9	5.2	1.3
57.6	4.5	2.0	3.7	5.1	1.4
60.2	4.7	1.9	3.6	5.0	1.4
62.8	5.0	2.1	3.4	4.9	1.4
65.4	5.6	2.7	3.4	4.9	1.4
68.0	5.4	2.6	3.4	4.8	1.4
70.6	6.2	2.9	3.4	4.7	1.4
73.2	6.7	3.4	3.3	4.6	1.3
75.8	6.8	3.7	3.4	4.7	1.3
78.3	7.0	4.3	3.4	4.8	1.4
80.9	8.0	6.4	5.3	6.4	1.2

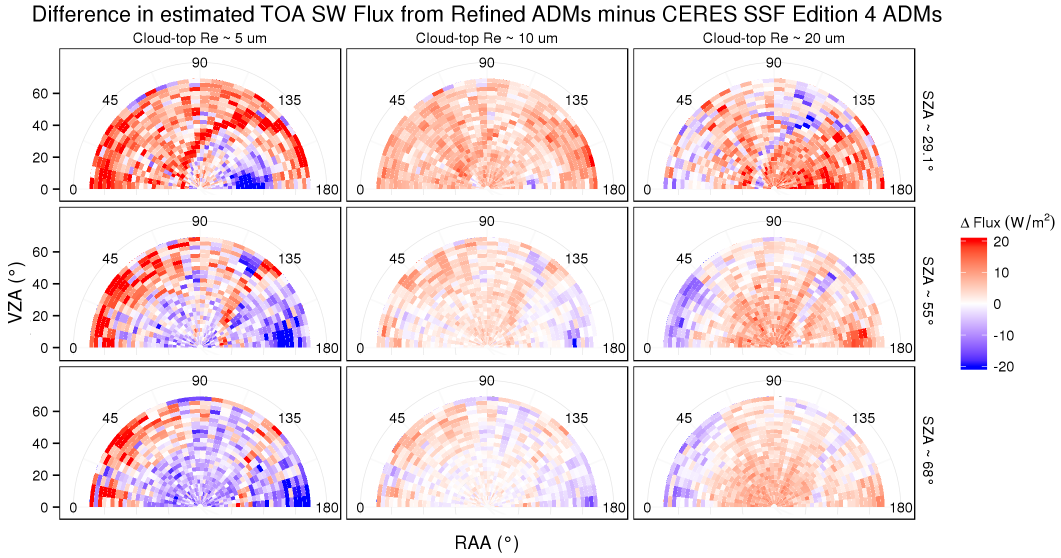

Fig. 4.6: Using TOA SW reflectances predicted from linear models of refined ADMs for three droplet effective radii (varying across panels horizontally) and three θ_s (denoted as SZA; varying across panels vertically), we applied both refined and CERES SSF 4 ADMs to obtain differences in flux estimates (shown in color). Differences beyond ± 20 are not further resolved. Linear models were give a constant cloud-topped water vapor of 4kg m^{-2}.

or 3D effects, produced rather higher reflectances compared to observations. In effect, albedo was slightly overestimated and anisotropies at θ_v lower than 70° were underestimated (by about -0.98% at an θ_s of 29° for θ_v between 0-70°, cloud-top R_e of $10\,\mu$m, and $CTWV$ of 4 kg m^{-2}).

To facilitate a fairer comparison and to avoid further analysis involving an anisotropy bias, we reproduced CERES SSF estimates (referred to as "CERES-like" ADMs). In addition to the footprints shown in Table 4.1, we extracted all CERES footprints of the years 2000-2005 which satisfied $f\tilde{\tau} \approx 10$ and consisted only of liquid condensate, roughly quadrupling the number of samples. As for refined ADMs, we supplemented angular bins which lacked sufficient CERES observations with simulations. Instead of supplementing an angular bin with all simulated reflectances (i.e. one reflectance from each cloud scenario and moisture profile), we sampled from simulations such that the distribution in cloud-top R_e and their level of cloud-topped water vapor corresponded to respective distribution and level of CERES observations within the same θ_s interval. Since footprints had near constant $f\tilde{\tau}$, we skipped the sigmoidal fitting (Section 4.2.3) and simply averaged reflectances per bin. Resulting CERES-like anisotropies compared well with original CERES SSF estimates, and – as expected from the use of simulations beyond θ_v of 70° – were also biased by about -0.98% (at θ_s of 29° for θ_v between 0-70°). We recomputed theoretical flux deviations using refined and CERES-like ADMs and found the positive bias successfully removed for a cloud-top R_e of $10\,\mu$m, as shown in Figure 4.7.

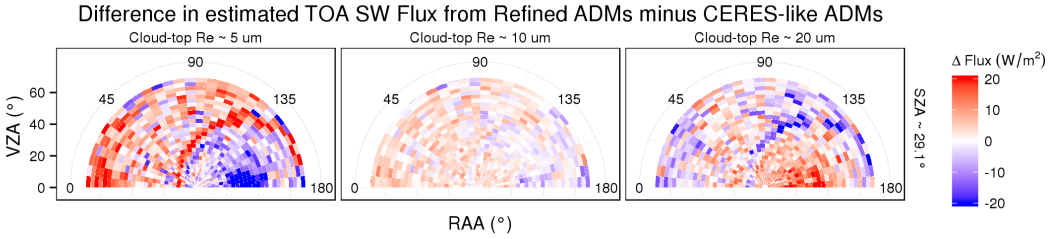

Fig. 4.7: Analogous to Figure 4.6, we compare refined ADMs with CERES-like ADMs at a θ_s of 29°.

Remaining residuals were mostly within 5 W m^{-2}. We found that gathered samples increased in $CTWV$ with lower θ_s (Tab. 4.2) and reached angular bin medians of up to 16.3 kg m^{-2} (at θ_s of 29°). Again, CERES-like ADM construction could have been subject to such sampling and therefore produced ADMs fit to moisture levels higher than 4 kg m^{-2}. Observed flux deviations potentially reflected this CERES sampling bias in cloud-topped moisture.

The CERES cross-track mode collects flux estimates which – when assembled to monthly statistics – provide optimal spatial sampling (Doelling et al., 2013) and allow for benchmark comparisons with global climate model simulations. To examine whether cross-track sampling and the use of refined rather than CERES-like ADMs could produce systematic flux differences, we applied both ADMs to the center months of winter (January) and summer (July) of 2007. Figure 4.8 shows largely positive biases across the globe, reaching significant large-scale biases of about 1-2 W m^{-2} and local levels of up to 10 W m^{-2}.

To investigate whether these large-scale biases were a result of irregular conditions, we examined properties of cross-track samples falling into three regions: SE Atlantic, NE Pacific, and Southern Ocean (highlighted as green rectangles in Fig. 4.8). As shown in Table 4.4, we found a low median cloud-top effective radius ($8.2\,\mu$m) and low median cloud-topped water vapor (1.6 kg m^{-2}) over the SE Atlantic in July. Flux errors of individual samples (-6.4 – 7.9 W m^{-2}) led to median flux deviation of 0.9 W m^{-2}. We found slightly larger median flux differences (1.2 W m^{-2}) in January over the Southern Ocean. However, the distribution of cloud-top effective radius (a median of $10.5\,\mu$m) and cloud-topped moisture (a median of 5.9 kg m^{-2}) appeared ordinary. We believe that deviations in cloud-top effective radius (7.2-$16.2\,\mu$m) and cloud-topped moisture (2.2 – 14.1 kg m^{-2}) from median conditions paired with a variety of viewing and illumination geometries created flux deviations (-6.0-7.0 W m^{-2}) which failed to cancel out to zero.

Tab. 4.4: We present median conditions (in θ_s, cloud-top effective radius, and cloud-topped water vapor) and median flux errors together with their 5th and 95th percentiles (in parenthesis) for two selected regions (SE Atlantic (20°S-0°N, 5°W-13°E) and NE Pacific (15°N-35°N, 140°W-120°W) as shown in Figure 4.8) and two calendar months (January & July of 2007). Asterisks mark significant differences identified in Figure 4.8.

	SE Atlantic		NE Pacific		Southern Ocean	
	January	July	January	July	January	July
No. of footprints	602	2286	655	2376	4474	1004
Solar Zenith Angle (°)	26.6 (17.4–34.6)	41.7 (34.2–49.8)	54.8 (44.7–59.7)	19.0 (10.4–27.9)	44.0 (37.1–52.3)	84.7 (75.7–86.2)
Cloud-top Effectie Radius (μm)	11.0 (8.2–14.4)	8.2 (6.6–14.4)	11.6 (8.0–17.1)	10.4 (7.6–16.0)	10.5 (7.2–16.2)	12.3 (8.8–16.7)
Cloud-topped Water Vapour (kg m^{-2})	16.1 (5.5–29.0)	1.6 (0.0–15.2)	0.0 (0.0–8.3)	11.6 (1.9–32.5)	5.9 (2.2–14.1)	0.5 (0.0-5.9)
TOA SW Flux Difference (W m^{-2})	1.5 (-7.3–12.3)	0.9* (-6.4–7.9)	2.4 (-3.3–9.9)	0.7* (-9.6–12.8)	1.2* (-6.0–7.7)	1.1 (-3.0–10.9)

We repeated the analysis with linear models only dependent on effective radius (of the form: $\ln \rho_o(\theta_s, \theta_v, \phi) = a + b \cdot \ln R_e$) and found similar biases; in part reducing the median difference to CERES-like ADMs (Southern Ocean January: 0.6 W m^{-2}; SE Atlantic July: -0.1 W m^{-2}) and in part increasing it (NE Pacific July: 2.3 W m^{-2}).

In summary, we show that TOA SW anisotropies of refined ADMs captured departures in cloud-top effective radius and cloud-topped water vapor from respective median conditions. Using mean empirical reflectances of extreme cloud droplet size distributions (cloud-top effective radii of 5 and $20\,\mu$m) and comparing CERES ADMs, which were insensitive to such extremes, with refined ADMs, we found deviations in estimated fluxes of up to 20 W m^{-2} at particular viewing and illuminations geometries. When applied to CERES cross-track observations – serving radiation budget climatologies - we demonstrated that the choice of ADM could introduce significant large-scale biases of 1-2 W m^{-2}, locally reaching levels of up to 10 W m^{-2}. In part, we could attribute large-scale biases to regions of persistently small cloud-top effective radii and low cloud-topped water vapor.

4.4 Discussion

Current ADMs over cloudy scenes have been designed to change with cloud optical thickness and cloud phase. However, a sensitivity towards cloud droplet size and cloud-topped water vapor was not considered. We show that TOA SW anisotropy changes substantially in situations deviating from median conditions (e.g. much smaller or larger effective radii than $10\,\mu$m) which could ultimately lead to the introduction of regional flux biases in monthly means. We identified anisotropy driving factors which should be considered in future ADMs.

We believe that observed regional differences in TOA SW fluxes are a result of a sampling bias. Such bias stems from the fact that individual samples rarely meet ADM median conditions for factors impacting anisotropy (such as cloud effective radius and cloud-topped moisture). Moreover, regional samples can deviate from the median systematically (e.g. stratocumulus clouds near continents are more likely to contain larger cloud droplet number concentrations leading to generally smaller droplet sizes). Alternatively, regional samples can have a temporally shifting deviation from median conditions as a changing climate might produce a progressively warmer and moister atmosphere as well as additional cloud condensation nuclei. However, even for regions which meet median conditions (and show a distribution around it), compensation of flux errors (under- and overestimating equally to reach correct monthly means) cannot be guaranteed, as shown in the example “Southern Ocean”. It is the nature of polar orbiting, such as Aqua and

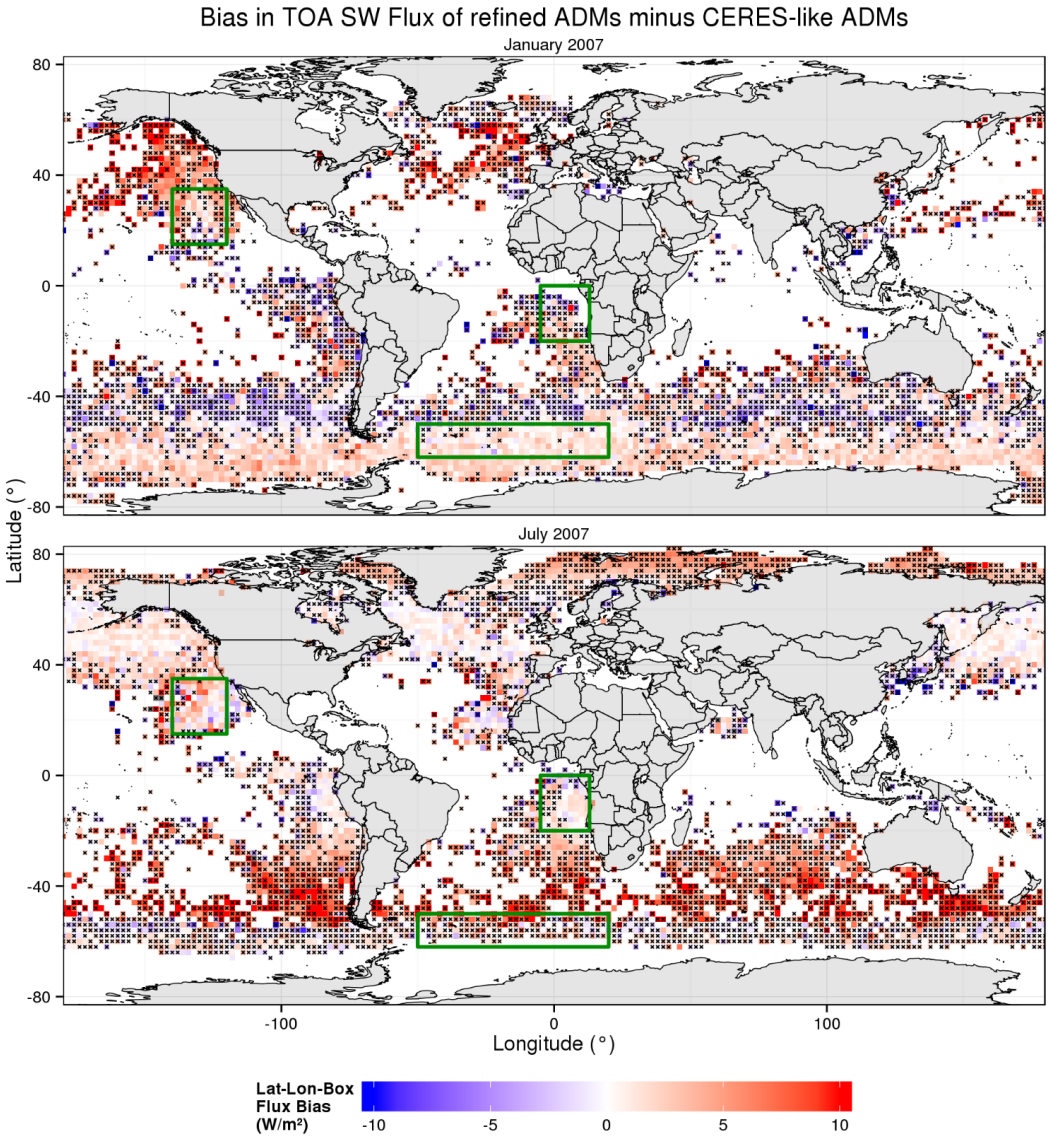

Fig. 4.8: Applied to CERES cross-track measured TOA SW reflectances in January (top) and July (bottom) 2007 over selected conditions ($\tilde{\tau}$ of 10, 100% cloud cover, homogeneous conditions), we found that refined angular distribution models produced mostly higher flux estimates than CERES-like ADMs, shown as positive regional flux biases. Insignificant differences (two-sided student t-test, 95% confidence level) over $2 \times 2°$ latitude-longitude boxes were marked with black crosses. Anisotropy uncertainties were not considered.

Terra, or geostationary satellites, such as the Meteosat series, to perceive regions such that θ_s are co-occurring with certain combinations of θ_v and ϕ. To reach a perfect compensation one needed to capture an underestimated R_e (e.g. $15\,\mu$m; provided that ADMs represent $10\,\mu$m as median condition) where there had been an overestimation of R_e (e.g. $5\,\mu$m) before under identical viewing and illumination geometry.

Most regional flux biases were positive (up to 10 W m^{-2}). Could stratocumulus clouds be more reflective that previously reported? Global climate models persistently produce "too-few-too-bright" low-level clouds (Nam et al., 2012) and show regional biases to CERES EBAF, such as the AM-4 of about 20 W m^{-2} (Zhao et al., 2018). Our samples represent a small portion of all low-level cases. Future work should incorporate footprints of other cloud fractions and cloud optical thicknesses to obtain a more representative picture.

Lastly, improved instantaneous flux from refined ADMs estimates should benefit closure assessment experiments such as the future EarthCARE mission (Illingworth et al., 2015). The foreseen broadband radiometer (BBR) will observe SW radiances at three along-track viewing angles (nadir-viewing as well as $\theta_v \approx 55^\circ$ forward and backward viewing) and, correspondingly, produce three SW flux estimates. In contrast to the CERES cross-track mode – BBR viewing geometries will be much closer to the principal plane and therefore more sensitive to cloud-top effective radii. We expect a better agreement in estimated fluxes across the three along-track views. Future work should verify such consistency of developed ADMs by using multi-viewing instruments such as MISR (Diner et al., 1998).

Acknowledgements

We thank Ralf Bennartz, Bjorn Stevens and Nicole Docter for helpful discussion. This work was possible through funding within the ESA contract 4000112019/14/NL/CT. The authors would also like to thank the anonymous reviewers for their constructive and helpful comments, and to the Atmospheric Sciences Data Center at the National Aeronautics and Space Administration, Langley Research Center, for providing them with the Clouds and the Earth's Radiant Energy System Single Scanning Footprint TOA/Surface Fluxes and Clouds data product.

5

On the use of Simulated Photon Paths to Co-register TOA radiances in EarthCARE Radiative Closure Experiments

Abstract

The Earth's Cloud, Aerosol and Radiation Explorer (EarthCARE) mission will retrieve vertical profiles of cloud and aerosol properties by combining data from active and passive instruments. The verisimilitude of retrievals will be assessed using data from its broadband radiometer (BBR), which measures top-of-atmosphere (TOA) shortwave (SW) radiances at three along-track viewing angles. BBR measurements will be compared to their modelled counterparts, simulated by a 3D Monte Carlo (MC) radiative transfer model acting on retrieved properties, thus defining a radiative closure experiment. Since cloud and aerosol microphysical and hence optical properties within each assessment domain vary horizontally and vertically, one challenge facing the closure process is selection of radiances that will foster the best assessments of retrievals. This study investigates whether co-registration of radiances for closure assessment can be aided by information pertaining to photon paths from the MC model. Unlike methods that provide one effective reflecting layer (ERL), such as cloud top altitude, simulated photon paths can account for several reflecting layers. For this study, A-Train satellite data provided cloud properties. The MC model was applied to this field to simulate BBR-like measurements. Cloud properties were then perturbed randomly, to roughly represent retrievals, and the MC model reapplied to them. The resulting sets of radiances mimicked EarthCARE measured and modelled data thus allowing a test of closure and co-registration methodologies. Through the use of 3D photon path information, the rate of identification of inaccurate cloud retrievals improved over ERL approaches by ∼4% for Cirrus clouds and ∼15% for broken clouds. For large-scale Deep Convective clouds, however, inaccurate photon paths, ostensibly due to poor retrievals, reduced identification performance by 3%.

Tornow, F., Barker, H. W., Domenech, C., (2015), Quarterly Journal of the Royal Meteorological Society, 144 (693), 3239-3251, DOI: https://doi.org/10.1002/qj.2606

5.1 Introduction

Changes to cloud and aerosol properties influence Earth's radiation budget, hydrological cycle, and climate at all scales, and so knowledge of their physical attributes is essential for confident modelling of local and global climatic change (Boucher et al., 2013). To adequately assess and improve the representations of cloud, aerosol, and radiation in global models requires sound information pertaining to their spatial and temporal properties on a global scale (e.g. Webb et al., 2001; Zhang et al., 2005; Cole et al., 2011). Following the lead of satellites in the so-called A-Train (Stephens et al., 2002; Wielicki et al., 1996; Winker et al., 2009), the Earth's Cloud, Aerosol and Radiation Explorer (EarthCARE) mission, to be launched no sooner than 2016, will be equipped with a lidar (ATLID), a cloud profiling radar (CPR), and a passive multi-spectral imager (MSI). A synergistic algorithm using data from all three sensors (cf. Delanoë and Hogan, 2010), and a suite of additional algorithms that operate on data from individual sensors will furnish profiles of cloud and aerosol properties for 1 km^2 columns along its nadir-track (ESA, 2001).

In contrast to previous missions, EarthCARE was designed from the outset to assess the verisimilitude of its retrieved products. This will be achieved via a radiative closure experiment using data from EarthCARE's fourth instrument; a broadband radiometer (BBR) which will measure reflected solar and emitted thermal radiances at three along-track viewing angles. For each three dimensional (3D) assessment domain D, with cross-sectional areas of $\sim$100 km^2, measured BBR values will be compared to their simulated counterparts that will be obtained by applying 3D radiative transfer models to the retrievals. For nadir BBR radiances associated with D, there is little ambiguity that those radiances are determined much, but not entirely, by cloud and aerosol microphysical and hence optical properties (hereafter denoted as *attenuators*) in D. Hence, closure assessments performed with nadir radiances are quite straightforward. Unfortunately, however, nadir BBR radiances are often highly correlated with nadir MSI narrowband radiances which will be employed in the retrieval process. As such, closure tests with nadir radiances are neither too demanding nor too informative.

On the other hand, closure tests using radiances from the BBR's two off-nadir views are generally much more demanding and involve data not used for retrievals. The complication with them arises because off-nadir views can be much less determined by attenuators in D, for radiances associated with them have lines-of-sight that traverse other domains. The challenge is therefore to establish which off-nadir radiances afford the best "view" of D. This amounts to a problem of co-registering off-nadir radiances with attenuators in D. Difficulties increase as cloudiness becomes partial or semi-transparent. Thus, the main point of this study is to demonstrate that

existing co-registration methods lack the ability to adequately determine which radiances will provide the best closure assessments, and to offer an alternate method that is especially suited to missions with active and passive sensors. For this exploratory study, only shortwave BBR radiances are considered.

In the following section, EarthCARE's closure assessment experiment is recounted briefly along with a discussion on the importance of co-registering radiances for closure assessment. Section 5.3 explains the conventional approach to radiance co-registration along with the new alternate method. Section 5.4 discusses a metric for establishing retrieval accuracy. Sections 5.5 and 5.6 present data and models used in this study in as well as results. The final section offers a summary and conclusion.

5.2 EarthCARE's radiative closure assessment

The objective of EarthCARE's radiative closure assessment is to aid developers of EarthCARE's cloud and aerosol retrieval algorithms, and users of their products, by demonstrating how well its BBR radiances can be reproduced by radiative transfer models that operate on the retrieved cross-section (RXS) (see Illingworth et al., 2015). BBR measurements consist of shortwave (SW) and totalwave (TW) channels with a nadir view and forward and backward along-track views at a viewing zenith angle of $\sim$55°. The telescopes are aligned such that they observe approximately a 10 km wide swath centred on the $\sim$1 km active-passive RXS.

Using the scene construction algorithm of Barker et al. (2011), 3D domains will be constructed around the RXS using both the RXS profiles and MSI narrowband radiances. The cross-track width of the constructed domain will exceed the BBR's footprint by at least 10 km on both sides. 3D radiative transfer models will then be applied to the constructed domains thereby producing simulated BBR data (Barker et al., 2012). From early on, the success of EarthCARE's retrievals has been expressed in terms of being able to reproduce BBR radiance-inferred fluxes to within $\sim$10 W m^{-2} for each assessment domain D. When radiances are being compared, they will be multiplied by π so that their magnitudes will be commensurate with fluxes.

The radiative closure assessment will begin by comparing nadir measured and modelled BBR radiances. For at least two reasons this is the weakest test. First, active-passive synergistic retrieval algorithms (e.g. Delanoë and Hogan, 2010) might rely much on MSI nadir radiances which are often highly correlated with BBR nadir radiances (Barker et al., 2014b). Hence, there is not a clean separation between variables used by retrievals and their assessment. Second, the purpose of the closure test is to assess the entire retrieved column. Of all radiances, nadir radiances are

determined much by conditions near cloud tops; retrievals well below cloud tops will often figure only weakly into the assessment.

The assessment will then progress to off-nadir radiances. Arguably, these radiances afford the most stringent assessment of retrievals for not only do these views differ radically from that used by the retrieval algorithms, but regions well below cloud tops can, at times, determine off-nadir radiances much thus providing a stronger test of the retrieved *profile* than that afforded by nadir radiances alone (cf. Barker et al., 2014a).

The final step in the assessment involves comparing fluxes simulated explicitly by the radiative transfer models at the specific altitude z_D to upwelling fluxes deduced from the application of angular distribution models (ADMs) to BBR measured radiances. An ADM uses information about angular characteristics of reflected or emitted radiation, ideally for a set of scenes characterized by geophysical and meteorological parameters, to estimate corresponding fluxes (e.g. Suttles et al., 1988; Domenech and Wehr, 2011). While these comparisons involve quite different quantities, and thus facilitate a satisfactory closure assessment, they carry additional uncertainty into the assessment via the ADMs and co-registration of measured radiances to the flux level z_D.

This study is limited to assessments involving radiances; assessment of fluxes is considered in a separate study. However, as with flux estimation, a crucial step when using radiances in closure assessments is establishment of the most appropriate radiances. In other words, how should radiances be co-registered to an assessment domain? The importance of this question to TOA closure assessment is addressed in the following section together with potential solutions.

5.3 Co-registering radiances: requirements and methods

This section begins by explaining issues associated with, and the importance of, co-registration of radiances for closure experiments. This is followed by discussion of co-registration of radiances to an effective reflecting layer within D, as well as a new method that utilizes information retrieved from the active-passive sensors.

5.3.1 Requirements to co-registration of off-nadir radiances

In contrast to nadir observations, oblique radiances will have lines-of-sight that traverse 3D domains other than the particular D which is being assessed. Hence, oblique TOA radiances have the potential to contain much *information* about the nature of attenuators in several domains in addition to D. To allow for an assessment of D via oblique TOA radiances, the most meaningful radiances must be identified. Without identification, a contrast between oblique TOA radiance measurement and simulation would merely indicate retrieval inaccuracy, but would be unrelated to any particular geophysical or meteorological conditions. The problem is minimized when D has a strongly reflecting layer that is clearly visible in oblique radiances (e.g Wylie et al., 1998; Zong et al., 2002). In general, however, clouds can be semi-transparent with multiple reflecting layers present in D, and clouds in D can be either blocked by clouds in front of D, or their contribution to radiances overpowered by backlighting from reflecting layers or surfaces behind D (cf. Barker et al., 2014a). Hence, when observing D from an off-nadir perspective, the following question arises: which off-nadir radiances are most useful for assessing retrievals in D?

A possible answer to this question might be the use of radiances with contributions from D-like attenuators that arise from regions outside of D. Here, D-like implies similar cloud and aerosol properties to those in D. Following this idea, if attenuators in neighbouring domain are D-like and at altitudes close to the dominant attenuators in D, radiances that pertain mostly to these attenuators might be appropriate for use in the assessment of D? Consequently, finding off-nadir radiances with lines-of-sight that traverse D and adjacent domains with D-like attenuators that match the nadir line-of-sight (D's vertical attenuating structure) would, therefore, be likely candidates for assessing retrieval inaccuracies in D.

Figure 5.1 provides a schematic illustration of this problem when three radiances are co-located with the top of the highest reflecting layer (HRL) (see section 5.3.2). The left side represents the most tractable situation: a single, highly reflecting layer whose top is in plain view to all three viewing directions, and, hence, the same attenuating structure is commonly observed. The majority of the information in all radiances comes from clouds within, and near the top of D. The right side illustrates a more complex case: an upper-level semi-transparent cloud layer above a small, but dense, low cloud that is situated mostly in D. In this case, off-nadir radiances co-located with the HRL contain information about the underlying surface and the higher cloud layer, but not the lower cloud which represents the bulk of the retrieved attenuators in D. According to the hypothesis presented in the previous paragraph, the best choice of off-nadir radiances to be used for assessment of retrievals in D would be those that intersect both the lower cloud and the higher cloud structure; not those co-located with the HRL. Section 5.3.3 presents a method,

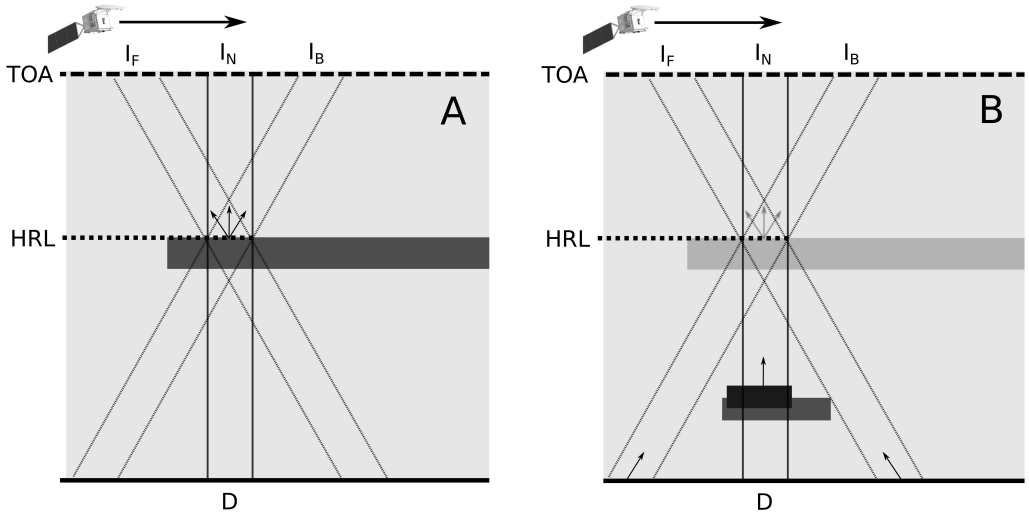

Fig. 5.1: Panel A shows a single, strongly reflecting layer (heavily shaded), which forms the common surface for all three radiances (I_F, I_N, and I_B). In panel B, the same layer is now semi-transparent (lightly shaded) and located above a small dense cloud. If I_F, I_N, and I_B that were used in Panel A are also used in Panel B, contributions to radiances will no longer stem from a well-defined region of cloud, but instead from very different clouds, and potentially even surfaces.

which supports finding the oblique radiances that are most likely to pass through D-like attenuators.

5.3.2 Co-registration at the effective reflecting layer

From the description of the problem given in section 5.3.1, finding ideal off-nadir radiances for assessment of retrievals in D requires much information about the 3D structure of attenuators in and around D. However, satellites that carry only passive radiometers provide very limited information about the vertical structure of cloud. Given this shortage of information, a solution has been to take a single vertical level for each D where off-nadir radiances intersect. This effective reflecting layer could be at a constant height, such as the surface (SRF) (Smith et al., 2004; Loeb et al., 2002).

If, however, one has estimates of cloud top heights, the effective reflecting layer can be at each domain's HRL; that is, the uppermost layer whose reflectance significantly exceeds that of a pristine atmosphere (Moroney et al., 2002). Once the height of this layer, h_{ERL}, in D is established, the horizontal shift l_{obl}, before and after the nadir observation, needed for the forward and backward views to intersect at h_{ERL} can be defined as

$$l_{obl} = (H - h_{ERL}) \tan \theta_v \tag{5.1}$$

where H is the satellite's altitude, and θ_v is off-nadir viewing zenith angle ($\theta_v = 55^\circ$ for EarthCARE's BBR). Letting D be at along-track position i, co-registration at h_{ERL} provides the set $S(i)$ of backward-viewing, nadir-viewing, and forward-viewing radiances:

$$S(i) = \{\mathrm{I}_B(i + l_{obl}), \mathrm{I}_N(i), \mathrm{I}_F(i - l_{obl})\} \tag{5.2}$$

As outlined in the previous subsection, the cloud-top layer is ideal for co-registration when the cloud is optically thick and the view of it from off-nadir directions is not blocked. In addition, a largly horizontally homogenoues structure (e.g. a more extended lower cloud layer in Figure 5.1) allows finding off-nadir lines-of-sight that traverse entirely through attenuators that resemble those in D. However, the more horizontally heterogeneous the local structure, the more likely it is that nearby D-like attenuators are rare or non-existent.

5.3.3 3D Monte Carlo photon paths and Maximum Similarity co-registration

The following sub-subsections present a new source of information based on results from a 3D Monte Carlo RT model, and a way to use this information for radiance co-registration.

3D Monte Carlo model and photon paths

In order to improve co-registration of nadir and off-nadir radiances so as to enhance the usefulness of radiative closure assessments that employ the three BBR radiances, a 3D Monte Carlo RT model (Barker et al., 2003) will be applied to active-passive retrievals of cloud and aerosol.

Monte Carlo RT models are classic Monte Carlo solutions to the integro-differential transport equation subject to, usually, non-analytic boundary conditions. Ensembles of photons are injected across a 3D domain containing retrieved cloud and aerosol properties, as well as gas and surface parameters. Photon paths and locations of scattering events (involving Earth surfaces, cloud ice crystals, cloud droplets, aerosol particles, and air molecules) are determined by selecting values from probability distributions and randomly-generated numbers. Let $\zeta_{j \to i,k}$ be the n^{th} photon cluster

contribution emerging at the top of the domain at the i^{th} column due to a scattering event involving the k^{th} constituent in the j^{th} column at altitude z. Thus,

$$\zeta_{j\rightarrow i,k}(n) = w(n)\omega_o(n)p_k(\theta,\varphi,\theta',\varphi',z(j)) \exp\left[-\int_{z(j)}^{z_{M(i)}} \beta(z')\,\mathrm{d}z'\right] \tag{5.3}$$

where $p_k(\theta,\varphi,\theta',\varphi',z(j))$ is the k^{th} constituent's bidirectional function, which describes the probability of radiation travelling in direction (θ',φ') being scattered at altitude $z(j)$ in the j^{th} column into direction (θ,φ) toward the sensor at the top of the i^{th} column at altitude $z_{M(i)}$, $\omega_o(n)$ is single-scattering albedo, $w(n)$ is the weight a photon cluster had upon arriving at $z(j)$ after previous collisions, and $\beta(z)$ is extinction due to all constituents along the path from $z(j)$ to $z_{M(i)}$. An expression similar to ζ describes contributions from surface reflection. Horizontal dimensions of columns are fixed at Δy across-track, and variable Δx along-track.

Summing over all contributions, simulated radiance at $z_{M(i)}$ is

$$\mathcal{I}^{\pm,0}(i) = \frac{1}{N_{cell}} \sum_k \sum_n \zeta_{j\rightarrow i,k}(n) \tag{5.4}$$

where N_{cell} is the number of photon clusters injected onto the top of each column. Implicit in $\mathcal{I}$ is spectral integration, meaning that terms in $\mathcal{I}$ are actually spectral-dependent. BBR measured counterparts of $\mathcal{I}^{\pm,0}$ are $\mathrm{I}^{\pm,0}$. Since the sum of photon cluster contributions represents the total TOA radiance, each cluster contribution can be regarded as a radiance contribution (Marchuk et al., 1980).

Using the same MC model as used here, Barker et al. (2014a) used all radiance contributions leaving a domain D to estimate whether oblique TOA radiances receive sufficient radiation scattered from clouds and aerosols in order to carry out a meaningful radiative closure assessment of retrieval quantities in D. Here, on the other hand, radiance contributions stemming from scattering events are accumulated for each cell. Figure 5.2 illustrates the extracted information for nadir and forward line-of-sight radiances. Each simulated radiance has stored information on the vertical origin and amount of radiance contribution along its line-of-sight. These photon paths allow consideration of 3D effects, as presented in the next part.

Maximum Similarity co-registration

In order to evaluate retrieved parameters in D, off-nadir radiances are required (section 5.3.1). To identify the off-nadir radiances (for each forward and backward viewing angle) that will be most useful for drawing conclusions about the quality of

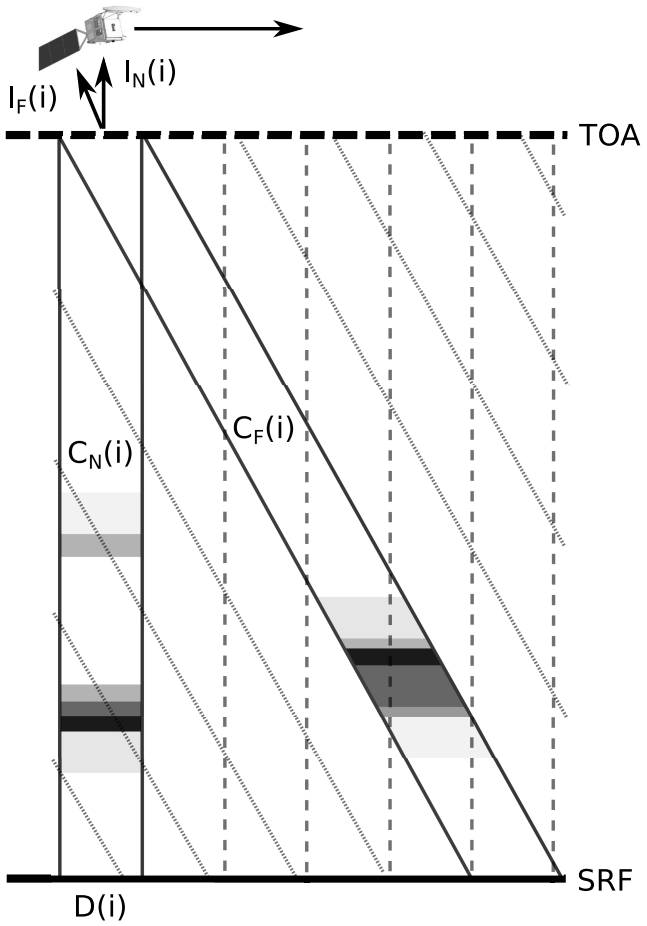

Fig. 5.2: Schematic showing the concept of radiative contributions to top-of-atmosphere (TOA) radiance that derive from scattering events, due to certain attenuators, at various positions along lines-of-sight (nadir: $C_N(i)$, forward view: $C_F(i)$) as simulated by a 3D MC model (shades of grey correspond to varying amounts of radiance contribution). The assessment domain of interest, $D(i)$, reaching from the surface (SRF) to TOA, is fully captured by $C_N(i)$, while $C_F(i)$ contains contribution from neighbouring domains. Summing over all layer contributions for all types of attenuators yields TOA radiance ($I_N(i)$ and $I_F(i)$, respectively).

retrieval in D, many methods use a common surface in D, where all views intersect (section 5.3.2). A hidden assumption to make, however, is atmospheric homogeneity along the satellite track; ensuring that lines-of-sight of selected radiances always traverse through a similarly characterized atmosphere in- and outside of D. But it is easy to see the possibility of co-registered radiances being inconsistent in cases of partial or semi-transparent clouds. The previous sub-subsection presented a source of information that might be usual when dealing with inhomogeneous clouds. This sub-subsection aims at exploiting the newly gained information.

Instead of defining D's structure by a common surface (e.g. its highest reflecting layer), this approach uses the profile of reflecting layers along the nadir line-of-sight. To find an off-nadir radiance and take inhomogeneity into account, we compare this nadir profile pair-wise against a subset of oblique profiles. Subsequently, a similarity measure identifies the oblique profile, which best resembles the nadir profile, and attributes the according off-nadir radiance of that oblique profile to D. This approach is hereafter referred to as Maximum Similarity (MXS) co-registration. Similar to an assumed *true* effective reflecting layer, MXS co-registration is based on the assumption that the retrieved 3D atmosphere, used in the MC model, is a good approximation of the actual distribution of attenuators. The following discussion presents the MXS co-registration method.
To define the structure of domain D at along-track position i, use the vertical profile of radiance contributions, C_N, as observed by the nadir view, with

$$C_N(i) = (\zeta_{i,m=1}, \ldots, \zeta_{i,m=n_z}) \tag{5.5}$$

where n_z is number of vertical layers, and $\zeta_{i,m}$ is radiance received from the m^{th} layer.
To find the off-nadir radiance which consists of radiative contributions coming from an attenuating structure most similar to D's structure, first, select a subset of potential off-nadir candidates. These off-nadir radiances should intersect the nadir column with their lines-of-sight. Therefore, all off-nadir radiances between the intersection at TOA, at along-track position i, and the intersection close to the surface at along-track position $i \pm l_{SRF}$ (for forward/backward view) are considered, with l_{SRF} derived from equation 5.1 with $h_{ERL} = 0$ km. To illustrate this, the set of off-nadir forward view profiles

$$F(i) = \{C_F(i), \ldots, C_F(i + \Delta l_{SRF})\} \tag{5.6}$$

will be compared, piece-wise, to the nadir profile. To achieve this, a similarity metric is used. The cosine similarity s_F (e.g. Kohonen et al., 2001), defined as

$$s_{\mathrm{F}} = \left\langle \frac{C_N}{\|C_N\|}, \frac{C_{\mathrm{F}}}{\|C_{\mathrm{F}}\|} \right\rangle = \cos\tau = \frac{\sum_{m=1}^{n_z} C_N^m \cdot C_{\mathrm{F}}^m}{\|C_N\| \|C_{\mathrm{F}}\|} \tag{5.7}$$

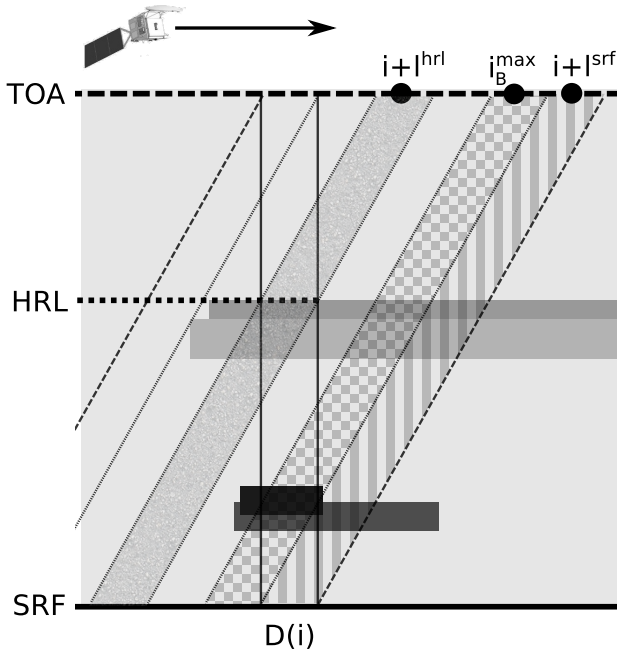

Fig. 5.3: Schematic showing a fictitious cloud extinction field (darkening shades correspond to increasing extinction). A backward-viewing radiance is to be selected for assessment of retrieved cloud products in column $D(i)$. The highest reflecting layer method uses radiance at location $i + l_{HRL}$; co-registering to the surface uses radiance at location $i + l_{SRF}$; the maximum similarity (MXS) method uses radiance at location i_B^{max}.

where τ is the angle between vectors C_N and C_F, describes the extent to which D's nadir and, in this case, forward profiles resemble one another. When $s_F = 1$, both profiles are identical; when $s_F = 0$, they bear no similarity at all. In general, the off-nadir radiance contribution profile that most resembles that of D's nadir profile is defined as

$$i_F^{max} = \arg\max_i [s_F(i), \ldots, s_F(i + \Delta l_{SRF})] \tag{5.8}$$

with the TOA radiance $I_F(i_F^{max})$ to be used to assess retrievals in D. Performing this procedure for forward and backward views yields a set S_{MXS} of co-registered, multi-angular TOA radiances for each D designated as

$$S_{\text{MXS}}(i) = \{I_B(i_B^{max}), I_N(i), I_F(i_F^{max})\} \tag{5.9}$$

Taking the entire profile into account, radiance co-registration can be performed for any collection of attenuators in D.

Figure 5.3 contrasts MXS co-registration with the previously presented single effective layer approaches (for backward viewing). This schematic demonstrates how various methods of co-registering off-nadir radiances can lead to substantially different radiances being selected for use in the assessment process.

5.4 Performance measure of co-registation methods

This section elaborates on an objective metric for evaluating co-registration methods with respect to their larger purpose in EarthCARE: identification of inaccurate cloud property retrievals in 3D domains.

In detail, co-registration aims at selecting off-nadir radiances such that their lines-of-sight traverse through the same or a similar atmospheric 3D structure as the nadir view. Supposing that similar atmospheric structures are retrieved with a similar degree of accuracy, successful co-registration leads (for each domain) to a set of BBR measured, and corresponding selected MC simulated radiances, which differ similarly at each of the three viewing angles due to underlying retrieval inaccuracies. If, on the other hand, co-registration fails to select appropriate off-nadir radiances, that is, nadir and off-nadir views observe different atmospheric structures likely retrieved with individual inaccuracies, radiance differences (between measurement and simulation) among viewing angles are assumed to appear inconsistent. Therefore, we propose to measure the agreement of radiance differences among all three view angles to infer the performance of a co-registration method in the framework of EarthCARE's radiative closure assessment. The following presents a detailed concept for the performance metric along with underlying assumptions.

For evaluation purposes, it is presupposed that D's or a D-like attenuating structure (i.e., its clouds and aerosols) reflect radiation according to a characteristic bidirectional function. Capturing three viewing angles of that bidirectional function should provide an indication of the successfulness of the co-registration method. Facing inaccurate retrieval, it is assumed additionally that bidirectional function will be amplified or reduced at all directions. In other words, the relative difference d_i^v between measured I_v and simulated radiance $\mathcal{I}_v$ defined as

$$d_i^v = \frac{\mathrm{I}_v(i) - \mathcal{I}_v(i)}{\mathrm{I}_v(i)} \tag{5.10}$$

is assumed to be equal over all three viewing zenith angles $v \in \{B, N, F\}$ for a domain at along-track position i.

Assuming equal relative differences simplifies evaluation of co-registration methods. The assumption reflects a well retrieved shape of D's bidirectional function but not of its intregration, the albedo. The main idea of the metric is to reward a co-registration method that manages to point at a common bidirectional function, and thus obtain relative differences of a similar magnitude over nadir and selected off-nadir views.

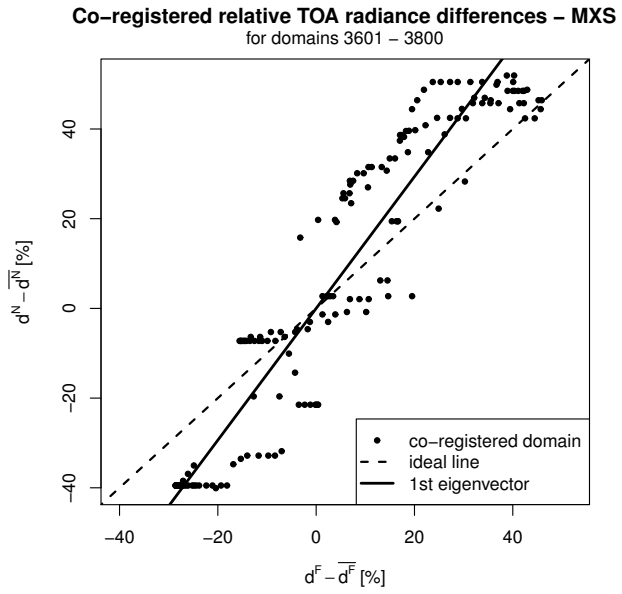

Fig. 5.4: This graphic concerns the co-registration performance metric of section 5.4. For illustration a 2D space is shown, instead of 3D space. Co-registered relative differences in nadir d^N and forward d^F (centred through their respective means $\overline{d^N}$ and $\overline{d^F}$) form a cloud of points around the ideal vector $\vec{u}$ (dashed line), representing equal relative differences. The first eigenvector $\vec{w}_1$ (solid line) in the 2D relative radiance difference space is computed for selected domains. The performance measures the alignment of both $\vec{u}$ and $\vec{w}_1$.

Considering all three viewing angles, we obtain the triplet

$$m_i = \left(d_i^B, d_i^N, d_i^F\right) \tag{5.11}$$

of relative differences for each domain. According to our assumption, the coordinates of m_i ideally form a point on the line $\vec{u} = (1,1,1)n$, with $n \in R$, as shown in Figure 5.4. Considering n_D assessment domains yields n_D points around $\vec{u}$.

To determine how well the n_D points agree with $\vec{u}$, first form the set $X \in R^{3\times n_D}$ of all n_D triplets. This "centering matrix" is defined for all three dimensions as

$$X = [m_1, \ldots, m_{n_D}] - \left(\frac{1}{n_D} I^T [m_1, \ldots, m_{n_D}]\right) I \tag{5.12}$$

where I is the column-vector of n_D Ones, and T denotes the matrix transpose. Consequently, the second term of equation 5.12 establishes a mean-value of 0, for each of the three columns in X.

From the covariance matrix XX^T one can obtain eigenvectors $W = [\vec{w}_1, \vec{w}_2, \vec{w}_3]$ with $W \in R^{3\times3}$, and corresponding eigenvalues $\lambda = [\lambda_1, \lambda_2, \lambda_3]$ from

$$XX^TW = \lambda W \tag{5.13}$$

The first eigenvector $\vec{w}_1$ will most likely correspond to the variance of a similar direction as the vector $\vec{u}$ as illustrated in Figure 5.4. The projection of the normalized eigenvector $\vec{w}_1$ onto normalized $\vec{u}$ reveals how parallel both vectors are, and thus how equal relative TOA radiance differences among viewing angles are. The eigenvalue λ_1 tells the percentage of explained variance by this eigenvector. Accordingly, define co-registration performance P as

$$P = \left(\frac{\vec{w}_1}{||\vec{w}_1||} \cdot \frac{\vec{u}}{||\vec{u}||} \right) \cdot \lambda_1 \cdot 100\% \tag{5.14}$$

For $P = 100\%$, all points are located on $\vec{u}$. In the worst case, $P = 0\%$; points in X form a line perpendicular to $\vec{u}$. For all other cases, $\vec{w}_1$ might still line up with $\vec{u}$, but due to scattering of points around $\vec{u}$ it may be that either $\lambda_1 < 1$ or, alternatively, $\vec{w}_1$ and $\vec{u}$ do not line-up, leading to an inner product smaller than 1. In the latter case, scattering of points around $\vec{w}_1$ may reduce P further.

Based on the simplifying assumption, the metric clearly fails if the bidirectional function of D or a D-like structure is incorrectly retrieved or if the assumed optical properties for clouds are incorrect. In this case, it could be that a well working co-registration method is *penalized* incorrectly. In case a co-registration method selects off-nadir radiances which do not point at D or D-like structures, but, by pure chance have similar relative differences to their counterparts compared to the nadir view, we would falsely reward a poor co-registration method. As the performance metric evaluates numerous domains at the same time, chances are low to alter the performance critically.

5.5 Test data and Monte Carlo model runs

To test the algorithms proposed here, this study employs data from the following A-Train satellite instruments: CloudSat's Cloud-Profiling Radar (CPR); CALIPSO's (Cloud-Aerosol Lidar and Infrared Pathfinder Satellite Observations) lidar; Tera's MODIS (Moderate Resolution Imaging Spectroradiometer); and CERES (Clouds and Earth's Radiant Energy System). Data from these sources have been coordinated (Sun-Mack et al., 2010; Kato et al., 2010) into the CERES-CALIPSO-CloudSat-MODIS (CCCM) product. This study used a 5,000 km-long section of CCCM data measured on 5 July 2006 over the equatorial Pacific (from 143.54°W, 17.25°S to

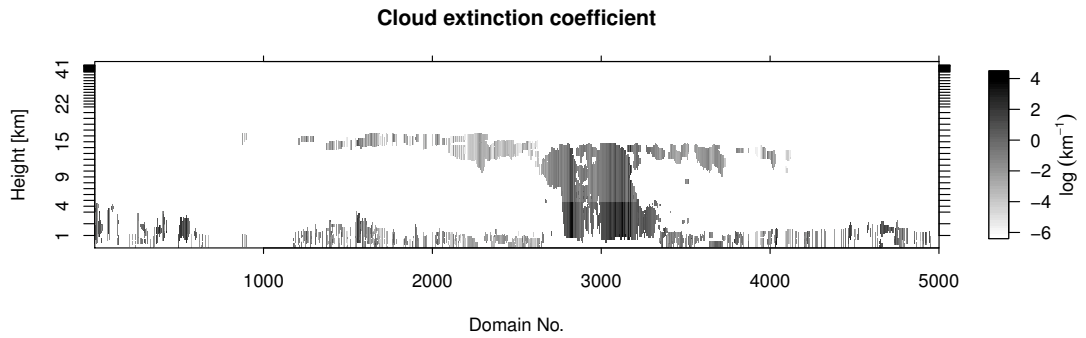

Fig. 5.5: Cross-section of A-train-derived cloud extinction coefficient used in this study. The track was measured on 5 July 2006 over the equatorial Pacific Ocean (from 143.54°W, 17.25°S to 153.48°W, 27.32°N).

153.48°W, 27.32°N). Figure 5.5 shows retrieved cloud extinction cross-section. The vast majority of the track was over ocean.

CCCM data provides CERES radiances close to nadir. For the present study, however, BBR data are required at the three EarthCARE viewing angles. Hence, they had to be generated by applying a 3D Monte Carlo model to CCCM data. But first, the CCCM cross-section needed to be expanded cross-track. This was achieved by applying the Barker et al. (2011) scene construction algorithm. The constructed domain was 31 km wide, but only the central 10 km were used for analyses; with across-track buffer-zones of 10 km to the East and 11 km to the West.

A *control* set of BBR-like measurements were produced by applying the MC model to the constructed CCCM domain. In the MC model, gaseous transmittances (H_2O, CO_2, O_3) were computed using the correlated k-distribution method (Li and Barker, 2005; Salzen et al., 2013). Optical properties for liquid droplets (Wiscombe, 1980) and ice crystals (Yang et al., 2013) were resolved into four bands consisting of 31 quadrature points in the range of 0.25 to $4.0\,\mu$m (for details see Barker et al., 2014b). Rayleigh scattering was included as was attenuation by continental tropospheric aerosol (Deepak and Gerbers, 1983) which blanketed the domain with optical depth 0.15 at wavelength 0.55 μm with extinction decreased exponentially with altitude at a scale height of 1 km. Two types of surfaces were used: Cox and Munk (1956) distribution of wave slopes coupled with Fresnel reflection; and Lambertian (Barker and Davies, 1992). For more details, see Barker et al. (2012). No instrument filter functions were applied.

In addition to the *control* set, a *perturbed* set was generated, too. The *perturbed* domain was the same as the *control* except that cloud liquid and ice water contents and droplet effective radii and crystal effective diameters were invested with random

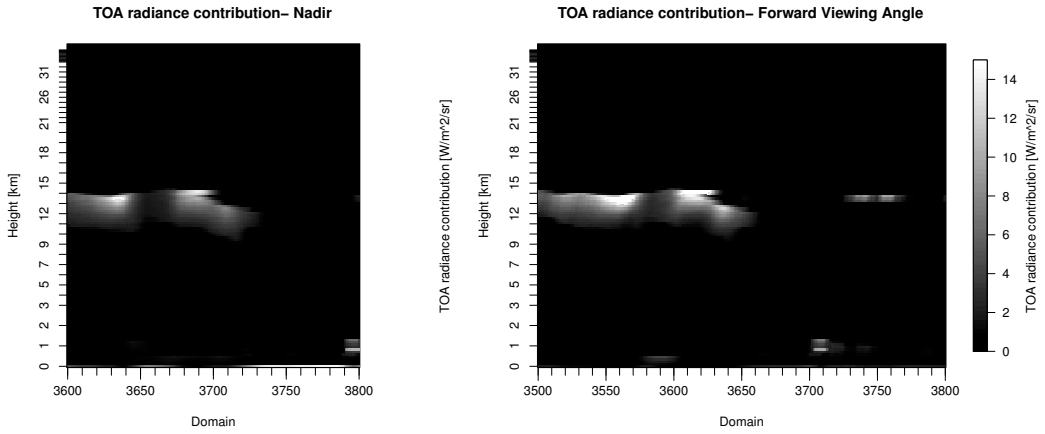

Fig. 5.6: Radiance contribution fields for nadir (left) and foreward view (right). In both plots, the domain number indicates the column at which the radiance contribution arrived. As such, the Cirrus cloud appears at smaller domain numbers in the forward view. Figure 5.9 shows co-registration results for the same sector.

uncorrelated variations (up to $\pm 25\%$ of the absolute property value) (per. comm. Pavlos Kollias, 2014; Robin Hogan, 2014). This domain was meant to represent the retrieved version of the *control* domain. The MC model was then applied to the *perturbed* domain producing TOA radiances at the three viewing directions as well as photon paths and contributions necessary for the application of the method described in section. Figure 5.6 presents a sample for nadir and forward viewing radiance contributions.

In order to estimate MC uncertainties, both *control* and *perturbed* simulations were performed 100 times using 3×10^6 photons per sample for a total of 3×10^8 photons over the domains of each experiment. Each sample of the *perturbed* experiment used a unique random perturbation of the *control* field.

5.6 Results

As noted before, EarthCARE will perform a closure assessment in order to verify cloud and aerosol properties retrieved for small 3D domains. A closure using TOA radiances involves a comparison of measured BBR radiances against their simulated counterparts; for nadir and, more importantly, off-nadir viewing angles. However, off-radiances need to be carefully selected so as ensure that they suitably correspond to the 3D domain defined by the nadir footprint. Co-registration aims at the common observation of the same or a similar attenuating structure. Because attenuators (clouds and aerosols) within each domain may appear in different heights and be vertically complicated, different co-registration methods have aimed to improve attribution by using different sources of information pertaining to height and

complexity. Foremost, Cirrus clouds appear semi-transparent at solar wavelengths, and so multiple reflecting layers are likely to contribute to single SW TOA radiance. To investigate whether a new source, namely 3D MC photon paths, could improve the selection of relevant oblique radiances, the new co-registration method and two existing ones, namely SRF and HRL, were applied to test cases.

As shown in section 5.5, EarthCARE's BBR-measured and simulated TOA radiances were mimicked by applying the 3D MC model to A-train satellite data and generating data for *control* and *perturbed* experiments. Based on a horizontal resolution of 1 km^2 of the 10 km $\times$ 5000 km track, we averaged domains over (10 km)^2, overlapping their neighbour by 9 km in the along-track direction.

Figures 5.7-5.14 show details of co-registration at the surface (SRF), at the highest reflecting layer (HRL), and by Maximum Similarity (MXS) for parts of the track. Figures 5.7, 5.9, 5.11, and 5.13 show results of co-registration as well as cross-sections of relative differences in cloud extinction

$$\delta\alpha_{\text{ext}} = \frac{(\alpha_{\text{ext}}^{\text{perturbed}} - \alpha_{\text{ext}}^{\text{control}})}{\alpha_{\text{ext}}^{\text{control}}} \tag{5.15}$$

between *perturbed* and *control* experiments. Of course, in the EarthCARE mission actual extinction, $\alpha_{\text{ext}}^{\text{control}}$, is unknown and the goal is to retrieve $\alpha_{\text{ext}}^{\text{perturbed}}$. Coloured points show each domain's reference level. As outlined in section 5.3.2, the SRF and HRL co-registration methods choose simulated and measured TOA radiances for forward and backward views that intersect a particular reference level. In order to illustrate the choice made the MXS method, equivalent reference levels were determined in the panels of the figures denoted by MXS.

If at least one of the three attributed TOA radiance pairs differed by more than $10/\pi$ W m^{-2} sr^{-1} (where 10 W m^{-2} is EarthCARE's goal), the reference level was coloured magenta; otherwise it was coloured green. Dashed lines illustrate lines-of-sight of co-registered TOA radiances, for two sample domains in Figure 5.7. As one may notice, oblique lines-of-sight were symmetric around the nadir line-of-sight for SRF and HRL, but not in MXS co-registration. This is because MXS co-registration selects independent subsets of forward and backward radiances.

Corresponding to Figs. 5.7, 5.9, 5.11, and 5.13, Figs. 5.8, 5.10, 5.12, and 5.14 present the co-registered differences between TOA radiances of *control* of *perturbed* experiment, collectively for all three viewing angles. From top to bottom, the panels show results for SRF, HRL, and MXS co-registration. Again, a grey shaded area highlights differences of up to $10/\pi$ W m^{-2} sr^{-1}. Over SRF, HRL, and MXS co-registration the nadir TOA radiance differences remained unchanged, but forward and backward differences shifted due to a changing attribution by co-registration

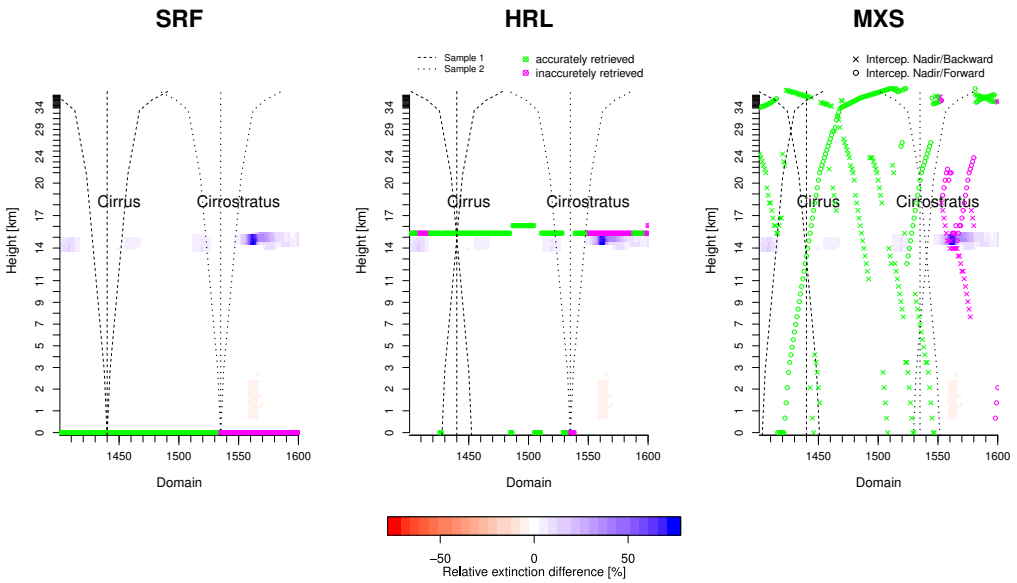

Fig. 5.7: Co-registration at the surface (SRF), the highest reflecting layer (HRL), and by Maximum Similarity (MXS) for a region containing Cirrus and Cirrostratus clouds. Highlighted in magenta and green are intersections for nadir with off-nadir lines-of-sight, as shown for two samples. For SRF and HRL, intersections correspond to single reference levels, i.e. surface and highest reflecting layer, for most parts forming a horizontal layer. For MXS, equivalent reference levels are provided separately for forward and backward view. More details are given in section 5.6. Relative extinction differences are between the *control* and *perturbed* experiments, and range roughly between -10% to 75% for this region.

methods. Consequently, a changing attribution of oblique radiances to domains led to more or less overlap of forward, nadir, and backward TOA radiance differences. The higher the degree of overlap and the more agreement in shape of the lines, the more we managed to attribute off-nadir radiances, which show a similar difference to their perturbed counterpart as the radiances in the nadir view do; and the higher the performance in identification of inaccurately retrieved domains, which are listed separately on the plots.

First, three regions were analyzed in order to understand the effectiveness of co-registration methods when Cirrus, and broken, clouds are present.

As shown in figure 5.7, $\delta\alpha_{\text{ext}}$ were smaller for Cirrus and larger for Cirrostratus clouds. Accordingly, exceeding of the radiance difference threshold took predominately place in latter domains. Focusing on the horizontal extend of the magenta-coloured reference levels, the spread at SRF (section 1530-1600) went beyond domains of larger $\delta\alpha_{\text{ext}}$ (section 1550-1580). In contrast, HRL and MXS co-registration managed to narrow down this spread. Figure 5.8 shows the improved overlap for HRL and MXS over SRF co-registration. As sample 1 and 2 in Fig. 5.7 indicate, HRL and MXS co-registration chose oblique TOA radiances for each domain individually.

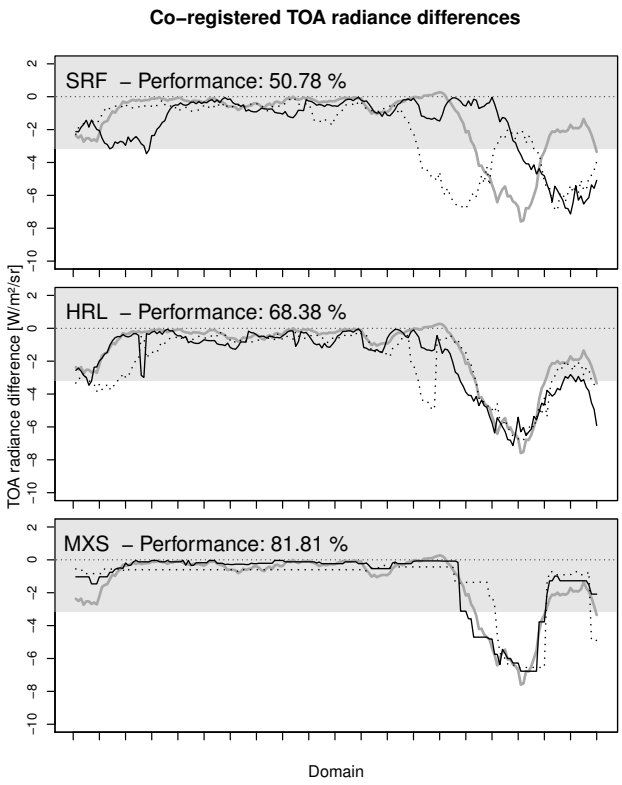

Fig. 5.8: Co-registered TOA radiance differences between *control* and *perturbed* experiments for all three viewing angles along with the performance for the three co-registration methods: (SRF) at the surface; (HRL) at the highest reflecting layer, and (MXS) by Maximum Similarity. The threshold refers to EarthCARE's radiative flux threshold, divided by π.

Hence, both co-registration methods were able to select similarly affected radiances for all viewing angles which intersected the same *perturbed* area.

A cloud-free region (around section 1530-1540) in between cloudy domains received large TOA radiance differences for SRF and HRL co-registration. The surface of the cloud-free domains were partly invisible to the backward view. In other words, the backward line-of-sight pointing at the surface of the cloud-free domains intersected neighbouring Cirrostratus clouds whose properties differed from those of clouds in the domain being assessed. Contrary to HRL co-registration, 3D photon paths provide information about the 3D cloud structure. Figure 5.8 confirms the difference between HRL and MXS co-registration for these domains in the backward view. Consequently, MXS co-registration selected a line-of-sight in the backward view which pointed at a surface close-by without intersecting critical clouds and attributed the corresponding backward TOA radiance differences to the cloud-free domains. Overall, MXS co-registration (81.81%) performed better than HRL (68.38%) and SRF (50.78%).

Figure 5.9 presents a Cirrus cloud edge with large $\delta\alpha_{\text{ext}}$. The right half of the region consisted largely of an unperturbed, lower cloud structure. Ideally, domains containing *perturbed* Cirrus clouds were attributed with larger TOA radiance differences and labelled as inaccurately retrieved. For SRF co-registration, we found again a much broader region of inaccurately retrieved domains than *perturbed* ones (section 3600-3745). Co-registering at HRL, domains identified with inaccurate retrievals were less extensive (section 3600-3730). However, around domain 3740, unperturbed domains were still marked as inaccurately retrieved. Using MXS co-registration, only *perturbed* domains were correctly identified as inaccurately retrieved.

Figure 5.10 confirms that the big difference between SRF and both HRL and MXS co-registration where the latter had approximately +40% more correct identifications. The poorly co-registered cloud edge (section 3740-3750) is, however, clearly visible in the HRL derived forward view.

Figure 5.11 shows a Cirrus cloud with $\delta\alpha_{\text{ext}}$ as large as 25%. At lower altitudes, cloud structures with smaller $\delta\alpha_{\text{ext}}$ were present. Considering the cloud top height in HRL in contrast to SRF co-registration, led to an enhanced separation of accurate and inaccurate retrievals in the left half of the region. The knowledge about multiple reflecting layers, for MXS co-registration, resulted in an even finer separation. Figure 5.12 underlines the difference between MXS and HRL co-registration with MXS resulting in an improvement of 9% in identification performance.

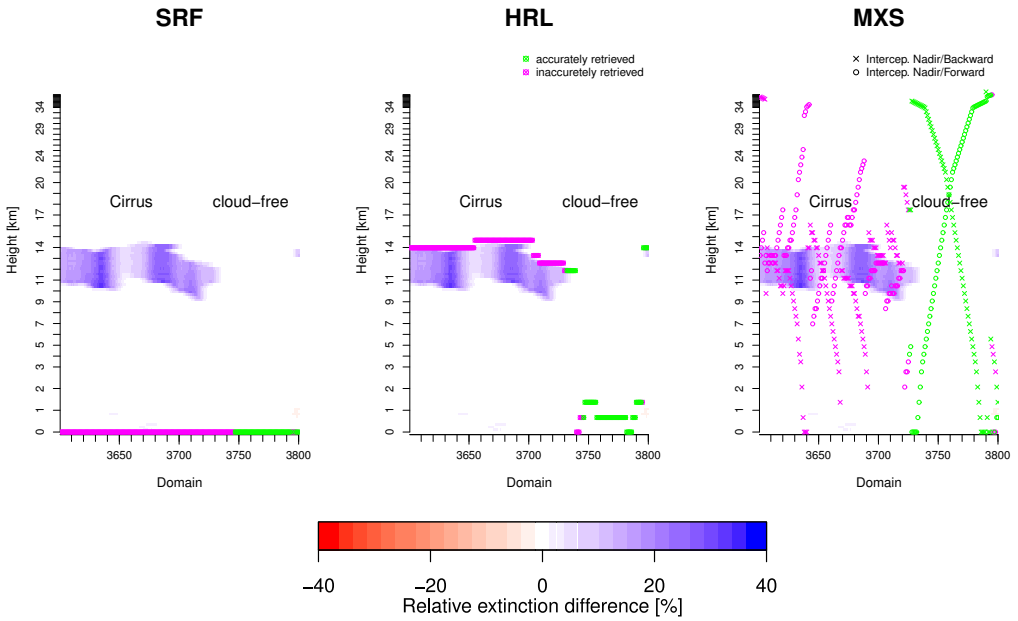

Fig. 5.9: Same as Fig. 5.7 but this is for the edge of a Cirrus cloud that exhibited large differences between the *control* and *perturbed* simulations (between -5% and 35%).

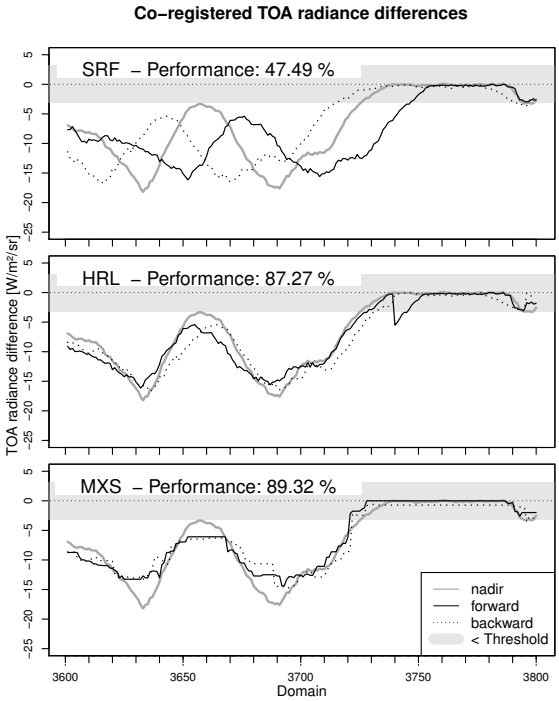

Fig. 5.10: Same as Fig. 5.8 but applicable to Fig. 5.9.

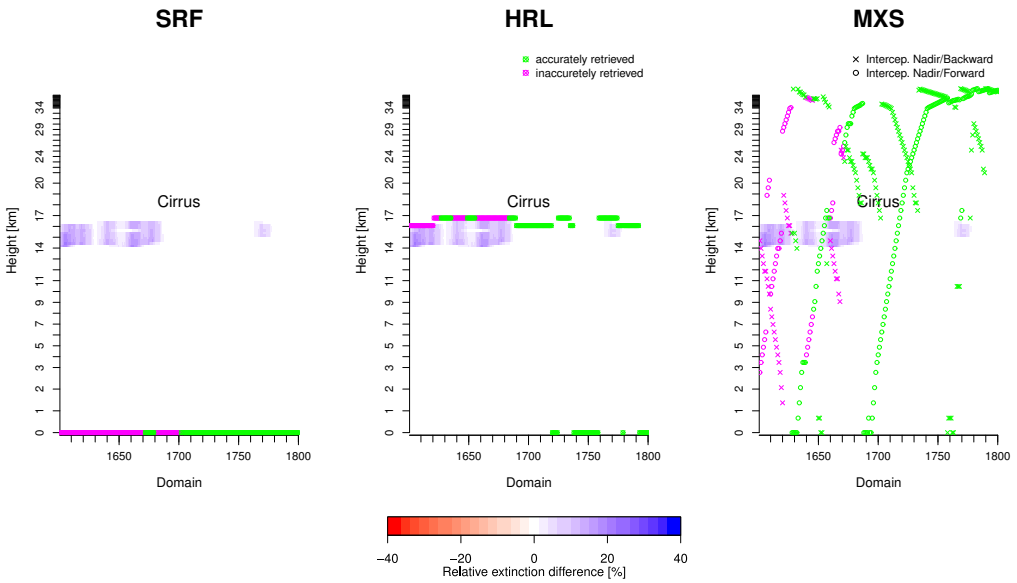

Fig. 5.11: Same as Fig. 5.7 but for Cirrus clouds above low-level clouds. Relative extinction differences range roughly between -1% and 25%.

Thus, based on the three regions looked at here, which are fairly representative of demanding conditions in general, it seems safe to conclude that having the additional information from the Monte Carlo simulations results in improved identification of inaccurate retrievals.

In addition, Table 5.1 presents identification performances of co-registration methods for some specific cloud types along the track. Echoing the results presented above: MXS co-registration is superior to other methods for Cirrus clouds, identifying $+4\%$ more inaccurate retrievals, and cloud-free domains (mostly part of broken cloud fields, cp. Fig. 5.5) for which it identified $+15\%$ more inaccurate retrievals.

While there was little difference in identification performance among co-registration methods for Cumulus clouds, the few domains that contained Deep Convective clouds saw the MXS method slightly less successful at identified inaccurate retrievals (-3%).

A potential pitfall to relying on information gleaned from simulated radiances is that *perturbed* cloud properties - that is, inaccurate retrievals - alter distributions of photon paths relative to true distributions. This might negatively impact the MXS co-registration selection process of oblique TOA radiance differences. As a result, the ability of MXS co-registration to identify inaccurate retrievals could decrease.

An example for limited performance of MXS co-registration is shown in Fig. 5.13. $\delta\alpha_{\text{ext}}$ were large, up to 80%, over the region of Deep Convective clouds. Consequently, extracted photon paths acted on stronger *perturbed* cloud properties, and

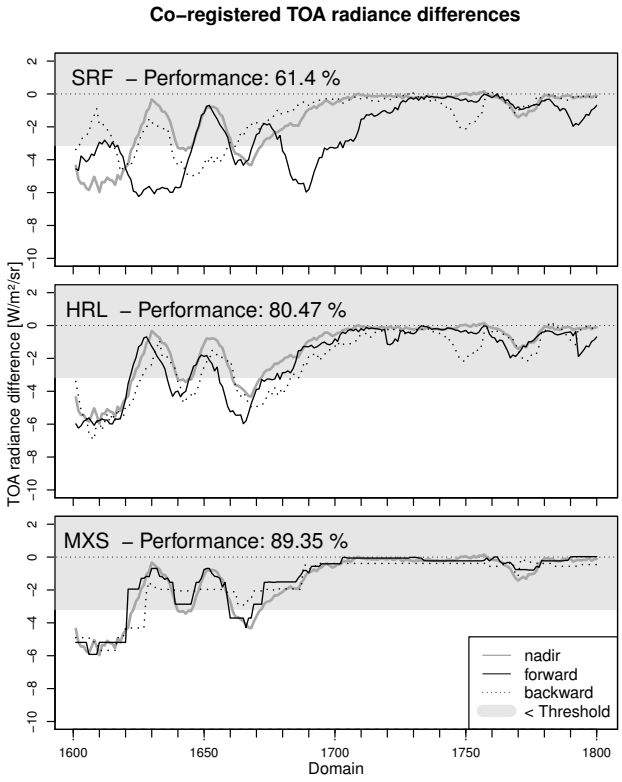

Fig. 5.12: Same as Fig. 5.8 but applicable to Fig. 5.11.

Tab. 5.1: Performance values for all regions along the cross-section shown in Fig. 5.5 and additionally for specific cloud/scene types. Comparing co-registration at the surface (SRF), the highest reflecting layer (HRL) or via Maximum Similarity (MXS), bold-face values indicate the co-registration method with the best performance for selected domains.

Domain No.	Characteristics	P(SRF) [%]	P(HRL) [%]	P(MXS) [%]
1400-1600	Cirrus and Cirrostratus Clouds	50.78	68.38	**81.81**
1600-1800	Cirrus Clouds	61.4	80.47	**89.35**
2800-3000	Deep Convective Clouds (horizontally heterogeneous)	49.62	90.23	**92.04**
3000-3200	Deep Convective Clouds (horizontally homogeneous)	36.14	**82.10**	78.17
3600-3800	Cirrus Clouds and cloud-free zones	47.49	87.27	**89.32**
1052/5000	Only domains with Cumulus Clouds	84.37	**85.75**	85.27
1933/5000	Only domains with Cirrus Clouds	71.94	87.38	**91.98**
181/5000	Only domains with Deep Convective Clouds	75.52	**93.12**	89.98
1286/5000	Only cloud-free domains	0.45	0.45	**15.01**

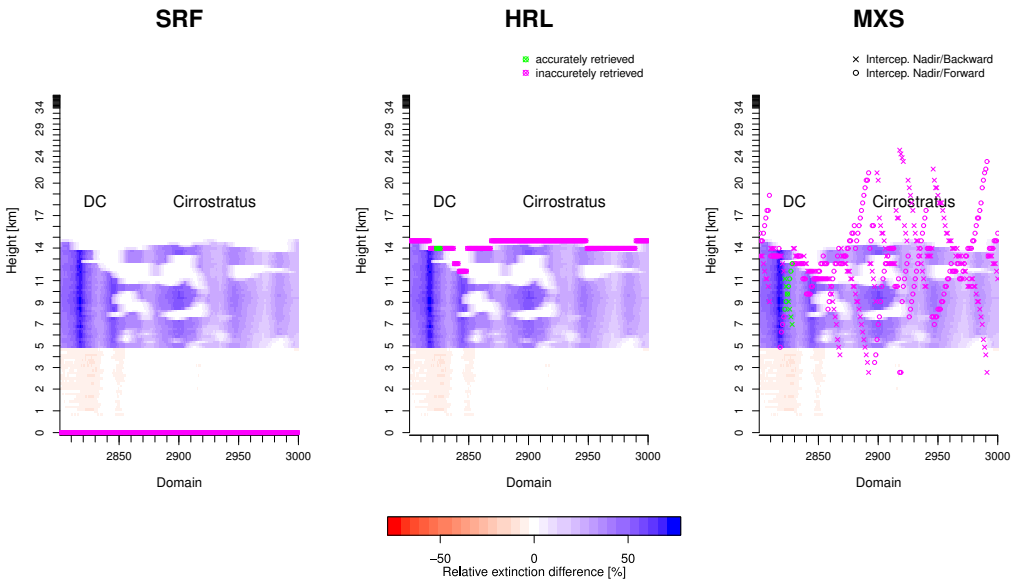

Fig. 5.13: Same as Fig. 5.7 but for deep convective and Cirrostratus clouds with relative extinction differences between -10% and 75%.

were, potentially, less reliable. As Fig. 5.14 shows, applying MXS (92.04%) over HRL co-registration (90.23%) was less profitable.

For HRL and MXS co-registration, TOA radiance differences below $10/\pi$ W m^{-2} sr^{-1} were concurrently attributed to domains of low $\delta\alpha_{\text{ext}}$ (section 2820-2830), although located in the midst of domains containing larger $\delta\alpha_{\text{ext}}$. Observing the total extinction of the domains marked in green, we found they were characterized by a strongly reflecting cloud top layer, in contrast to more transparent clouds nearby (outside of 2820-2830). Clear, when extinction is weak near cloud top, underlying reflecting layers can contribute much to TOA radiances. If retrieved inaccurately, the layers below cloud top provide inconsistent backscattered radiation and lead to an exceeding of the threshold as photon paths might not resemble their real counterparts particularly well. Accordingly, the selection process by MXS co-registration can be affected adversely.

It might also be that horizontally heterogeneous domains, as seen in Fig. 5.13, were assumed to support the individuality of photon paths. A large variety of atmospheric paths would provide a small set of suitable paths and, hence, prevent MXS co-registration from selecting a path, which only appeared similar due to inaccurate retrieval. In addition to the heterogeneous region, we applied co-registration algorithms to a horizontally homogeneous and largely inaccurately retrieved region (section 3000-3200). As a result, we observed a lower performance for MXS than HRL co-registration.

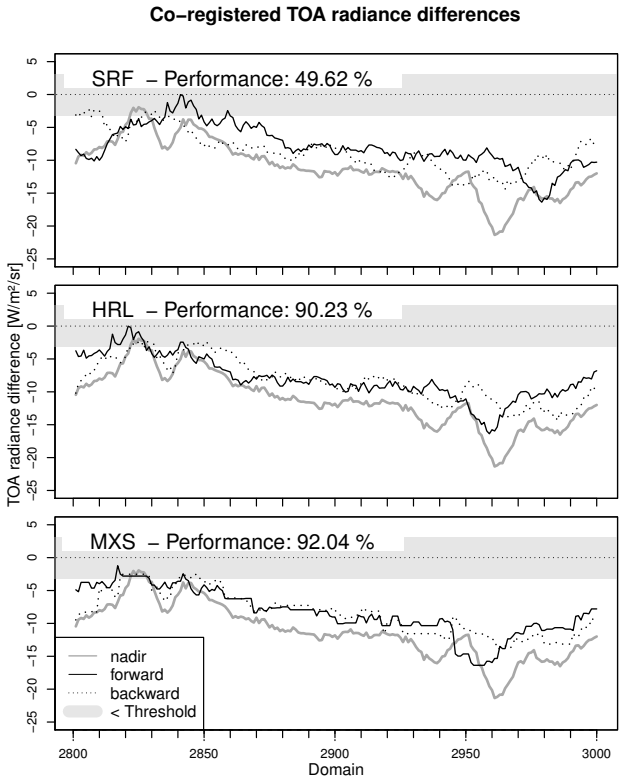

Fig. 5.14: Same as Fig. 5.8 but applicable to Fig. 5.13.

In summary, we show how 3D photon paths, extracted from 3D MC simulations, support radiance co-registration in the presence of Cirrus and broken cloud fields. As summed up in table 5.1, we still found advantages of MXS co-registration over other co-registration methods for large-scale inaccuracies of cloud parameters. Only in the special case of horizontal homogeneity and inaccurate retrieval on a larger scale, we expect accidentally high similarities between nadir and oblique MC photon paths resulting in mistaken selection by MXS co-registration.

5.7 Summary and Conclusion

EarthCARE will retrieve vertical profiles of cloud and aerosol properties by combining data from active and passive instruments. In order to check the verisimilitude of the retrieved properties, a radiative closure assessment is foreseen (see Illingworth et al., 2015; Barker et al., 2014a) in which EarthCARE's BBR radiances, measured at three viewing angles, will be compared to modelled radiances simulated by 1D and 3D radiative transfer models. Differences between measured and simulated radiances and fluxes will hopefully help retrieval algorithm developers and users understand the performance characteristics of the algorithms and their retrieved products.

After broadening the retrieved cross-section across-track, it will be operated on by radiative transfer models with simulated and measured radiances partitioned into 3D domains of $(10\text{km})^2$ area. As the attenuators in each domain will generally scatter shortwave (SW) radiation at different heights, it is not obvious how best to select the oblique TOA radiances that align most with nadir radiances so as to optimize the quality of the comparison between measured and modelled radiances. This problem of co-registering radiances for the purpose of performing a closure experiment was the main point of this study.

In contrast to previous co-registration methods, such as the highest reflecting layer (HRL) of a domain, photon path information, produced by application of a 3D MC model to the retrieved atmosphere, was employed. The intention is to use this information for situations in which the assumption of a single reflecting layer is inadequate, such as for semi-transparent or broken cloud fields.

In this study, we used a 5000 km-long track of A-train satellite data. Application of a MC SW model using A-train-derived cloud and aerosol properties provided a *control* experiment consisting of BBR-like radiances. These radiances were meant to represent EarthCARE BBR observations. A second *perturbed* experiment, with randomly altered cloud profiles that mimic imperfect retrieval of cloud properties, yielded corresponding radiances that are to be compared to *control* values in order

to assess the quality of the retrievals (which in this idealized setting are represented by the randomly altered A-train retrievals). Additionally, the *perturbed* simulations output 3D photon path information as needed by the new radiance co-registration method.

By using a performance measure for identification of inaccurate retrievals, it was shown that the Maximum Similarity (MXS) co-registration method, using 3D MC photon paths, successfully supported radiance co-registration and outperformed previous 2D-based methods, for most parts of the track, such as co-registration at the HRL and the surface (SRF). As expected, the largest improvements were for Cirrus clouds and broken cloud fields. This was especially so in the tropics where convective cloud structure can be very inhomogeneous, and in mid-latitudes where semi-transparent cirrus clouds can partially obscure lower clouds. In these cases the HRL method does not always represent the optimal intersection of the three BBR lines-of-sight as potentially important reflecting layers below the HRL go unacknowledged.

In special cases, i.e. for inaccurate retrieval on a large scale over a horizontally homogeneous atmosphere, we suspected perturbations to affect photon paths, such that their information content may become misleading for co-registration purposes. In contrast to an uncertain HRL, simulated radiances and photon paths are products of the same source. Naturally, an ideal MC model acting on fairly well-retrieved parameters is expected to establish both more realistic radiances and photon paths; and vise versa. We suggest future experiments on reduced and enhanced degrees of perturbation, to know where the limits of photon path reliability are.

The tests performed here idealized the radiative closure assessment by only perturbing cloud properties. EarthCARE will also face uncertainties in surface and aerosol properties, especially over land. Further experiments will have to include errors in the specification of surface and aerosol optical properties (cf. Barker et al., 2014b) and more realistic errors and uncertainties in cloud retrievals. Ultimately, this will require full end-to-end simulations of EarthCARE's processes.

Finally, this novel co-registration approach might also benefit Angular distribution models (ADMs), converting single- or multi-angular TOA radiances into TOA radiative fluxes. Relying on radiances originating from different scene types, MXS could ensure that off-nadir radiances point at a scene type of interest. Consequently, we see a large potential in MC photon paths to improve ADM's radiance to flux conversion.

Acknowledgements

We thank ESA for financial support within the FLURB project (4000104526/11/NL/CT), EOAS of the University of British Columbia for computing time and the McMaster University of Hamilton as well as the Institute for Space Science at the Freie Universität Berlin for providing work space. The latter institution, led by Professor Dr. Jürgen Fischer, provided steady motivation through its fruitful seminars. Monte Carlo simulations were performed on the facilities of the Shared Hierarchical Academic Research Computing Network (SHARCNET: [http://www.sharcnet.ca).

6 Conclusion

This work contributes in various ways to the estimation of top-of-atmosphere (TOA) shortwave (SW) and longwave (LW) fluxes and their uncertainties, which are based on BBR radiance measurements onboard the upcoming EarthCARE mission.

We assess a so-far unaccounted sampling uncertainty of BBR-measured SW and totalwave (TW) radiances assembled towards $\sim$100 km^2 assessment domains. Uncertainties arise from irregular sampling through $\sim$(0.6)km^2 footprints within domains and a naturally heterogeneous radiance field. Sampling becomes increasingly irregular as BBR instrument performance is reduced to conserve mission lifetime. We evaluate uncertainties using Landsat 8 imagery and repeated mimicry of BBR nadir sampling under various levels of instrument performance, and measure how far BBR-obtained radiances depart from actual mean radiances over domains. We observe that uncertainty in SW and TW radiances increases linearly with radiance heterogeneity and near-linearly with reduced instrument performance. We find that the uncertainty of LW radiances, which are inferred from staggered SW and TW measurements, is particularly sensitive to instrument performance and can amount to twice the SW uncertainty – even though LW radiances are horizontally homogeneous within domains. In order to keep radiance uncertainties below a flux equivalent of 10 W m^{-2}, we recommend to reduce instrument performance no further than 25% of its nominal value.

We present an algorithm for the conversion of BBR-measured TOA SW radiances into TOA SW fluxes over clear-sky domains. We find a new representation of state-of-the-art CERES angular distribution models (ADMs). Through the use of additional geophysical variables - obtained from an aerosol optical depth climatology, ERA-20C reanalysis, and climatology of MCD43BGF surface bidirectional reflectance distribution function parameters - we unite spatially and temporally separate CERES ADMs towards new ADMs per surface type and BBR-perceived scattering direction. We show which geophysical parameters are important and how well artificial neural networks perform when using essential parameters. With the exception of domains containing fresh snow, we reproduce CERES estimates with an uncertainty of 2.7 – 4.0 W m^{-2}. Fresh snow surfaces are hardly characterized by any of above parameters and that results in larger uncertainties of 8.3 – 14.6 W m^{-2}.

We investigate whether the conversion of BBR-measured TOA SW radiances to fluxes above low-levels clouds is significantly sensitive to cloud microphysics and cloud-topped moisture. We generate new ADMs that account for cloud-top effective radii and cloud-topped water vapor by using CERES-MODIS observations and broadband simulations. We find that TOA SW anisotropy can vary by 2.9-8.0% due to extremes in cloud-top effective radii, and by 1.3-6.4% due to extremes in cloud-topped water vapor, while anisotropy uncertainty is 3.2-5.0%. Compared to state-of-the-art CERES ADMs, which lack these sensitivities, new radiance-to-flux conversions show differences of up 20 W m^{-2} – especially for particularly small and large cloud-top effective radii (5 and $20\,\mu$m, corresponding to particularly strong and weak cloud-aerosol interaction, respectively). When applying ADMs to CERES cross-track measurements, which produce radiation budget estimates as a benchmark for global climate models, new ADMs produce TOA SW flux estimates 1-2 W m^{-2} larger than CERES ADMs. We can attribute such flux biases in part to conditions of persistently small effective radii and low amounts of cloud-topped water vapor. This work therefore identifies additional factors impacting TOA SW anisotropy that future radiance-to-flux converting ADMs should consider to avoid sampling biases.

We introduce a new method of colocating individual measurements of SW radiances and corresponding flux estimates from BBR's three views towards a common assessment domain. By using photon paths, produced by 3D Monte-Carlo radiative transfer simulations acting on active-passive retrievals of a cloudy atmosphere, we are able to colocate even under conditions of broken and semitransparent clouds where no obvious vertical level exists that current methods would use for colocation. Applied to a 5000 km frame based on A-Train satellite observations, we find that the use of photon paths improves colocation by 4% for cirrus clouds and 15% for broken cloud fields when compared against a colocation at cloud-top height level.

Once the EarthCARE mission is launched, the radiative closure assessment will compare BBR-based TOA flux estimates with simulated TOA fluxes, based on 1D or 3D radiative transfer simulations acting on active-passive retrievals of clouds and aerosols. By providing a better understanding of BBR-based TOA fluxes and their uncertainties, this work will improve the mission's radiative closure assessment which will strengthen the science community's understanding of the interaction among clouds, aerosols, and radiation.

7 Zusammenfassung

Die vorliegende Arbeit leistet verschiedene Beiträge zur messgestützten Schätzung von Strahlungsflüssen am Oberrand der Atmosphäre sowie deren Unsicherheiten. Die Schätzungen basieren auf Strahldichtemessungen des BBR an Bord der geplanten Satellitenmission EarthCARE.

Wir untersuchen die Unsicherheiten von BBR-gemessenen Strahldichten im Nadir über $\sim$100km^2 großen Gebieten. Mögliche Unsicherheiten kommen durch die ungleichmäßige Erfassung $\sim$(0.6km)^2 großer Ausleuchtbereiche innerhalb eines Gebietes die natürliche horizontale Heterogenität des Strahlungsfeldes zustande. Ein gezieltes Herunterregeln der BBR-Leistung ermöglicht eine Verlängerung der Lebensdauer der Mission, resultiert allerdings in zunehmend ungleichmäßiger Erfassung der Strahlungsfeldes. Für diese Arbeit werden die Unsicherheiten durch Simulation verschiedener BBR-Leistungslevel an räumlich hochaufgelösten Landat-8-Messungen abgeschätzt. Die Ergebnisse zeigen, inwieweit BBR-basierte Strahldichten von eigentlichen Gebietsmitteln abweichen. Unsicherheiten kurzwelliger und totalwelliger (kurzwelliger plus langwelliger) Strahldichten nehmen linear mit der horizontalen Heterogenität des jeweiligen Strahlungsfeldes innerhalb der Gebiete zu und steigen nahezu linear mit reduzierter Leistung an. Wir zeigen weiterhin, dass langwellige Strahldichten, die von räumlich versetzten kurz- und totalwelligen Messungen abgeleitet werden, eine deutlich höhere Sensitivität gegenüber der BBR-Leistung aufweisen. Es zeigt sich eine Verdopplung der Unsicherheit von langwelligen gegenüber kurzwelligen Strahldichten, sogar wenn Gebiets-interne langwellige Strahlungsfelder horizontal homogen sind. Um eine Unsicherheit resultierender Strahlungsflüsse von unter 10 W m^{-2} zu gewährleisten, empfehlen wir die Leistung um nicht mehr als 25% vom nominellen Wert zu reduzieren.

Wir präsentieren einen Algorithmus zur Umwandlung von solaren Strahldichten in solare Strahlungsflüsse am Oberrand der Atmosphäre über wolkenfreien Gebieten. Wir zeigen eine neue Abbildung gängiger CERES Winkelverteilungsmodelle. Durch kollokierte geophysikalische Parameter (einer Klimatologie Aerosol-optischer Dicken, ERA-20C Reanalyse-Daten, sowie einer Klimatologie von MCD43BGF-basierten Parametern für bidirektionale Reflexionsverteilungsfunktionen über Landoberflächen) können räumlich und zeitlich separate CERES Modelle vereint werden, und neue Winkelverteilungsmodelle per Landoberflächenklasse und per BBR-erfassbarer Streurichtung erzeugt werden. Es wird dargestellt, welche geophysikalischen Parameter für

die Erzeugung relevant sind und mit welcher Genauigkeit CERES Modelle reproduziert werden. Neue Modelle weichen um 2.7-4.0 W m^{-2} von CERES Modellen ab, wenn Fälle mit Neuschneeereignissen ausgeschlossen werden. Neuschnee und dessen bidirektionale Reflexionsverteilung wird durch geophysikalische Parameter nicht erfasst. In diesen Fällen beträgt die Abweichung 8.3-14.6 W m^{-2}.

Wir untersuchen die Umwandlung von gemessenen solaren Strahldichten in solare Strahlungsflüsse am Oberrand der Atmosphäre über tiefen Flüssigwasserwolken. Es wird die Sensitivität gegenüber der Wolkentröpfchengrößenverteilung und der Wasserdampfmenge über Wolken analysiert, die herkömmliche CERES Winkelverteilungsmodelle nicht berücksichtigen. Mit Hilfe mehrjähriger CERES-MODIS Messungen sowie Breitband-Simulationen mit dem Strahlungstransfermodell MOMO, erstellen wir neue Winkelverteilungsmodelle, die eine Sensitivität gegenüber Wolkenoberkanten-Effektivradius und Wasserdampfsäule über den Wolken zulassen. Die Ergebnisse beschreiben eine Variabilität der solaren Anisotropie von 2.9-8.0% zwischen extremen Effektivradien sowie 1.3-6.4% zwischen extremen Wasserdampfsäulengehalten. Die Unsicherheit der Anisotropie beträgt 3.2-5.0%. Im Vergleich zu CERES Winkelverteilungsmodellen weichen Strahlungsflussschätzungen um bis 20 W m^{-2} ab. Insbesondere bei sehr kleinen und großen Effektivradien (5 und $20\,\mu$m, entsprechend einer sehr starken und schwachen Wolken-Aerosol-Interaktion, respektive) wird eine große Abweichung beobachtet. Bei der Anwendung auf CERES Cross-Track Messungen, die als Grundlage zur Validierung von Klimamodellen dienen, schätzen die neu beschriebenen Winkelverteilungsmodelle 1-2 W m^{-2} höhere solare Strahlungsflüsse als CERES Modelle. Teilweise kann diese Differenz bestimmten Regionen zugeordnet werden, die stets kleine Wolken-Effektivradien und niedrige Mengen Wolken-überlagerten Wasserdampfs ausweisen. Diese Arbeit identifiziert somit zusätzliche Anisotropie-Faktoren, die zukünftige Winkelverteilungsmodelle berücksichtigen sollten, um regionale, systematische Fehler in Strahlungsflussschätzungen zu vermeiden.

Wir stellen eine neue Methode zur Kollokation von individuellen Strahldichtemessungen der drei BBR-Beobachtungsrichtungen sowie zugehörigen Strahlungsflussschätzungen zu gemeinsamen Gebieten vor. 3D Monte-Carlo Strahlungstransfersimulationen, die auf eine aktiv-passiv gemessene Atmosphäre angewendet werden, generieren Photonenpfade pro BBR-Messung. Die simulierten Photonenpfade erlauben eine Kollokation auch unter schwierigen Bedingungen, wie z.B. teilweiser oder semi-transparenter Bewölkung, an denen herkömmliche Methoden scheitern. Angewendet auf eine 5000 km lange Szene aus Satellitendaten des A-Trains, beobachten wir eine Verbesserung der Kollokation von 4% bei Zirrusbewölkung und 15% für Fälle teilweiser Bewölkung, verglichen mit einer Methode, die die Wolkenoberkantenhöhe zur Kollokation nutzt.

Mit dem anstehenden Start der EarthCARE Mission wird das Strahlungsschließungsexperiment BBR-basierte und simulierter Strahlungsflüsse am Oberrand der Atmosphäre vergleichen. Durch neu gewonnene Erkenntnisse hinsichtlich BBR-gestützter Strahlungsflüsse und deren Unsicherheiten trägt diese Arbeit zum besseren Verständnis über die Wechselwirkung von Wolken, Aerosolen und Strahlung innerhalb der Wissenschaftsgemeinschaft bei.

Bibliography

Ardanuy, P. E., L. L. Stowe, A. Gruber, and M. Weiss (1991). "Shortwave, longwave, and net cloud-radiative forcing as determined from Nimbus 7 observations". In: *Journal of Geophysical Research: Atmospheres* 96.D10, pp. 18537–18549. DOI: 10.1029/91JD01992 (cit. on p. 2).

Barker, H. W. and J. A. Davies (1992). "Solar Radiative Fluxes for Stochastic, Scale-invariant Broken Cloud Fields". In: *J. Atmos. Sci.,* 49.13, pp. 1115–1126 (cit. on p. 82).

Barker, H. W., B. A. Wiellicki, and L. Parker (1996). "A Parameterization for Computing Grid-Averaged Solar Fluxes for Inhomogeneous Marine Boundary Layer Clouds. Part II: Validation Using Satellite Data". In: *Journal of the Atmospheric Sciences* 53.16, pp. 2304–2316. DOI: 10.1175/1520-0469(1996)053<2304:APFCGA>2.0.CO;2 (cit. on pp. 1, 49).

Barker, H. W., R. K. Goldstein, and D. E. Stevens (2003). "Monte Carlo Simulation of Solar Reflectances for Cloudy Atmospheres". In: *Journal of the Atmospheric Sciences* 60.16, pp. 1881–1894 (cit. on p. 74).

Barker, H. W., M. P. Jerg, T. Wehr, et al. (2011). "A 3D cloud-construction algorithm for the EarthCARE satelitte mission". In: *Quarterly Journal of the Royal Meteorological Society* 137.657, pp. 1042–1058. DOI: 10.1002/qj.824 (cit. on pp. 2, 23, 70, 82).

Barker, H. W., S. Kato, and T. Wehr (2012). "Compuation of Solar Radiative Fluxes by 1D and 3D Methods Using Cloudy Atmospheres Inferred from A-train Satellite Data". In: *Surveys in Geophysics* 33.3-4, pp. 657–676. DOI: 10.1007/s10712-011-9164-9 (cit. on pp. 70, 82).

Barker, H. W., J. N. S. Cole, C. Domenech, et al. (2014a). "Assessing the quality of active–passive satellite retrievals using broad-band radiances". In: *Quarterly Journal of the Royal Meteorological Society*. DOI: 10.1002/qj.2438 (cit. on pp. 9, 71, 72, 75, 93).

Barker, H. W., J. N. S. Cole, and M. W. Shephard (2014b). "Estimation of Errors associated with the EarthCARE 3D Scene Construction Algorithm". In: *Quarterly Journal of the Royal Meteorological Society*. DOI: 10.1002/qj.2294 (cit. on pp. 70, 82, 94).

Barker, H. W., Z. Qu, S. Bélair, et al. (2017). "Scaling properties of observed and simulated satellite visible radiances". In: *Journal of Geophysical Research: Atmospheres* 122.17, pp. 9413–9429. DOI: 10.1002/2017JD027146 (cit. on p. 7).

Bertrand, C., N. Clerbaux, A. Ipe, S. Dewitte, and L. Gonzalez (2005). "Angular distribution models, anisotropic correction factors, and mixed clear-scene types: a sensitivity study". In: *IEEE Transactions on Geoscience and Remote Sensing* 43.1, pp. 92–102. DOI: 10.1109/TGRS.2004.838361 (cit. on p. 38).

Bloom, S., A. da Silva, and D. Dee (2005). *Documentation and validation of the Goddard Earth Observing System (GEOS) Data Assimilation System*. Tech. rep. TM-2005-104606. Version 4. NASA (cit. on p. 50).

Bolton, David (1980). "The Computation of Equivalent Potential Temperature". In: *Monthly Weather Review* 108.7, pp. 1046–1053. DOI: 10.1175/1520-0493(1980)108<1046:TCOEPT>2.0.CO;2 (cit. on p. 50).

Boucher, O., D. Randall, P. Artaxo, et al. (2013). "Clouds and Aerosols". In: *Climate Change 2013: The Physical Science Basis. Contribution of Working Group I to the Fifth Assessment Report of the Intergovernmental Panel on Climate Change*. Ed. by T.F. Stocker, D. Qin, G.-K. Plattner, et al. Cambridge, United Kingdom and New York, NY, USA: Cambridge University Press. Chap. 7, pp. 571–658. DOI: 10.1017/CBO9781107415324.016 (cit. on pp. 1, 69).

Breiman, L. (2001). "Random Forests". In: *Machine Learning* 45.1, pp. 5–32. DOI: 10.1023/A:1010933404324 (cit. on p. 27).

Brenguier, J.-L., H. Pawlowska, L. Schüller, et al. (2000). "Radiative Properties of Boundary Layer Clouds: Droplet Effective Radius versus Number Concentration". In: *Journal of the Atmospheric Sciences* 57.6, pp. 803–821. DOI: 10.1175/1520-0469(2000)057<0803:RPOBLC>2.0.CO;2 (cit. on p. 50).

Caldwell, M. E., D. A. V. Spilling, J. Delderfield, K. Ward, and M. Whalley (2017a). "Radiometric Characteristics of the Broadband Radiometer (BBR) Instrument for the EarthCARE Mission". In: *Journal of Atmospheric and Oceanic Technology* 34, pp. 1783–1794. DOI: 10.1175/JTECH-D-16-0168.1 (cit. on p. 8).

Caldwell, M. E., D. Spilling, W. Grainger, et al. (2017b). "The EarthCARE mission BBR instrument: ground testing of radiometric performance". In: *Proc.SPIE* 10402, pp. 10402 –10402 –14. DOI: 10.1117/12.2273148 (cit. on pp. 7, 23).

Capderou, M. and M. Viollier (2006). "True Along-Track Scan to Improve Radiation Budget Estimations". In: *Journal of Atmospheric and Oceanic Technology* 23.8, pp. 1093–1103. DOI: 10.1175/JTECH1907.1 (cit. on p. 30).

Cole, J., H. W. Barker, N. G. Loeb, and K. von Salzen (2011). "Assessing Simulated Clouds and Radiative Fluxes Using Properties of Clouds Whose Tops are Exposed to Space". In: *J. Climate* 24.11, pp. 2715–2727. DOI: 10.1175/2011JCLI3652.1 (cit. on p. 69).

Corbett, J. and W. Su (2015). "Accounting for the effects of sastrugi in the CERES clear-sky Antarctic shortwave angular distribution models". In: *Atmospheric Measurement Techniques* 8.8, pp. 3163–3175. DOI: 10.5194/amt-8-3163-2015 (cit. on p. 34).

Cox, C. and W. Munk (1954). "Measurement of the Roughness of the Sea Surface from Photographs of the Sun's Glitter". In: *J. Opt. Soc. Am.* 44.11, pp. 838–850. DOI: 10.1364/JOSA.44.000838 (cit. on p. 27).

– (1956). "Slopes of the sea surface deduced from photographs of sun glitter". In: *Bulletin of the Scripps Institution of Oceanography* 6.9, pp. 401–488 (cit. on p. 82).

Deepak, A. and H. E. Gerbers, eds. (1983). *Report of the experts' meeting on aerosols and their climatic effects*. WCP-55 World Climate Research Program, Geneva (cit. on p. 82).

Delanoë, J. and R. J. Hogan (2010). "Combined CloudSat-CALIPSO-MODIS retrievals of the properties of ice clouds". In: *J. Geophys. Res.* 105.D00H29, pp. 1–17. DOI: 10.1029/2009JD012346 (cit. on pp. 69, 70).

Dewitte, S., L. Gonzalez, N. Clerbaux, et al. (2008). "The Geostationary Earth Radiation Budget Edition 1 data processing algorithms". In: *Advances in Space Research* 41.11, pp. 1906 –1913. DOI: https://doi.org/10.1016/j.asr.2007.07.042 (cit. on pp. 23, 47).

Diner, D. J., J. C. Beckert, T. H. Reilly, et al. (1998). "Multi-angle Imaging SpectroRadiometer (MISR) instrument description and experiment overview". In: *IEEE Transactions on Geoscience and Remote Sensing* 36.4, pp. 1072–1087. DOI: 10.1109/36.700992 (cit. on p. 65).

Doelling, D. R., N. G. Loeb, D. F. Keyes, et al. (2013). "Geostationary Enhanced Temporal Interpolation for CERES Flux Products". In: *Journal of Atmospheric and Oceanic Technology* 30.6, pp. 1072–1090. DOI: 10.1175/JTECH-D-12-00136.1 (cit. on p. 61).

Domenech, C. and T. Wehr (2011). "Use of Artificial Neural Networks to Retrieve TOA SW Radiative Fluxes for the EarthCARE Mission". In: *IEEE Transactions on Geoscience and Remote Sensing* 49.6, pp. 1839–1849. DOI: 10.1109/TGRS.2010.2102768 (cit. on pp. 30, 71).

Doppler, L., R. Preusker, R. Bennartz, and J. Fischer (2014). "k-bin and k-IR: k-distribution methods without correlation approximation for non-fixed instrument response function and extension to the thermal infrared—Applications to satellite remote sensing". In: *Journal of Quantitative Spectroscopy and Radiative Transfer* 133, pp. 382 –395. DOI: https://doi.org/10.1016/j.jqsrt.2013.09.001 (cit. on p. 49).

ESA (2001). *The Five Candidate Earth Explorer Missions: EarthCARE - Earth Clouds, Aerosols and Radiation Explorer*. Prepared by J.P.V. Poiares Baptista. ESA SP-1257(1): ESA Publ. Division, ESTEC (cit. on pp. 7, 19, 69).

– (2006). *EarthCARE Mission Requirements Document*. Prepared by Mission Advisory Group. EOP-SM/1567/TW (cit. on pp. 7, 19).

Hollstein, A. and J. Fischer (2012). "Radiative transfer solutions for coupled atmosphere ocean systems using the ma trix operator technique". In: *Journal of Quantitative Spectroscopy and Radiative Transfer* 113.7, pp. 536 –548. DOI: https://doi.org/10.1016/j.jqsrt.2012.01.010 (cit. on pp. 3, 49).

IGBP (1992). *Improved global data for land applications*. Tech. rep. 20. International Geosphere–Biosphere Programme, Stockholm, Sweden (cit. on p. 30).

Illingworth, A. J., H. W. Barker, A. Beljaars, et al. (2015). "The EarthCARE Satellite: the next step forward in global measurements of clouds, aerosols, precipitation and radiation". In: *Bull. Am. Meteorol. Soc* 96, pp. 1311–1332. DOI: 10.1175/BAMS-D-12-00227.1 (cit. on pp. 2, 7, 9, 23, 65, 70, 93).

Jacobowitz, H., W. L. Smith, H. B. Howell, F. W. Nagle, and J. R. Hickey (1979). "The First 18 Months of Planetary Radiation Budget Measurements from the Nimbus 6 ERB Experiment". In: *Journal of the Atmospheric Sciences* 36.3, pp. 501–507. DOI: 10.1175/1520-0469(1979)036<0501:TFMOPR>2.0.CO;2 (cit. on p. 2).

Jacobowitz, H., H. V. Soule, H. L. Kyle, and F. B. House (1984). "The Earth Radiation Budget (ERB) Experiment: An overview". In: *Journal of Geophysical Research: Atmospheres* 89.D4, pp. 5021–5038. DOI: 10.1029/JD089iD04p05021 (cit. on p. 2).

Kandel, R., M. Viollier, P. Raberanto, et al. (1998). "The ScaRaB Earth Radiation Budget Dataset". In: *Bulletin of the American Meteorological Society* 79.5, pp. 765–784. DOI: 10.1175/1520-0477(1998)079<0765:TSERBD>2.0.CO;2 (cit. on p. 2).

Kato, S., F. G. Rose, and T. P. Charlock (2005). "Computation of Domain-Averaged Irradiance Using Satellite-Derived Cloud Properties". In: *Journal of Atmospheric and Oceanic Technology* 22.2, pp. 146–164. DOI: 10.1175/JTECH-1694.1 (cit. on pp. 1, 49).

Kato, S., S. Sun-Mack, W. F. Miller, et al. (2010). "Relationship among Cloud Occurence Frequency, Overlap, and Effective Thickness derived from CALIPSO and CloudSat merged Cloud Vertical Profiles". In: *Journal of Geophysical Research* 115.D00H28. DOI: 10.1029/2009JD012277 (cit. on p. 81).

Kato, S., F. G. Rose, S. Sun-Mack, et al. (2011). "Improvements of top-of-atmosphere and surface irradiance computations with CALIPSO-, CloudSat-, and MODIS-derived cloud and aerosol properties". In: *Journal of Geophysical Research: Atmospheres* 116.D19. DOI: 10.1029/2011JD016050 (cit. on p. 2).

Kiehl, J. T. and K. E. Trenberth (1997). "Earth's Annual Global Mean Energy Budget". In: *Bulletin of the American Meteorological Society* 78.2, pp. 197–208. DOI: 10.1175/1520-0477(1997)078<0197:EAGMEB>2.0.CO;2 (cit. on p. 2).

Kinne, S., D. O'Donnel, P. Stier, et al. (2013). "MACv1: A new global aerosol climatology for climate studies". In: *Journal of Advances in Modeling Earth Systems* 5.4, pp. 704–740. DOI: 10.1002/jame.20035 (cit. on pp. 25, 26).

Kohonen, T., T. S. Huang, and M. R. Schroeder (2001). *Self-Organizing Maps*. 3rd. Springer-Verlag New York, Inc. Secaucus, NJ, USA (cit. on p. 77).

Kyle, H. L., J. R. Hickey, P. E. Ardanuy, et al. (1993). "The Nimbus Earth Radiation Budget (ERB) Experiment: 1975 to 1992". In: *Bulletin of the American Meteorological Society* 74.5, pp. 815–830. DOI: 10.1175/1520-0477(1993)074<0815:TNERBE>2.0.CO;2 (cit. on p. 2).

Li, J. and H. W. Barker (2005). "A Radiation Algorithm with Correlated-k Distribution. Part I: Local Thermal Equilibrium". In: *J. Atmospheric Sciences* 62.2, pp. 286–309. DOI: 10.1175/JAS-3396.1 (cit. on p. 82).

Loeb, N. G., S. Kato, and B. A. Wielicki (2002). "Defining Top-of-the-Atmosphere Flux Reference Level for Earth Radiation Budget Studies". In: *J. Climate* 15.22, pp. 3301–3309 (cit. on p. 73).

Loukachine, K. and N. G. Loeb (2004). "Top-of-atmosphere flux retrievals from CERES using artificial neural networks". In: *Remote Sensing of Environment* 93.3, pp. 381 –390. DOI: https://doi.org/10.1016/j.rse.2004.08.005 (cit. on p. 30).

Lucht, W., C. B. Schaaf, and A. H. Strahler (2000). "An algorithm for the retrieval of albedo from space using semiempirical BRDF models". In: *IEEE Transactions on Geoscience and Remote Sensing* 38.2, pp. 977–998. DOI: 10.1109/36.841980 (cit. on p. 25).

Marchuk, G. I., G. A. Mikhailov, M. A. Nazaraliev, et al. (1980). *The Monte Carlo Methods in Atmospheric Optics*. 1st. Springer-Verlag Berlin Heidelberg GmbH (cit. on p. 75).

Mariani, G., M. Kenyon, J. Pearson, and W. Holmes (2016). "Far-infrared room-temperature focal plane modules for radiation budget instrument". In: *2016 41st International Conference on Infrared, Millimeter, and Terahertz waves (IRMMW-THz)*, pp. 1–2. DOI: 10.1109/IRMMW-THz.2016.7758729 (cit. on p. 20).

Mehmood, T., K. Hovde Liland, L. Snipen, and S. Sæbø (2012). "A review of variable selection methods in Partial Least Squares Regression". In: *Chemometrics and Intelligent Laboratory Systems* 118, pp. 62 –69. DOI: https://doi.org/10.1016/j.chemolab.2012.07.010 (cit. on p. 28).

Minnis, P., S. Sun-Mack, D. F. Young, et al. (2011). "CERES Edition-2 Cloud Property Retrievals Using TRMM VIRS and Terra and Aqua MODIS Data x2014;Part I: Algorithms". In: *IEEE Transactions on Geoscience and Remote Sensing* 49.11, pp. 4374–4400. DOI: 10.1109/TGRS.2011.2144601 (cit. on p. 48).

Moody, Eric G., Michael D. King, Crystal B. Schaaf, and Steven Platnick (2008). "MODIS-Derived Spatially Complete Surface Albedo Products: Spatial and Temporal Pixel Distribution and Zonal Averages". In: *Journal of Applied Meteorology and Climatology* 47.11, pp. 2879–2894. DOI: 10.1175/2008JAMC1795.1 (cit. on pp. 25, 26).

Moroney, C., R. Davies, and J.-P. Muller (2002). "Operational Retrieval of Cloud-Top Heights using MISR Data". In: *Geoscience and Remote Sensing* 40.7, pp. 1532–2892. DOI: 10.1109/TGRS.2002.801150 (cit. on p. 73).

Mueller, J., R. Stuhlmann, K. Dammann, et al. (1999). "GERB: An Earth Radiation Budget instrument on second generation meteosat". In: *Advances in Space Research* 24.7. Satellite Applications for Energy Budgets and the Hydrological Cycle, pp. 921 –924. DOI: 10.1016/S0273-1177(99)00356-7 (cit. on p. 2).

Nam, C., S. Bony, J.-L. Dufresne, and H. Chepfer (2012). "The 'too few, too bright' tropical low-cloud problem in CMIP5 models". In: *Geophysical Research Letters* 39.21. DOI: 10.1029/2012GL053421 (cit. on p. 65).

Poli, P., H. Hersbach, D. P. Dee, et al. (2016). "ERA-20C: An Atmospheric Reanalysis of the Twentieth Century". In: *Journal of Climate* 29.11, pp. 4083–4097. DOI: 10.1175/JCLI-D-15-0556.1 (cit. on pp. 25, 26).

Rahman, H., B. Pinty, and M. M. Verstraete (1993). "Coupled surface-atmosphere reflectance (CSAR) model: 2. Semiempirical surface model usable with NOAA advanced very high resolution radiometer data". In: *Journal of Geophysical Research: Atmospheres]* 98.D11, pp. 20791–20801. DOI: 10.1029/93JD02072 (cit. on p. 25).

Ramanathan, V., R. D. Cess, E. F. Harrison, et al. (1989). "Cloud-Radiative Forcing and Climate: Results from the Earth Radiation Budget Experiment". In: *Science* 243.4887, pp. 57–63. DOI: 10.1126/science.243.4887.57 (cit. on pp. 2, 47).

Rossow, W. B. and Y.-C. Zhang (1995). "Calculation of surface and top of atmosphere radiative fluxes from physical quantities based on ISCCP data sets: 2. Validation and first results". In: *Journal of Geophysical Research: Atmospheres* 100.D1, pp. 1167–1197. DOI: 10.1029/94JD02746 (cit. on p. 2).

Rothman, L.S., I.E. Gordon, A. Barbe, et al. (2009). "The HITRAN 2008 molecular spectroscopic database". In: *Journal of Quantitative Spectroscopy and Radiative Transfer* 110.9. HITRAN, pp. 533 –572. DOI: https://doi.org/10.1016/j.jqsrt.2009.02.013 (cit. on p. 49).

Salzen, K. von, J. F. Scinocca, N. A. McFarlane, et al. (2013). "The Canadian Fourth Generation Atmospheric Global Climate Model (CanAM4). Part I: Representation of Physical Processes". In: *Atmosphere-Ocean* 51.1, pp. 104–125. DOI: 10.1080/07055900.2012.755610 (cit. on p. 82).

Scrucca, Luca et al. (2013). “GA: a package for genetic algorithms in R”. In: *Journal of Statistical Software* 53.4, pp. 1–37 (cit. on p. 28).

Smith, G. L. S., B. A. Wielicki, B. R. B. Barkstrom, et al. (2004). “Clouds and Earth Radiant Energy System: An Overview”. In: *Advances in Space Research* 33, pp. 1125–1133. DOI: 10.1016/S0273-1177 (cit. on p. 73).

Stephens, G. L., D. G. Vane, R. J. Boain, et al. (2002). “The CloudSat Mission and the A-Train: A new dimension of space-based observations of clouds and precipitation”. In: *Bulletin of the American Meteorological Society* 83.12, pp. 1771–1790. DOI: 10.1175/BAMS-83-12-1771 (cit. on pp. 2, 69).

Stephens, G. L., J. Li, M. Wild, et al. (2012). “An update on Earth’s energy balance in light of the latest global observations”. en. In: Nature Geoscience 5.10. Received 8 November 2011, Accepted 13 August 2012, Published online 23 September 2012., pp. 691 –696. DOI: 10.1038/ngeo1580 (cit. on p. 2).

Strobl, Carolin and Achim Zeileis (2009). *Party on!–A new, conditional variable importance measure for random forests available in party*. Tech. rep. 50. University of Munich Department of Statistics (cit. on p. 27).

Su, W., J. Corbett, Z. Eitzen, and L. Liang (2015a). “Next-generation angular distribution models for top-of-atmosphere radiative flux calculation from CERES instruments: methodology”. In: *Atmospheric Measurement Techniques* 8.2, pp. 611–632. DOI: 10.5194/amt-8-611-2015 (cit. on pp. 23, 24, 47, 48, 54).

– (2015b). “Next-generation angular distribution models for top-of-atmosphere radiative flux calculation from CERES instruments: validation”. In: *Atmospheric Measurement Techniques* 8.8, pp. 3297–3313. DOI: 10.5194/amt-8-3297-2015 (cit. on p. 43).

Sun-Mack, S., P. Minnis, S. Kato, et al. (2010). “Enhanced Cloud algorithm from collocated CALIPSO, CloudSat and MODIS global boundary layer lapse rate studies”. In: *IEEE Geoscience and Remote Sensing*, pp. 201–204. DOI: 10.1109/IGARSS.2010.5649624 (cit. on p. 81).

Suttles, J. T, R. N. Green, P. Minni, et al. (1988). *Angular radiation models for earth-atmosphere systems. Vol. I. Shortwave radiation*. NASA Rep. RP-1184. NASA, Washington DC (cit. on p. 71).

Theodoridis, S. and K. Koutroumbas (2009). *Pattern recognition. 2009*. 4th ed. Academic Press (cit. on p. 32).

Twomey, S. (1977). “The Influence of Pollution on the Shortwave Albedo of Clouds”. In: *Journal of the Atmospheric Sciences* 34.7, pp. 1149–1152. DOI: 10.1175/1520-0469(1977)034<1149:TIOPOT>2.0.CO;2 (cit. on pp. 1, 47).

Velázquez-Blázquez, A. and N. Clerbaux (2010). *Sensitivity study of the influence of a target spectral signature in the unfiltering process for broadband radiometersc*. Tech. rep. Final Report. ESA/ESTEC (cit. on p. 20).

Velázquez-Blázquez, A., N. Clerbaux, A. Ipe, E. Baudrez, and C. Domenech (2017). *Sensitivity study of the influence of a target spectral signature in the unfiltering process for broadband radiometersc*. Tech. rep. Software Version 3, downloaded through https://earth.esa.int/web/guest/pi-community/apply-for-data/ao-s. ESA/ESTEC (cit. on p. 10).

Viollier, M., C. Standfuss, O. Chomette, and A. Quesney (2009). "Top-of-Atmosphere Radiance-to-Flux Conversion in the SW Domain for the ScaRaB- 3 Instrument on Megha-Tropiques". In: *Journal of Atmospheric and Oceanic Technology* 26.10, pp. 2161–2171. DOI: 10.1175/2009JTECHA1264.1 (cit. on pp. 23, 47).

Wald, L. and J. M. Monget (1983). "Sea surface winds from sun glitter observations". In: *Journal of Geophysical Research: Oceans* 88.C4, pp. 2547–2555. DOI: 10.1029/JC088iC04p02547 (cit. on p. 27).

Wallace, K., N. Wright, D. Spilling, K. Ward, and M. Caldwell (2009). "The broadband radiometer on the EarthCARE spacecraft". In: *Proc.SPIE* 7453, pp. 7453–7453. DOI: 10.1117/12.825837 (cit. on pp. 2, 7, 8, 23).

Webb, M., C. Senior, S. Bony, and J.-J. Morcrette (2001). "Combining ERBE and ISCCP data to assess clouds in the Hadley Centre, ECMWF and LMD atmospheric climate models". In: *Climate Dynamics* 17.12, pp. 905–922. DOI: 10.1007/s003820100157 (cit. on p. 69).

Wielicki, B. A., B. R. Barkstrom, E. F. Harrison, et al. (1996). "Clouds and the Earth's Radiant Energy System (CERES): An Earth Observing System Experiment". In: *Bulletin of the American Meteorological Society* 77.5, pp. 853–868. DOI: 10.1175/1520-0477(1996)077<0853:CATERE>2.0.CO;2 (cit. on pp. 2, 20, 25, 48, 49, 69).

Winker, D. M., M. A. Vaughan, A. Omar, et al. (2009). "Overview of the CALIPSO Mission and CALIOP Data Processing Algorithms". In: *Journal of Atmospheric and Oceanic Technology* 26.11, pp. 2310–2323. DOI: 10.1175/2009JTECHA1281.1 (cit. on pp. 2, 69).

Wiscombe, W. J. (1980). "Improved Mie scattering algorithms". In: *Applied Optics* 19.9, pp. 1505–1509. DOI: 10.1364/AO.19.001505 (cit. on p. 82).

Wood, R. (2012). "Stratocumulus Clouds". In: *Monthly Weather Review* 140.8, pp. 2373–2423. DOI: 10.1175/MWR-D-11-00121.1 (cit. on p. 47).

Wylie, D. P., D. Santek, and D. O. C. Starr (1998). "Cloud-Top Heights from GOES-8 and GOES-9 Stereoscopic Imagery". In: *J. Appl. Meteor.* 37.4, pp. 405–413 (cit. on p. 72).

Yang, P., L. Bi, B. A. Baum, et al. (2013). "Spectrally consistent scattering, absorption, and polarization properties of atmospheric ice crystals at wavelengths from 0.2 to 100 μm". In: *J. Atmos. Sci* 70.1, pp. 330–347. DOI: 10.1175/JAS-D-12-039.1 (cit. on p. 82).

Zhang, M. H., W. Y. Lin, S. A. Klein, et al. (2005). "Comparing clouds and their seasonal variations in 10 atmospheric general circulation models with satellite measurements". In: *Journal of Geophysical Research: Atmospheres* 110.D15S02. DOI: 10.1029/2004JD005021 (cit. on p. 69).

Zhao, M., J.-C. Golaz, I. M. Held, et al. (2018). "The GFDL Global Atmosphere and Land Model AM4.0/LM4.0: 1. Simulation Characteristics With Prescribed SSTs". In: *Journal of Advances in Modeling Earth Systems* 10.3, pp. 691–734. DOI: 10.1002/2017MS001208 (cit. on p. 65).

Zong, J., R. Davies, J.-P. Muller, and D. J. Diner (2002). "Photogrammetric retrieval of cloud advection and top height from the Multi-angle Imaging SpectroRadiometer". In: *Photogrammetric Engineering and Rem. Sens.* 68, pp. 821–829 (cit. on p. 72).

List of Figures

List of Tables

Acknowledgements

First off, I would like to thank Prof. Jürgen Fischer for his support and encouragement and for trusting me to work on this interesting project that made this dissertation possible. I'm proud to count myself among the space scientists in his working group. I would also like to thank Ralf Bennartz for being the second reviewer of this work. I would like to acknowledge my former and current colleagues at the institute for fruitful discussions as well as companionship and sportsmanship during coffee breaks, in particular Nicole, Sören, Lena, and especially Cintia and Bennet who also provided valuable feedback on this work. I would like to express gratitude to my coauthors for their patience and indispensable contributions to publications, in particular Howard W. Barker, Carlos Domenech, Nicolas Clerbaux, and Rene Preusker. Also thanks to all my other colleagues from the ESA Project "CLARA," including Tobias Wehr, for enlightening meetings and good times at conferences. Last but not least, I would like to thank my family and friends for their love and support, especially my parents, Uwe and Cornelia Tornow, and my wife and favourite copyeditor, Lauren.

Curriculum Vitae

For reasons of data protection, the curriculum vitae is not included in the online version.